SHAPE EVOLUTION OF 3D PERIODIC STRUCTURE FABRICATED BY DIRECT-WRITE ASSEMBLY OF CONCENTRATED COLLOIDAL GELS

By

CHENG ZHU

Master of Science

East China University of Science and Technology

Shanghai, China

2006

Submitted to the Faculty of the
Graduate College of the
Oklahoma State University
in partial fulfillment of
the requirements for
the Degree of
DOCTOR OF PHILOSOPHY
December, 2010

SHAPE EVOLUTION OF 3D PERIODIC STRUCTURE FABRICATED BY DIRECT-WRITE ASSEMBLY OF CONCENTRATED COLLOIDAL GELS

Dissertation Approved:

Dr. James E. Smay

Dissertation Adviser

Dr. Martin S. High

Dr. AJ Johannes

Dr. Warren T. Ford

Dr. A. Gordon Emslie

Dean of the Graduate College

ACKNOWLEDGMENTS

This dissertation is dedicated to my dear parents, Mr. Keang Zhu and Mrs. Shuangfeng Chen. I owe a great debt of gratitude to them for their selfish love and support over years. Without their faith, I would never be able to pursue my dreams and aspirations to abroad, and complete my Doctoral work. I would also like to thank my girl friend, Ms. Ya Wang for her accompany during my graduate career. She has sacrificed her own career and spare time to support me. Her enthusiastic personality is a wellspring of encouragement throughout my graduate research.

I would give special thanks to my research advisor, Dr. James Smay for his superb guidance and professional support. Dr. Smay guided me into the scientific research world by showing theoretical knowledge and hands-on experimental skills. His erudite expertise inspires me to do my best and reach further than I would ever have imagined. He tracks the focuses of current research in my area, and motivates me to strive harder and develop skills on multiple fronts. I really enjoy my discussions with him about various technical problems, and look forward to my association with him in the future.

I would also like to thank my committee members; Dr. Martin High, Dr. AJ, and Dr. Warren Ford. I really appreciate that every committee member devoted themselves to answer my questions, solve my problems, and review my progress. I was fortunate to have collaboration with my colleagues, Dr. Sarosh S. Nadkarni and Dr. Jian Xu.

TABLE OF CONTENTS

Chapter Page

1. INTRODUCTION 1

1.1 Motivation and Objectives 1
1.2 Thesis Scope 3
1.3 Thesis Organization 4

2. BACKGROUND 6

2.1 Direct-Write Assembly of Colloidal Inks 6
2.2 Colloidal Processing Mechanisms of Powder Materials 9
2.3 Rheology and Flow Behavior of Colloidal Inks 19

3. VISCOELASTIC PROPERTIES OF COLLOIDAL INKS 25

3.1 Introduction 25
3.2 Experimental Procedure 26
3.2.1 Materials 26
3.2.2 Gels preparation 27
3.2.3 Zeta potential measurement 28
3.2.4 Potentiometric titrations measurement 28
3.2.5 Linear viscoelastic properties measurement 30
3.3 Results and Discussion 30
3.3.1 Zeta potential of Al_2O_3 particles 31
3.3.2 Adsorption of PAA onto Al_2O_3 particles 32
3.3.3 Stress sweep 33
3.3.4 Theoretical modeling of creep and recovery behavior 36
3.3.5 Creep and recovery compliance 38
3.4 Summary 43

4. THIXOTROPIC RHEOLOGY OF COLLOIDAL INKS 44

4.1 Introduction 44
4.2 Experimental Procedure 46
4.2.1 Materials 47

Chapter Page

4.2.2 Rheological measurement 47
4.3 Development of Time Dependent Rheological Model 49
4.3.1 Structural kinetics 50
4.3.2 Constitutive relationship 52
4.3.3 Estimation of parameters 54
4.4 Results and Discussion 55
4.4.1 Steady state rheology 55
4.4.2 Hysteresis loops 58
4.4.3 Breakdown and build-up curves 61
4.4.4 Start-up transient shear flow 63
4.4.5 Structural recovery after cessation of shear flow 66
4.5 Summary 67

5. STRUCTURE AND FLOW DYNAMICS OF COLLOIDAL INKS 68

5.1 Introduction 68
5.2 Mathematical modeling and Numerical Simulation 70
5.2.1 Rheological model 70
5.2.2 Numerical simulation 71
5.3 Experimental Procedure 71
5.3.1 Materials 72
5.3.2 Extrusion pressure measurement 72
5.4 Results and Discussion 74
5.4.1 Bagley end correction 74
5.4.2 Flow dynamics simulation 77
5.4.3 Structure dynamics of colloidal inks 81
5.5 Summary 85

6. SHAPE EVOLUTION OF AS-DEPOSITED SPANNING ELEMENTS 86

6.1 Introduction 86
6.2 Empirical Modeling of Dimensional Analysis 88
6.2.1 Dimensionless groups 88
6.2.2 Relations of dimensionless groups 90
6.2.3 Validation and prediction of empirical model 92
6.3 Mathematical Modeling of Viscoelastic Catenary 93
6.3.1 Bending moment of viscoelastic materials 94
6.3.2 Viscoelastic catenary model development 95
6.3.3 Analytical method for model solution 100
6.3.4 Equilibrium shape profiles of viscoelastic spanning elements 102
6.3.5 Time dependent shape evolution of viscoelastic spanning elements 108
6.4 Summary 113

7. CONCLUSIONS AND FUTURE WORKS 115

Chapter Page

7.1 Conclusions....115
7.2 Recommendations....117

REFERENCES....119

LIST OF TABLES

Table Page

Table 3.1 Fitting parameters of creep and recovery model 41

Table 3.2 Compliance percentage of each model component 42

Table 4.1 Parameters for Al_2O_3 colloidal inks with varying PEI wt% 54

Table 5.1 Dimensions of extrusion system and operation conditions 74

Table 6.1 Empirical constants obtained by least-square regression 92

LIST OF FIGURES

Figure Page

Figure 2.1 Flow diagram of direct-write process.....7

Figure 2.2 Schematic illustrations of Robocasting apparatus (a) x-y-z gantry robot, (b) multi-nozzle array ink delivery system, (c) mixing nozzle ink delivery system.....8

Figure 2.3 Schematic illustration of colloidal inks preparation procedures 11

Figure 2.4 Schematic illustrations of van der Waals potential energy V_{vdw} between two particles as a function of surface distance h 13

Figure 2.5 Schematic illustrations of double layer near a positive charged particle surface and electrostatic potential energy V_{el} as a function of surface distance h 14

Figure 2.6 Net interaction potential between particles based on DLVO theory.....15

Figure 2.7 Schematic illustrations of steric interaction and steric potential energy V_{steric} as a function of surface distance h 17

Figure 2.8 Schematic illustrations of two positive charged particles covered by the polyelectrolytes based on electrosteric stabilization mechanism 18

Figure 2.9 Schematic illustrations of adsorbed anionic polyelectrolyte species on an ideal particle surface as a function of pH and ionic strength 18

Figure 2.10 Schematic cross section of ink flow in a capillary tube with assumed core-shell architecture. A slip layer (δ) of particle depleted solvent is shown between at the tube wall.....21

Figure 2.11 (a) Schematic top view of V-shaped test structure highlighting the inner and outer support structures and spanning elements (marker layer is not shown). (b) Illustration of select spans demonstrating the reference height of 2 mm and the variation of span length (L) between the inner supports as a function of x position.....24

Figure Page

Figure 3.1 The structure of PAA and PEI 27

Figure 3.2 Typical titration curves for PAA and its corresponding first derivative curve; the inset shows the linear calibration curve between the PAA concentration and the mole equivalent of titrant 29

Figure 3.3 Zeta potential of Al_2O_3 with and without PAA adsorption 31

Figure 3.4 The adsorption curve of PAA onto Al_2O_3 particles.....32

Figure 3.5 Linear viscoelastic regions of Al_2O_3 colloidal inks as a function of PEI wt% and solid volume fraction ϕ_{solids} 33

Figure 3.6 Variation of equilibrium elastic shear modulus G'_{eq} with solid volume fraction for Al_2O_3 inks with varying PEI wt% 35

Figure 3.7 Variation of critical stress τ_c with solid volume fraction for Al_2O_3 inks with varying PEI wt% 35

Figure 3.8 Schematic illustrations of mechanical models. (a) Maxwell model; (b) Kelvin-Voigt model; (c) four-element Burgers model; (d) modified Burgers model 36

Figure 3.9 Compliance of Al_2O_3 inks plotted for creep and recovery experiments as a function of PEI wt% and solid volume fraction ϕ_{solids} 39

Figure 4.1 Schematic illustrations of (a) hysteresis loop and (b) shear-stress changes with time in shear-rate changes for a thixotropic material 48

Figure 4.2 Schematic microstructure evolutions of colloidal gels with shear rate change. The larger circles indicate flocs in the gel consisted of gelled particles. The small dark circles indicate single particles 49

Figure 4.3 The variation of (a) overall breakdown constant K_b and (b) overall agglomeration constant K_a as a function of the shear rate $\dot{\gamma}$.....56

Figure 4.4 The steady state flow curves: (a) steady stress-shear rate curves, (b) steady apparent viscosity-shear rate curves.....57

Figure 4.5 The hysteresis loops of experimental results comparing with model prediction: (a) varying PEI wt% at sweep time of 10s, (b) at varying sweep times 60

Figure Page

Figure 4.6 The shear rate step change of experimental results comparing with model prediction. (a) shear rate step-up measurements, (b) shear rate step-down measurements 62

Figure 4.7 Start-up shear flow of Al_2O_3 inks of ϕ_{solids} = 0.49 and PEI wt% = 0.018 for $\dot{\gamma}$ = (a) 0.01, (b) 0.1, and (c) $1s^{-1}$ 63

Figure 4.8 Structural parameter evolution of Al_2O_3 inks with ϕ_{solids} = 0.49 and PEI wt% = 0.018 after cessation of shear flow from varying initial state.....66

Figure 5.1 Schematic illustration of extrusion pressure drop measurement setup ...73

Figure 5.2 Bagley plots for Al_2O_3 gels of ϕ_{solids} = 0.49 with varying PEI wt% = (a) 0.010, (b) 0.014, (c) 0.018 74

Figure 5.3 Computed wall stress τ_w as a function of apparent shear rate $\dot{\gamma}_a$ for nozzle length of L_n = 12.7mm 76

Figure 5.4 Dimensionless velocity profiles under various apparent shear rate compared with no-slip boundary condition CFD simulation results for three gels with varying PEI wt% = (a) 0.010, (b) 0.014, (c) 0.018 extrusion flow in nozzles of L_n = 12.7mm 78

Figure 5.5 Core fraction as a function of apparent shear rate $\dot{\gamma}_a$ for Al_2O_3 gels of ϕ_{solids} = 0.49 with varying PEI wt% in nozzle of L_n = 12.7mm.....79

Figure 5.6 Computed wall slip velocity V_s as a function of apparent shear rate $\dot{\gamma}_a$ for nozzle length of L_n = 12.7mm 80

Figure 5.7 Structural parameter change profile under different apparent shear rate for Al_2O_3 gels of ϕ_{solids} = 0.49 with varying PEI wt% = (a) 0.010, (b) 0.014, (c) 0.018.....81

Figure 5.8 Structure profiles recovery after deposition as a function of time for Al_2O_3 gels of ϕ_{solids} = 0.49 with varying PEI wt% = (a) 0.010, (b) 0.014, (c) 0.018.....83

Figure 6.1 Schematic illusions of 3D periodic structures: (a) space filling layers, (b) high aspect ratio walls, and (c) spanning elements 86

Figure Page

Figure 6.2 Relations between dimensionless groups (a) $\delta z_{mid}/D$ as a function of L/D by keeping $\rho_{gel}\bar{V}^2/G'_{eq}$ constant; (b) $\delta z_{mid}/D$ as a function of $\rho_{gel}\bar{V}^2/G'_{eq}$ by keeping L/D constant.....91

Figure 6.3 Comparison of model predictions with experimental data.....93

Figure 6.4 Model predictions as a function of dimensionless groups and compared with experimental data 93

Figure 6.5 Forces and moments acting on a finite element of the filament.....96

Figure 6.6 Time dependent displacement of an element of the filament.....99

Figure 6.7 Equilibrium deflection profiles of spanning filaments deposited at a speed of $\bar{V}$ = 6 mm/s for PZT colloidal inks at varying pH = (a) 7.60, (b) 6.85, and (c) 6.15.....103

Figure 6.8 Comparison of effective elastic modulus G'_{eff} and equilibrium elastic modulus G'_{eq} of PZT colloidal inks as a function of pH at a deposition speed of $\bar{V}$ = 6mm/s.....105

Figure 6.9 Equilibrium deflection profiles of spanning elements deposited at speeds of $\bar{V}$ = (a) 2mm/s, (b) 8mm/s, for PZT colloidal inks at pH = 6.15 106

Figure 6.10 The effective elastic modulus G'_{eff} of PZT colloidal inks at pH = 6.15 vary with deposition speed $\bar{V}$ 108

Figure 6.11 Mid-span point dynamic deflection of spanning filaments from PZT colloidal inks at pH = 6.15 by assuming $G'_{eff} = 10^5$Pa; and E/ξ = (a) 0.1, (b) 1.0, and (c) 10 109

Figure 6.12 Mid-span point dynamic deflection of spanning filaments from PZT colloidal inks at pH = 6.15 by assuming $G'_{eff} = 10^5$Pa; $E\,\xi/ = 1.0$; $\eta_i = 0.6\eta_o$; and τ_e = (a) 0.1, (b) 1.0, and (c) 10s.....111

NOMENCLATURE

A	area of cross section
D	filament (nozzle) diameter
E	Young's modulus
e	equivalent length of end effects
F_H	horizontal forces balance
F_V	vertical forces balance
G	equilibrium shear modulus
G_0	elastic modulus of free spring
G_i	elastic modulus of spring in the first Kelvin component
G_m	maximum elastic modulus
$G^{'}$	shear modulus
$G^{'}_{eq}$	equilibrium shear modulus
g_0	gravitational constant
h	surface distance between particles
I	area moment of inertia
J	compliance
J_c	creep compliance
J_r	recovery compliance

$J_{component}$	compliance of component
J_{sum}	sum compliance
K	viscosity parameter
K_a	overall agglomeration rate constant
K_b	overall breakdown rate constant
k	system specific prefactor
k_a'	specific agglomeration rate constant
k_a''	specific agglomeration rate constant
k_0	Brownian motion induced agglomeration rate constant
L	span distance
L_n	nozzle length
M	bending moment
m	characteristic material parameter
N	normal shear force
n	characteristic material parameters
n_0	shear thinning exponent
P_y	compressive yield stress
Q	volume flow rate
R	the radius of curvature of the filament
r	radial position
s	arc-length coordinate
s'	new arc-length coordinate
T	tangential tension force

t	time
t'	critical time point
t_{sweep}	sweep time
u	horizontal displacement
V_{total}	total interparticle potential energy
V_{vdw}	van der Waals potential energy
V_{el}	electrostatic potential energy
V_{steric}	steric potential energy
$\bar{V}$	deposition speed
v	vertical displacement
V_s	wall slip velocity
v_r	radial velocity profile
w	distributed load
x	position along the filament
x_i	scaling exponent
Y	distance of surface from neutral axis
y_i	elastic properties of the material
y_0	undetermined constant
y_1	undetermined constant
y_2	undetermined constant
y_3	undetermined constant
α	characteristic material parameter
β	characteristic material parameter

δ	slip layer thickness
δl	adsorbed layer thickness
δz	deflection at any position
δz_{mid}	maximum deflection at mid-span point
δx	neighborhood of the lateral attachment boundaries
ΔP	pressure drop
ε	total strain
ε_e	elastic strain
ε_v	viscous strain
ϕ_{gel}	minimum solid volume fraction for gelatin
ϕ_{solids}	solid volume fraction
γ	shear strain
γ_c	critical elastic strain
$\dot{\gamma}$	shear rate
$\dot{\gamma}_a$	apparent shear rate
η	apparent viscosity
η_e	equilibrium viscosity
η_i	initial viscosity
η_{de}	viscosity decrement term
η_m	zero-shear viscosity
η_∞	infinite viscosity
η_0	viscosity of free dash port

η_i	viscosity in Kelvin component
λ	structural parameter
λ_i	initial structural parameter
λ_e	equilibrium structural parameter
ν	Poisson's ratio
π_i	dimensionless number
θ	kinetic angle of the tangent to the centerline with the horizontal
ρ	exponential factor
ρ_{gel}	gel density
σ	total stress
σ_e	elastic stress
σ_v	viscous stress
τ	applied shear stress
τ_e	relaxation time
τ_y	yield shear stress
τ_r	radial varying shear stress
τ_c	critical stress
τ_{total}	total shear stress
τ^{el}	elastic shear stress
τ^{vis}	viscous shear stress
τ_w	computed wall stress
ξ	traction coefficient of the dashpot

CHAPTER 1 INTRODUCTION

1.1 Motivation and Objectives

Several 3D periodic structures have been successfully fabricated by extrusion-base direct-write assembly of concentrated colloidal gel-based inks [1-6]. The ink filament is extruded continuously from a capillary nozzle and deposited onto a platform to draw complex patterns in a layer-by-layer scheme. These structures have demonstrated widespread potential applications in areas of sensors [7-9], composites [10-12], microvascular networks [13], photonic band-gap materials [14], and tissue-engineering scaffolds [15, 16]. However, current success in freeform fabrication of 3D structures is still achieved by empirically customizing the ink materials, and process variables to meet the manufacturing demand. The advance of direct-write techniques calls for science-based correlations to related process history and ink properties to workpieces quality and manufacturing process optimization.

Despite excellent self-supporting features, concentrated colloidal inks inevitably will undergo shape deformation more or less after deposition due to rheological response during deposition process as well as wetting, gravity, and drying stress and post processing such as sintering [4, 17]. The highlighted applications and functionality of micro-device largely depend on 3D structures geometric fidelity, and this fidelity has

been closely tied to inks rheological properties and shear history of whole deposition process [18]. An ideal direct-write ink must possess shear thinning behavior to facilitate extrusion flow through fine capillary nozzles, and rapid transition from a flowable fluid to a strong elastic solid upon removal of extrusion pressure to maintain desired structures shape after deposition [4, 18]. In contrast, real direct-write inks generally display reversible viscoelastic properties with a high shear modulus at low shear loading, a high degree of shear thinning, and a limited structure recovery time.

From a microstructure prospective, concentrated colloidal inks consist of closely packed flocs network, whose attrition and rebuilding determine the rheological behavior of inks. Here, various factors need to be specified to show their influence on the shape evolution of 3D structures. First, current inks formulation still follow the method that mimic old inks viscoelastic behavior that work for a similar shape, by trial and error adjustments of inks viscosity, and deposition parameters. In order to better tailor the desired inks, their viscoelastic properties need to be quantified to reveal its relationships with microstructures dynamics at low shear loading. Second, current inks were described as simple viscous fluids (i.e., Herschel-Bulkley fluid) after shear flow started. The time dependent reversible response of inks rheological behavior on the shear process needs to be quantitatively described by accounting for the gel networks evolution. Third, 3D structures shape evolution is also the results of shear history from inks rest in the reservoir to extrusion to rest after deposition. In order to better understand the influence of shear history on workpieces quality and optimize the operation conditions of deposition process, flow dynamics simulation need to be carried out to convey an accurate description of inks structure evolution during deposition and thereafter. The

details of ink dynamics between the quiescent, low shear rate and the yielded, high shear rate need to be characterized in relation to the shear history of deposition process. Besides, the failures of deposition process resulting from operation anomalies such as nozzle clogging, over flow, dynamic instabilities should have much to do with extrusion flow dynamics. Finally, although many attempts [6, 9-11] have been made to optimize some process specific writing inks and deposition parameters, most have not been related to the structures and dynamic properties of inks. The microstructure changes in gels network and the interrelation between dynamic ink properties, deposition variables, and shape evolution are poorly understood.

The objective of this project is to obtain a fundamental understanding of the rheological properties, flow dynamics and shape evolution of the concentrated colloidal inks for direct-write assembly techniques through experimental and modeling methods at a microstructure level. The contributions made by this research will open new pathway to serves as a guideline for new inks design, deposition process optimization and 3D structures shape evolution control.

1.2 Thesis Scope

The aims of this project are three-fold: (1) to determine the viscoelastic properties of concentrated colloidal inks and establish the relationship between rheological parameters and static microstructure of gel networks, (2) to investigate the flow dynamics of concentrated colloidal inks during deposition process and quantitatively describe microstructure changes, (3) to measure and model the self-supporting shape evolution of spanning elements with different ink properties and deposition conditions. Each above

aspect is important for the ultimate goal of control and optimal shape evolution of deposited structures. Since inks microstructure changes are the most fundamental reasons for their shape evolution, it is the trend to do the research from a microscopic level.

In this work, we present a comprehensive characterization of concentrated colloidal inks shape evolution for direct-write assembly. First of all, the viscoelastic properties of the ink are characterized and used to define a mass-less mechanical model representation. Second, as a part of experimental characterization of 3D structures shape evolution, the rheological properties of the colloidal ink are measured and use a modified time-dependent rheological model to describe its thixotropic behavior. Third, flow dynamics of concentrated colloidal inks during deposition are calculated incorporating slip boundary conditions and compared with simulation results with slip boundary conditions. Finally, the shape evolution of spanning elements is investigated to correlate the ink properties, deposition variables to the shape evolution. The information collected here aims to elucidate the influence factors related to the shape evolution, and quantitatively describe how these variables contribute to the shape evolution degrees.

1.3 Thesis Organization

This thesis is organized into seven chapters. Chapter 1 (this chapter) states the motivation and objectives of this project, and describes thesis scope and organization that are presented in latter chapters. Chapter 2 is a review of literature pertinent to three interdisciplinary fields: direct-write assembly techniques, concentrated colloidal inks properties used in direct-write techniques, and microstructures and properties evolution of concentrated colloidal inks. Chapter 3 covers the formulation and preparation method

of concentrated colloidal inks, viscoelastic properties of inks at low shear loading. Chapter 4 reports the theoretical and experimental investigations of inks thixotropic rheology during shear flow. A single-phase time-dependent constitutive model is proposed and validated by actual experimental data, where the ink is treated as a homogeneous material with thixotropic properties and microstructure is characterized by a scalar structural parameter. Chapter 5 presents the flow dynamics simulation of concentrated colloidal inks during deposition process with wall slip boundary conditions based on previous rheology results. Chapter 6 describes the shape evolution of spanning elements structures of concentrated colloidal inks. Dimensional analysis was used to reduce relevant parameters, and an empirical model was developed. Besides, a viscoelastic catenary model was raised, and various influence factors are discussed to determine their contributions to the shape evolution. Chapter 7 summarizes the general conclusions drawn from complete work and provides recommendations for future work that could yield better understanding of the shape evolution due to the microstructures evolution of colloidal inks.

CHAPTER 2 BACKGROUND

2.1 Direct-Write Assembly of Colloidal Inks

The concept of "direct-write assembly" [19, 20] is defined as a host of solid freeform fabrication methods, which employ colloidal inks with the desired rheological and consolidation behavior to assemble complex 3D structures through a sequential deposition scheme without the need for traditional part specific tooling, dies or molds. According to the ink flow behavior, direct-write techniques can be categorized into two approaches: (1) droplet-based, and (2) filament-based ink approach [21-23]. In droplet-based writing system, the ink is delivered in the form of discrete droplets to fabricate desired 3D structures. 3D printing [24, 25], direct ink-jet printing [26-28], and related approaches such as hot-melt printing [29-31] are representative droplet-based writing techniques [22, 23]. In contrast, the ink is continuously extruded through a single or multi-nozzle array to create filamentary elements through filament-based writing techniques, such as robocasting [1, 32], fused deposition [33], and micro-pen writing [34]. The filament-based direct-write techniques are especially promising due to their material flexibility, low cost, and capability for self-supporting features [35]. They allow creating advanced composites by multi-material depositions. They have the capabilities to assemble true 3D circuit packages even on curved surface. They also show a route for tissue engineering to fabricate bone scaffolds with integrated cartilage and bone regions.

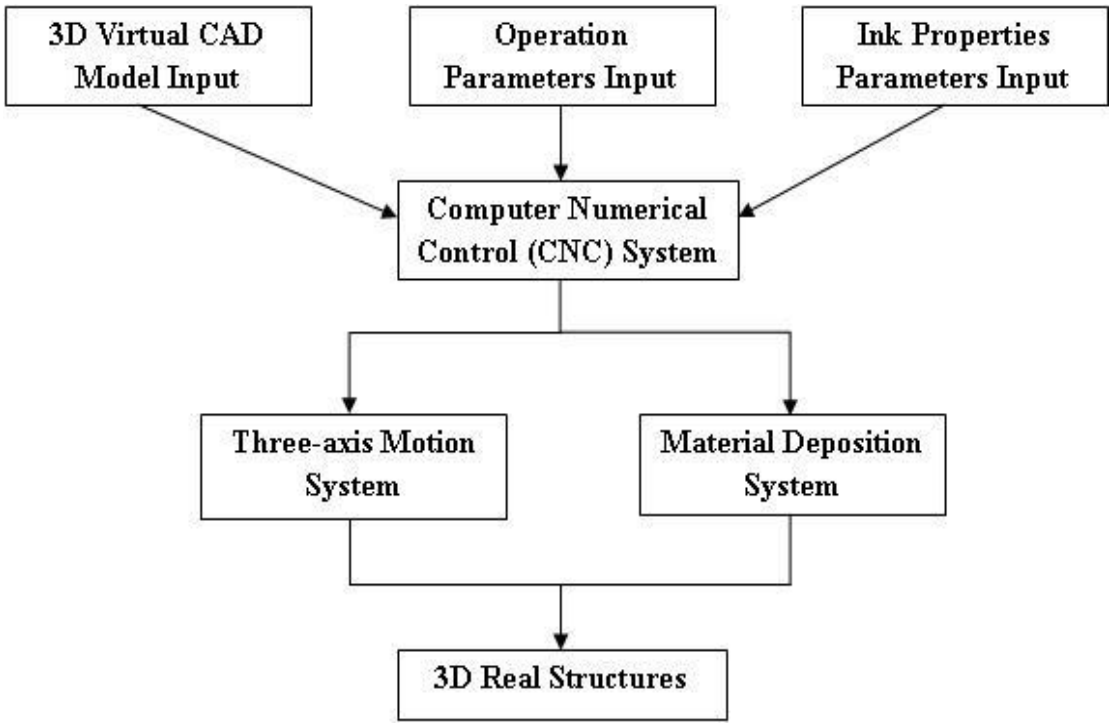

Figure 2.1 Flow diagram of filament-based direct-write process.

The flow diagram of filament-based direct-write procedure for freeform fabrication of 3D structures is presented in Figure 2.1. First, 3D virtual structures are generated through computer aided design (CAD) model tools. Then, the operation parameters, such as deposition speed, applied pressure, nozzle diameter, and spacing height, should be specified. Next, process relevant ink properties, like material types and composition, should be determined. The computer numerical control (CNC) software processes the designed CAD model, operation conditions and ink properties, and conveys them to three-axis motion system and ink delivery system simultaneously. Three-axis motion system controls the accurate tool path for the deposition process. The ink delivery system supplies appropriate volumetric flow rate of inks along the tool-path lines. Based on the cooperation of these two systems, the real 3D structures can be created.

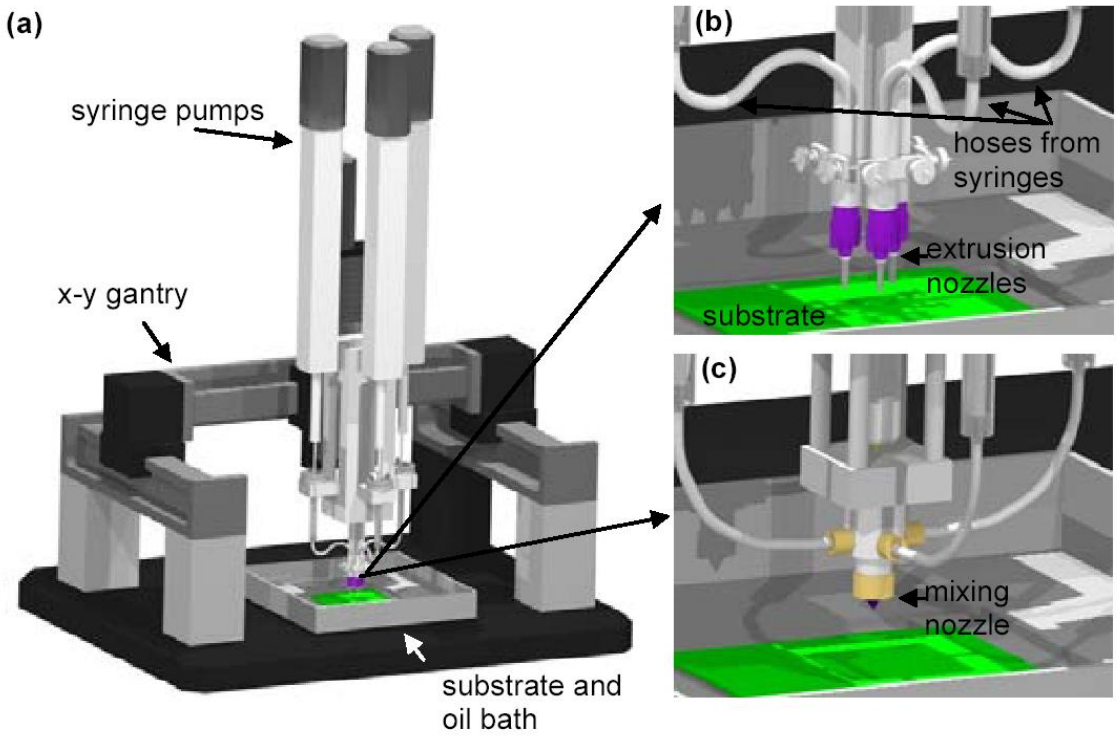

Figure 2.2 Schematic illustrations of Robocasting apparatus (a) x-y-z gantry robot, (b) multi-nozzle array ink delivery system, (c) mixing nozzle ink delivery system [36].

The ink delivery system is the most important component in the whole filament-based direct-write process. It depends on the ink properties, and desired 3D structures and determines the quality of the final products. It commonly consists of three components, propeller, reservoir, and deposition head. The feedstock inks are stored in reservoirs; the displacement part extrudes inks through a deposition head at desired volumetric flow rate. For example, in robocasting, the plunger can be mechanically displaced on the ink reservoir at the constant speed to drive the ink out of the nozzle. Figure 2.2 illustrates the schematics of the robocasting machine and multi-nozzle arrays for parallel printing of discrete ink materials and mixing nozzle system for multi-material mixture printing [16].

Although direct-write techniques have showed huge potential advantages, the challenges are also inevitable. The first challenge lies in the identification of new ink materials and their functions. Further advances require science-based ink design method, instead of empirically formulating new inks by trial and error adjustments of inks composition. The second challenge requires manufacturing high precision, quality parts using these materials. The shape deformation of structures during deposition, drying, and sintering is another direction to advance this technology. The last challenge is how to apply these techniques from prototyping to large-scale production, and to shorten production time and lower cost for these parts.

2.2 Colloidal Processing Mechanisms of Powder Materials

In powder materials processing, it is desirable to produce the uniformly compact green body with fully dense and fine-grain microstructures. Compared to powders consolidation by dry or semidry pressing in a die, colloidal methods are being increasingly used to eliminate any source of heterogeneity in the starting powders and consolidated green bodies, which leads to better control of strength-limiting defects in the final sintered parts.

The term “colloid” is defined as a type of mixture, where particles with feature size of $10^{-9} \sim 10^{-6}$ m are dispersed in a liquid medium. Colloids generally can be divided into two broad classes: lyophilic colloids and lyophobic colloids. Lyophilic (i.e., liquid-loving) colloids show a strong affinity between the dispersed particle and the liquid. The liquid is strongly absorbed onto the particle surfaces, and this system is intrinsically stable due to a reduction in the Gibbs free energy when the particles are dispersed. Polymer solutions

are good examples of lyophilic colloids. Lyophobic (i.e., liquid-hating) colloids are those in which the liquid does not show affinity for the particle. This system is naturally unstable and tends to flocculate due to the Gibbs free energy increase when the particles are distributed in the liquid. Lyophobic colloids can, therefore, only be dispersed when the surface is treated in some way to cause a strong repulsion to exist between the particles. Colloidal inks used in direct-write techniques consisting of insoluble particles in a liquid are well-known examples of lyophobic colloids.

Cesarano et al., [1] pioneered the use of flocculated colloidal gels as inks for direct-write assembly of ceramics. Smay et al., [3, 4] advanced this method to develop aqueous colloidal inks for direct-write techniques. From then on, a broad array of powder materials have been employed to prepare colloidal inks, such as silica [3], lead zirconate titanate [4], barium titanate [37], alumina [38], mullite [5], silicon nitride [39], and hydroxyappatite [15]. Li et al., [37] prepared inks that flowed through 30 μm glass capillary tips using nanoparticle barium titanate. Nadkarni et al., [36, 40] successfully developed multi-material inks by mixing different ceramic particles and ceramic-metal particles. Current success in colloidal ink design is achieved by following this two-step process, illustrated in Figure 2.3. A highly concentrated, stable colloidal suspension is prepared by dispersing the particles in an aqueous medium via electrosteric stabilization [41, 42], by adsorption of polyelectrolytes onto particle surfaces. The well-dispersed colloidal suspension is then gelled by introducing a systematic change mechanism such as pH shift, salt addition [5, 37], or bridging flocculation with a counter polyelectrolyte or other coagulants [38, 40]. This general approach of creating concentrated colloidal inks can be extended to any type of colloidal or nanoparticle materials with alternate surface

chemistry. Therefore, we need to understand the attractive interactions that lead to flocculation and how they can be overcome by repulsive interactions to produce colloids with the desired stability.

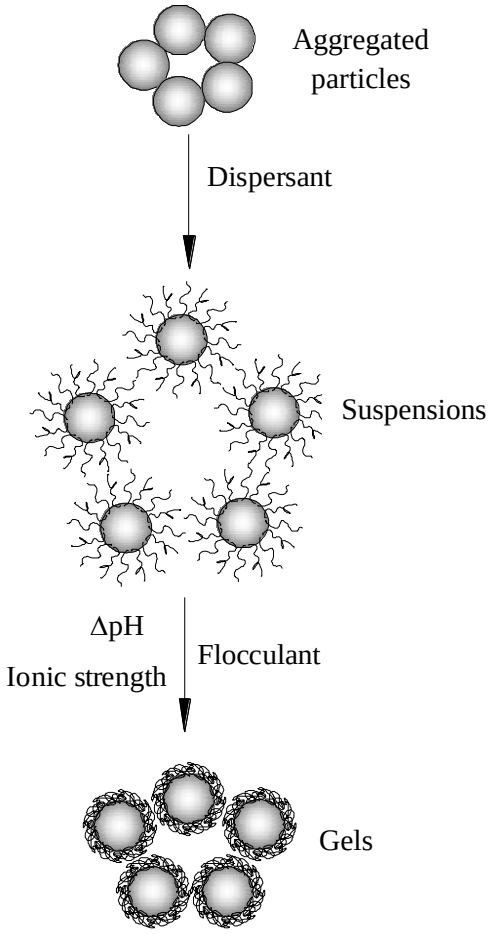

Figure 2.3 Schematic illustration of colloidal inks preparation procedures.

The total interparticle potential V_{total} in a colloidal system is a summation of attractive (e. g. van der Waals) and repulsive (e. g. double layer interactions, steric hindrance) potential energy [43-48]. If V_{total} is positive (net repulsion), the colloidal system is typically fluid and considered stable, whereas a negative (net attractive) potential between colloids includes aggregation and leads to gelation. A distinguishing feature of

the colloidal system is that the contact area between particles and the dispersing medium is large. Particles in a suspension move throughout the liquid due to Brownian motion, gravity and convection currents. Brownian motion ensures the smaller particles, especially in micrometers or less, colliding with each other all the time, whereas the influence of gravity becomes negligible. Long-range forces resulting from van der Waals interactions are ubiquitous and always attractive between particles. The combination of Brownian motion and van der Waals attraction force would result in the formation of agglomeration of the particles to reduce the surface energy if the attractive forces overcome the repulsive forces. The van der Waals force is a weak force and becomes significant only at a very short distance. Van der Waals interaction between two particles is the sum of the molecular interaction for all pair of molecules composed of one molecule in each particle, as well as to all pairs of molecules with one molecule in a particle and one in the surrounding medium such as solvent. The attractive van der Waals interaction potential, V_{vdw}, exhibits a power law distance dependence whose strength depends on the dielectric properties of the interacting colloidal particles and the intervening medium. A schematic representation of V_{vdw} is shown in Figure 2.4. Although the nature of the attraction energy between two particles is the same as that between two molecules, integration of all the interaction between molecules from two particles and from medium results in a totally different dependence of force on distance. The attraction force between two particles decays much slowly and extends over distances of nanometers. As a result, a barrier potential must be developed to prevent agglomeration. Two basic stabilization mechanisms exist to overcome van der Waals attraction between particles: electrostatic stabilization and steric stabilization [20, 49].

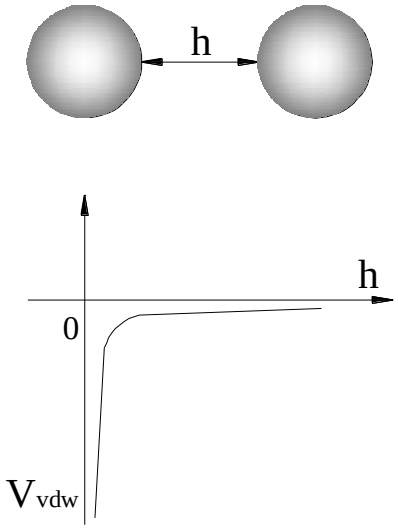

Figure 2.4 Schematic illustrations of van der Waals potential energy V_{vdw} as a function of surface distance h.

Electrostatic stabilization occurs when the repulsion between the particles is generated by a common surface charge on the particles. The repulsion is not a simple case of repulsion between charged particles. An electrical double layer of charge is produced around each particle and the repulsion occurs as a result of the interaction of the double layers. By introducing the analysis of the electrical double layer, we consider how particles acquire an electrostatic charge in an aqueous liquid and the general principle of the double layer. Most substances, such as oxides, acquire a surface electric charge when brought into contact with a polar (e.g. water) medium due to hydrolysis. The charged particles adsorb counter ions from medium, forming electric double layer. The double layer can be regarded as consisting of two regions: the inner region which may include adsorbed ions, and a diffuse region in which ions are distributed according to the influence of electrical forces and random thermal motions. According to Stern Model, the double layer is divided into two parts by a plane (the Stern Plane) which located at about

a hydrated ion radius from the surface. The thickness of the double layer depends on the charge density of the particle surface and the ionic strength of the electrolyte solution. The schematics of electrical double layer and corresponding repulsive electrostatic potential energy between charged particles with exponential distance dependence are shown in Figure 2.5.

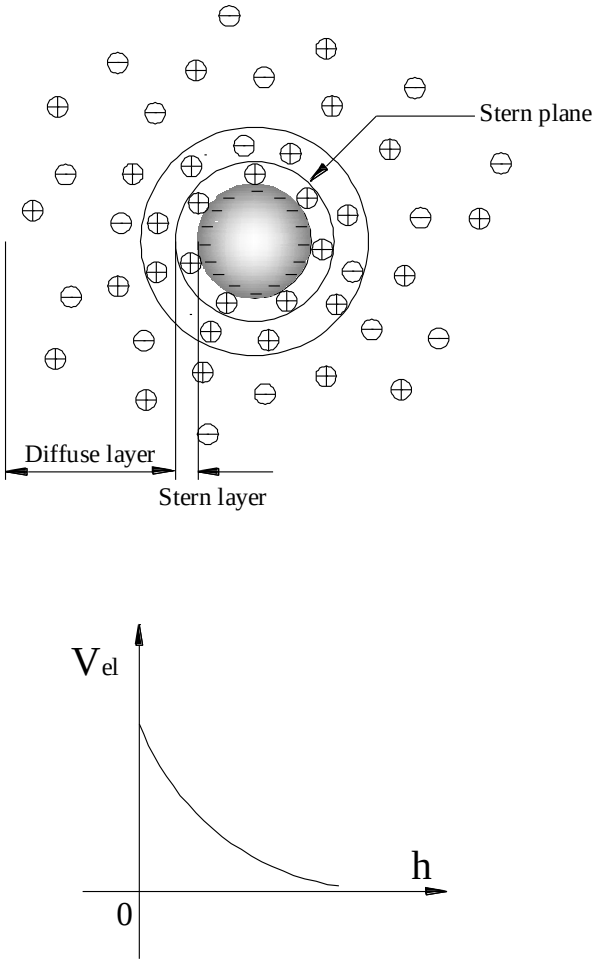

Figure 2.5 Schematic illustrations of the double layer near a positively charged particle surface and electrostatic potential energy V_{el} as a function of surface distance h.

The total interaction between two electrostatic stabilized particles is the combination of the electric double layer and London-van der Waals forces. The electrostatic stabilization of particles in a suspension is successfully described by the DLVO theory,

named after Derjaguin, Landau, Verwey, and Overbeek [50, 51]. This theory predicts the stability of colloidal particles suspended in polar liquids.

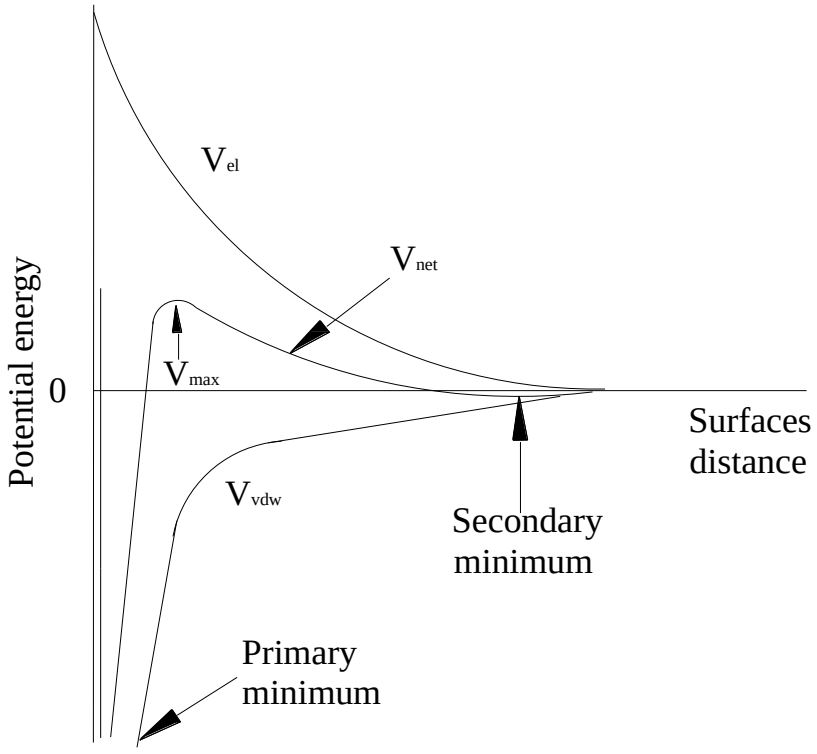

Figure 2.6 Net interaction potential between particles based on DLVO theory.

Figure 2.6 shows the van der Waals attraction potential, electric repulsion potential, and the combination of the two opposite potentials as a function of distance from the surface of a spherical particle. At a distance far from the solid surface, both van der Waals attraction potential and electrostatic repulsion potential reduce to zero. Near the surface is a deep minimum in the potential energy produced by the van der Waals attraction. A maximum, also known as repulsive barrier, is located a little farther away from the surface, as the electric repulsion potential dominates the van der Waals attraction potential. Since the electric potential is dependent on the concentration and valence state of counter-ions and the van der Waals attraction potential is almost

independent of the concentration and valence state of counter-ions, the overall potential is strongly influenced by the concentration and valence state of counter-ions.

Steric stabilization is achieved by adsorption of polymeric additives which serve to form protective colloids. Steric stabilization is the term used to describe the stabilization of colloidal particles which results from the interaction between uncharged polymer chains adsorbed onto the particle surface. The interactions among the polymer chains are fundamentally different from those among the charged ions in electrostatic stabilization is commonly associated with suspensions in organic liquids, but it is also effective for aqueous solvents. There are some requirements for steric stabilization of colloidal suspensions. The adsorbed polymer layer should completely cover the particles and as dense as possible to prevent the particles from close contact. The polymer should be firmly anchored to the surface of the particle. Good solvent condition is required for stabilization. If the solvent condition is poor, interaction between two polymer layers results in attractive, not repulsive, force. The conformation of adsorbed polymer is closely related to its steric stabilization capability, which depends on pH, solvent quality, molecular architecture, chemical nature of the anchoring group, and ionic strength of the medium. When two particles covered with adsorbed polymer layers approach close, the overlap of adsorbed organic layers on neighboring particle surfaces results in a repulsive force, or steric hindrance. Figure 2.7 shows the schematic representation of the stabilization by steric hindrance. Adsorbed polymeric species begin to overlap at $\delta l < h < 2\delta l$, where δl is the adsorbed layer thickness, is on the order of the radius of gyration of a polymer coil. Upon close approach $h < \delta l$, in a good solvent, repulsive interactions arise due to the loss in configurational entropy of the adsorbed chains.

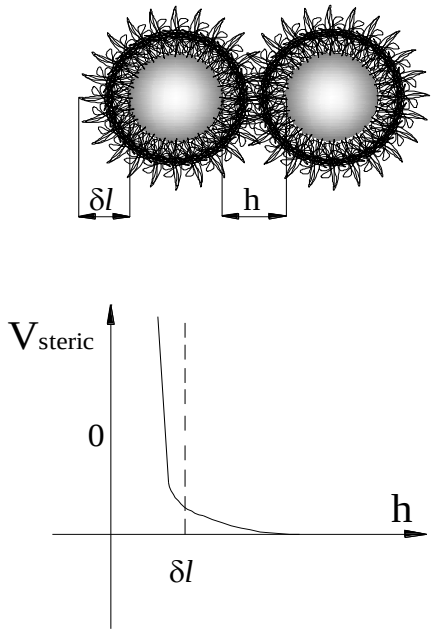

Figure 2.7 Schematic illustrations of steric interaction and corresponding steric potential as a function of surface distance h.

In practice, colloidal inks stabilization is usually achieved by a combination of electrostatic repulsion and steric hindrance, termed as electrosteric stabilization. Electrosteric stabilization requires the presence of adsorbed polymer and significant electrical double-layer repulsion. A common way of achieving electrosteric stabilization in aqueous liquid is through the use of polyelectrolytes that dissociate to produce charged polymers. When polymers attached to a charge particle surface, a polymer layer would develop as discussed above. In addition, an electric potential adjacent to the solid surface would retain. When two particles approach each other, both electrostatic repulsion and steric restriction would prevent agglomeration, as illustrated in Figure 2.8.

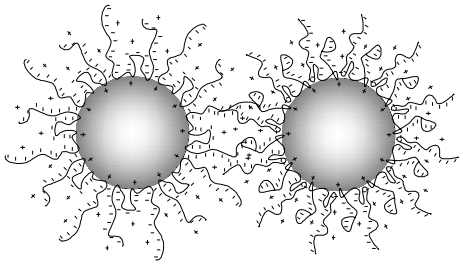

Figure 2.8 Electrosteric interactions schematics of two positive charged particles covered by polyelectrolytes.

The electrostatic component may originate from a net charge on the particle surface and/or charges associated with the polyelectrolyte attached to the surface. Polyelectrolyte adsorption is strongly influenced by the chemical and physical properties of the particle surface and solvent medium. For a given system, the adsorption behavior and conformation can be modified by tailoring solvent conditions. For example, anionic polyelectrolytes are fully ionized and adopt an open coil configuration in solution at high pH due to intersegment repulsion, and adopt a compact coil configuration at high ionic strength and adsorb in a dense layer with low adlayer thickness, as shown in Figure 2.9.

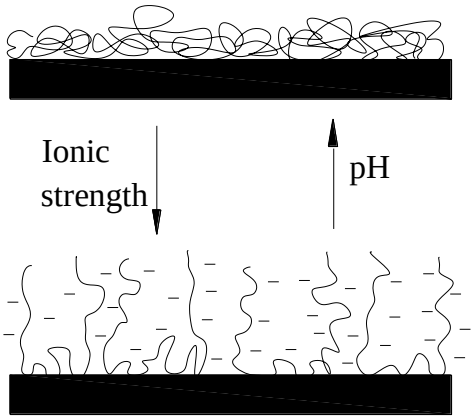

Figure 2.9 Schematic illustrations of absorbed anionic polyelectrolyte species on an ideal ceramic surface as a function of pH and ionic strength.

The stability of colloidal suspensions breaks down when the total energy barrier becomes of the same order of magnitude as the Brownian motion-associated energy of particles. The energy barrier can be affected by surface potential, solution pH, ionic strength, and the particle dimension. As predicted by DLVO theory, dispersions can be rendered unstable by either increasing ionic strength or adjusting pH toward the isoelectric point (IEP) at which the surface potential is minimum. Coagulation can be achieved via addition of a salt to a dispersed suspension. For electrosteric dispersion the electrostatic charges on the polyelectrolyte chains are shielded, allowing them to coil and act as uncharged polymers. Thus, the salt reduces the solvent quality and hence enhances adsorption. Upon suppression of the diffuse double layer, steric forces dictate the stability of the suspension. If the adsorbed layer is relatively thin, attraction may dominate due to van der Waals forces and the suspensions will become more viscous. As predicted by DLVO theory, dispersions can be rendered unstable by either increasing ionic strength or adjusting pH toward the isoelectric point (IEP).

2.3 Rheology and Flow Behavior of Colloidal Inks

Concentrated colloidal inks generally display a finite yield stress and reversible fluid-to-solid transition behavior, which facilitate inks flow during extrusion and hold the desired shape after deposition. This rheological behavior has led to successful printing of several basic shapes and is due to attrition and re-building of colloidal gels structure. The important rheological parameters for a given ink may include its apparent viscosity, yield stress under shear, and viscoelastic properties (i.e., the loss and elastic moduli). Typically, such parameters are tailored for the specific direct-write technique used.

The viscosity of a flocculated suspension depends on the shear rate, the strength and range of the attraction between particles, and the solid volume fraction, ϕ_{solids}. When $\phi_{solids} < \phi_{gel}$ (the minimum solid loading for gelation to occur), the system consists of a clustered fluid, whereas at $\phi_{solids} \geq \phi_{gel}$, it is a colloidal gel. The suspension viscosity typically decreases with increasing shear rate (shear thinning), and increases with the depth of the attractive potential [52]. The relationship between shear stress and shear rate is commonly described by the Herschel Bulkley model: [53]

$$\tau = \tau_y + K\dot{\gamma}^{n_0} \tag{2.1}$$

where τ and τ_y are the applied shear stress and shear yield stress respectively, K is a viscosity parameter, $\dot{\gamma}$ is the shear rate, and n_0 is a shear thinning exponent. As the ink flows through the deposition nozzle under a pressure gradient $\Delta P / L_n$, a radial varying shear stress τ_r develops:

$$\tau_r = \frac{r\Delta P}{2L_n} \tag{2.2}$$

where r is the radial position within the nozzle, ΔP is the pressure drop, and L_n is the length of the nozzle. The extrudate was hypothesized to possess dynamic core-shell architecture as a result of the radially varying shear stress within the extrusion nozzle [4, 45]. Based on the radial varying shear stress and Herschel-Bulkley equation, Smay et al., [54] extended this core-shell model to a three-zone velocity profile with the cylindrical deposition nozzle that consists of an unyielded core moving at constant velocity

surrounded by a yielded shell experiencing laminar flow and a thin slip layer devoid of colloidal particles at the nozzle wall, as illustrated in Figure 2.10 [55].

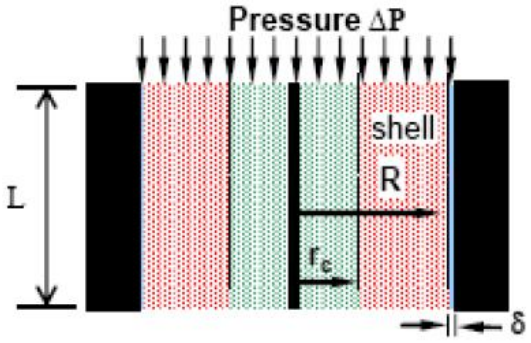

Figure 2.10 Schematic cross section of ink flow in a capillary tube with assumed core-shell architecture. A slip layer (δ) of particle depleted solvent is shown between at the tube wall. [54]

This filamentary architecture arises because the percolating network of attractive particles within the gelled ink is capable of transmitting stress above ϕ_{gel}. When stress beyond its yield point (τ_y), the ink exhibits shear thinning flow behavior due to the attrition of floc-floc bonds within gels network. Detailed characterizations of a variety of colloidal gels [56, 57] of homogeneous, single composition particles have demonstrated a generalized power-law-scaling behavior of their elastic properties described by [45, 58]

$$y_i = k\left(\frac{\phi_{solids}}{\phi_{gel}} - 1\right)^{x_i} \tag{2.3}$$

where k is a system-specific prefactor, x_i is a scaling exponent, and y_i is the property of interest (e.g., shear yield stress (τ_y), shear modulus (G'), or compressive yield stress (P_y). The equilibrium mechanical properties of colloidal gels are governed by two parameters:

ϕ_{solids}, which is proportional to their bond density, and ϕ_{gel}, which scales inversely with bond strength. As the interparticle forces are made more attractive, colloidal gels (constant ϕ_{solids}) experience significant increases in their elastic properties. [46, 48, 56, 58] The density of interparticle bonds increases with ϕ_{solids} and as the particles are made more attractive, ϕ_{gel} decreases (i.e., particles form a gel network even at low concentration), resulting in a more rigid gel. The elastic properties (G', τ_y, and P_y) of colloidal gels exhibit a power-law dependence on ϕ_{solids} similar to colloidal glasses, although the exponent values differ significantly. Reub and Zukoski [56] investigated the behavior of SiO_2 gels and found exponent values of 4 ~ 6 for G', which are much smaller than their glassy counterparts. Channell et al., [58] studied the shear and compressive Rheology of Al_2O_3 gels. They found that P_y and τ_y exhibited a similar scaling exponent, x_i ~ 5. Rao [59] have reported the exponent values for $BaTiO_3$ nanoparticle gels to ~ 4, 4, and 6 for G', τ_y, and P_y, respectively. Similar power law exponent values for colloidal gels have been reported in other studies [60-62].

Smay et al., [4] first related equilibrium shear rheological properties of PZT inks to shape evolution of structures. A simply supported, elastic beam model was used to describe a filamentary rod with circular cross-section that deflects under its own weight, as given by:

$$\delta z = \frac{wx}{24EI}(2Lx^2 - x^3 - L^3) \tag{2.4}$$

where w is the distributed load, x is the position along the rod, E is the Young's modulus of the filament ($E = (1+\nu)2G'$) [63], ν = 0.5 is the Poisson's ratio for the filament [58], and I is area moment of inertia of the circular cross section ($I = \pi D^4 / 64$). The minimum ink elasticity requires assembling a given periodic structure can be estimated by setting a criteria for the maximum acceptable deflection of $\delta z_{mid} < 0.05D$ for y = L / 2, and using the following equation:

$$G' \geq 1.39 \times 10^4 \rho_{gel} g_0 \frac{L^4}{D^3} \tag{2.5}$$

where ρ_{gel} is the gel density, g_0 is the gravitational constant, L is the span length, and D is the diameter of the filament. In this study, mesoscale V-shaped test structures were assembled, consisting of a support base, a spanning layer, and a marker layer, as illustrated in Figure 2.11. Deflection measurement of spanning elements was used to probe the relationship between gel strength, deposition speed, and shear rate profiles in the nozzle. Smay et al., [3] combined optical images and weight loss data of 3D structures to illustrate the ability of silica gels to span unsupported regions.

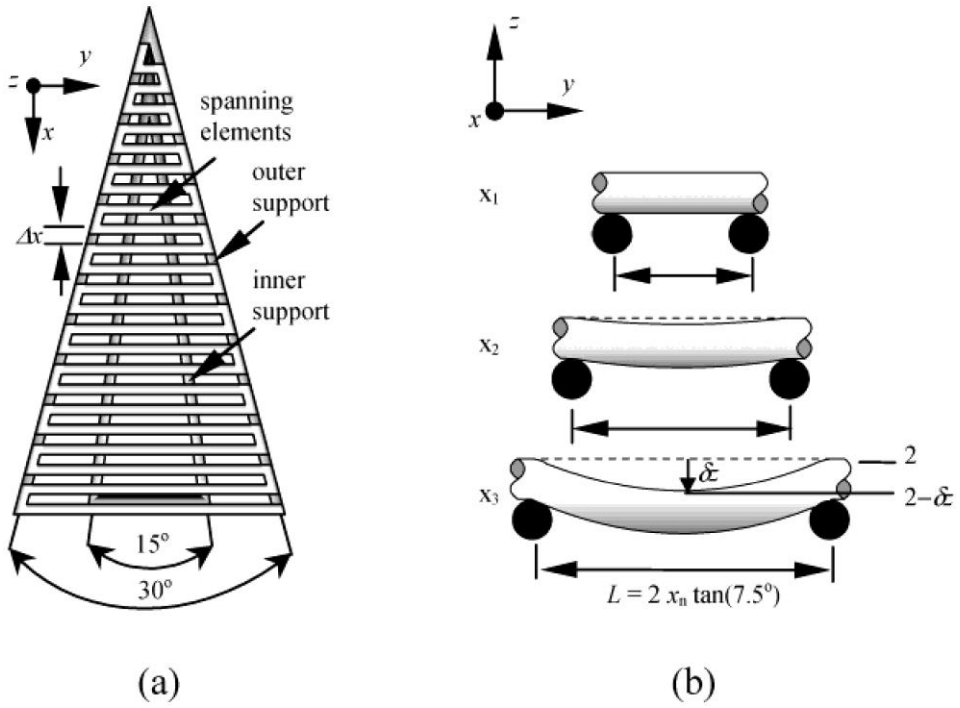

Figure 2.11 (a) Schematic top view of V-shaped test structure highlighting the inner and outer support structures and spanning elements (marker layer is not shown). (b) Illustration of select spans demonstrating the reference height of 2 mm and the variation of span length (L) between the inner supports as a function of x position [4].

CHAPTER 3 VISCOELASTIC PROPERTIES OF COLLOIDAL INKS

3.1 Introduction

The concentrated colloidal ink consists of a percolating network of attractive flocs, whose strength directly determines viscoelastic properties of ink materials. Previous work shows that inks viscoelastic properties are controlled by solid volume fraction ϕ_{solids} and inter-flocs force [9-12]. The solid volume fraction ϕ_{solids} is proportional to flocs bond density, and inter-flocs force determines flocs bond strength. Thus, tailoring the magnitude and range of attractions through solution conditions as well as solid volume fraction allows controlling mechanical properties of colloidal inks. By adjusting the solid volume fraction, pH value, compositions, flocculants concentration, or additional salts, the viscoelastic properties can be tailed over many orders of magnitude to facilitate inks flow through the deposition nozzle and then maintain their filaments shape even as they span gaps in the underlying layers [18, 40].

Here, Al_2O_3 concentrated colloidal gels were used as model ink materials. The Al_2O_3 powders used are high purity, sub micrometer-size, and relatively monodispersed. To disperse Al_2O_3 powders in aqueous suspensions with polyelectrolytes addition, several critical factors such as the pH, the surface chemistry of powders, the degree of polyelectrolytes dissociation, the molecular weight of polyelectrolytes, and the

adsorption of polyelectrolytes must be understood and controlled [41, 42, 64, 65]. After the stabilized suspensions were obtained, the gel-based inks were prepared by adding appropriate amount of flocculants. During the extrusion, the unyielded ink must sustain the creep deformation caused by the extrusion pressure induced shear stress. Viscoelastic properties of Al_2O_3 gels before yielding can be measured by creep and recovery test within linear viscoelastic region. This method has the advantage of avoiding destruction in the sample. This permits the determination of rheological parameters under conditions which approach its conditions at undisturbed state and, as a consequence, allows a relationship between the results obtained and the actual structure of the ink material to be drawn.

In this chapter, the equilibrium shear modulus and creep and recovery behavior of Al_2O_3 colloidal gels were measured as first step of a series shape evolution experiments. Here, shear modulus and creep compliance were used as diagnostic tools to characterize dynamic viscoelastic properties, which are an essential requirement for new ink design and shape evolution improvement. We focused on the relations between gels network structures and their rheological properties as a function of solid fraction ϕ_{solids} and flocculant concentration. A mass-less mechanical model was used to analyze the creep and recovery behavior of Al_2O_3 colloidal inks.

3.2 Experimental Procedure

3.2.1 Materials

Aluminum oxide powders (AKP-30, Sumitomo Chemical Co., Tokyo, Japan, with a mean particle size of 0.32 μm, a specific surface area of 7.1 m^2/g, and a density of 3.97

g/cm^3) served as ceramic phase. A 40% aqueous solution of poly(acrylic acid) (PAA) (Darvan 821A, R.T. Vanderbilt Co., Norwalk, CT) was used as a dispersant. Hydroxypropyl methylcellulose (HPMC) (Methocel F4M, Dow Chemical Co., Midland, MI, with a molecular weight of 3500) was prepared in a 5 wt% stock solution and used as a viscosifier. Nonlinear poly(ethylenimine) (ICN Biomedical, Aurora, OH, with molecular weight of 50,000~100,000) ($PEI_{50\text{-}100k}$) were prepared in aqueous stock solutions with 10% polymer weight, and served as flocculants These polyelectrolyte structures are shown in Figure 3.1. All samples were prepared in de-ionized water having a nominal conductivity of $5\times10^{-4}\,\Omega^{-1}$ cm^{-1}.

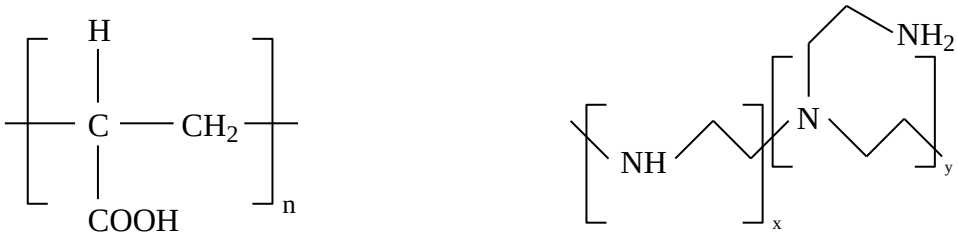

(a) (b)

Figure 3.1 The structure of (a) PAA and (b) PEI.

3.2.2 Gels preparation

Concentrated Al_2O_3 colloidal gels preparation follows a two-step procedure. Firstly, Darvan 821A (0.65 wt%, based on alumina weight), de-ionized water, and alumina powders were added sequentially into a 250 ml sample cup containing about 30 g of 3 mm diameter zirconia milling media. The blend was mixed for 3 min in a non-contact mixer (AR-250, Thinky Co., Laguna Hills, CA) to obtain a high concentrated colloidal suspension. Next, HPMC was added to achieve 7 mg/ml in the liquid phase. After mixed for 1.5 min and kept equilibrium for 1hr, these suspensions were gelled by adding the

flocculant of 10 wt% $PEI_{50\text{-}100k}$ solution, to achieve a desired flocculant concentration. In this study, the Al_2O_3 colloidal inks with solid fraction ϕ_{solids} = 0.45, 0.47, and 0.49 were prepared. For each of these ink, the PEI concentration was selected as PEI wt% = 0.010, 0.014, and 0.018.

3.2.3 Zeta potential measurement

Zeta potentials were measured in dilute Al_2O_3 dispersions using acoustophoretic titration. Suspensions of 4 vol% were prepared by mixing 28 g of Al_2O_3 with 168 ml deionized water. The suspension was then treated with an ultrasonic horn at 30 KW for 10 min. To determine the zeta potential as a function of pH, 1.0 N standard HNO_3 and KOH were used to adjust pH values. To determine zeta potential versus PAA concentration, 2.0 wt% of PAA solution was used to add to the suspension during titration.

3.2.4 Potentiometric titrations measurement

A standard procedure for potentiometric titration has been adopted from the literature [64]. A representative potentiometric titration curve and its first derivative are given in Figure 3.2. Two titration peaks are observed in the first derivative curve. The distance between the two peaks is the amounts of the mole of equivalent (meq) titrant required to titrate PAA. The linear calibration curve in the inset of Figure 3.2 has been obtained for a known PAA concentration, and this calibration curve is used to determine the unknown amount of PAA in the solution.

Aqueous suspensions of 12 vol% Al_2O_3 with different concentrations of PAA were prepared at pH values ranging from 3 to 10. While the Al_2O_3 powder is being added, the

pH is constantly monitored and adjusted so that it is always within 0.2 pH unit of the desired pH values. After mixing, the slurries were deagglomerated by using a high-energy ultrasonic horn for 10 min and the pH is measured and adjusted again if necessary. The samples then are put into a gentle mechanical shaker for approximately 24 h equilibrium and then centrifuged for 20 min at 11000 rpm to obtain the supernatants. The residual PAA concentration in the supernatant was analyzed by using the same previously stated titration procedure and then determined by using the linear calibration curve in Figure 3.2. The total amount of PAA adsorbed on Al_2O_3 was then calculated based on a mass balance for PAA.

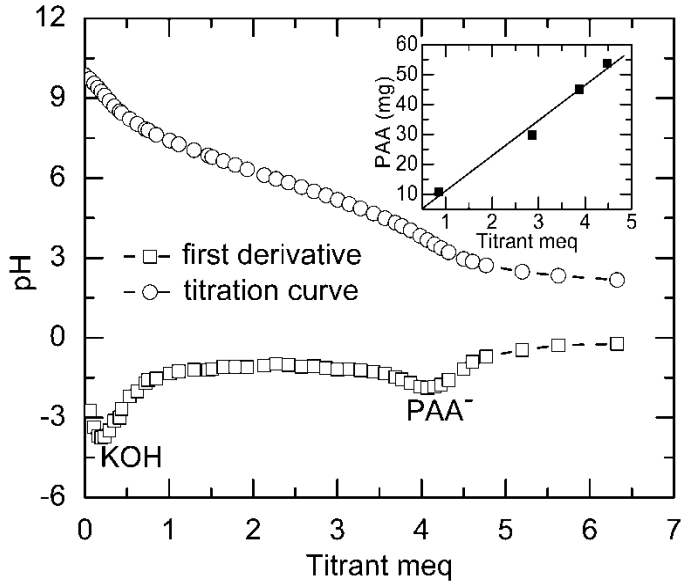

Figure 3.2 Typical titration curves for PAA and its corresponding first derivative curve; the inset shows the linear calibration curve between the PAA concentrations and the mole equivalent (meq) of titrant.

3.2.5 Linear viscoelastic properties measurement

Stress sweep oscillation followed by creep and recovery measurements were carried out using a high-precision stress controlled rheometer (Bohlin C-VOR 200, Malvern Instruments, Westborough, MA) under the isothermal condition at 25 ^{0}C. A cup and bob geometry system (C14, Cup ID = 16 mm and Bob OD = 14 mm) with serrated walls was used to prevent the wall slip. For every measurement, the sample was subjected to a pre-shear rate of $\dot{\gamma} = 0.2\ s^{-1}$ for 1 min and then left at rest for 10 min to provide a consistent shear history. A stress sweep from 10^{-2} to 10^{3} Pa at constant frequency of 0.5 Hz was conducted to record the elastic modulus variations as a function of sweep stress and determine the limits of linear behavior (i.e., where the shear modulus G' is approximately constant). The critical stress (τ_c) is defined as the stress where elastic modulus falls to 90% of the plateau value.

After the stress sweep, the sample was allowed to rest in the cup for 10 min followed by a creep and recovery measurement. The creep compliance, $J_c(t)$ was measured by application of an instantaneous stress at time t = 0 and held constant for 120 s. During this creep interval, the shear strain (γ) was measured as a function of time. At the end of the interval, the stress was reduced to zero and γ was again measured as a function of time for another 120 s as recovery interval to calculate the recovery compliance, $J_r(t)$. The compliance J(t) was calculated based on:

$$J(t) = \frac{\gamma(t)}{\tau} \tag{3.1}$$

3.3 Results and Discussion

3.3.1 Zeta Potential of Al_2O_3 particles

Al_2O_3 has been verified to be an amphoteric oxide that is composed of negative and positive surface sites. And the pure Al_2O_3 powder in the acid solution is positively charged. The negatively charged PAA adsorbed onto the positively charged sites existing on the Al_2O_3 surface. Figure 3.3 illustrated the surface zeta potential of Al_2O_3 powders as a function of pH values. For the bare Al_2O_3 powders, the isoelectric point (IEP) is around at pH = 8.3. When pH is below the IEP, the particle is positively charged. When the pH is above the IEP, the particle is negatively charged. While the Al_2O_3 powders coated with PAA, the surface zeta potential decreased dramatically. The IEP also decreased to about pH = 4.6. We can find that the coated dispersant can significantly change the physic-chemical properties of particles surface.

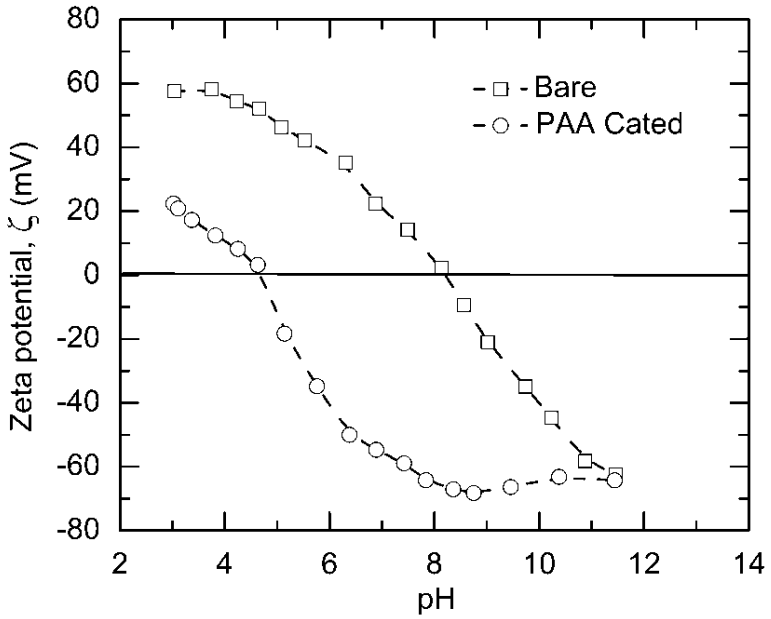

Figure 3.3 Zeta potential of Al_2O_3 particles with and without PAA adsorption.

3.3.2 Adsorption of PAA onto Al_2O_3

Titration analysis results of the PAA adsorption onto Al_2O_3 particles were illustrated in Figure 3.4. The concentration of PAA adsorbed from solution increased with the amount of PAA in solution up to a plateau level of average value 2.4 mg PAA/g Al_2O_3. There are two factors likely explain the observed phenomena. The first has to do with the amphoteric characteristics of the Al_2O_3 surface. Because of the net positive charges on the surface, the positive sites must be attractive to the negative sites of ionic PAA. The H^+ ion from hydrolysis also decreased the pH values of the solution, until IEP was reached.

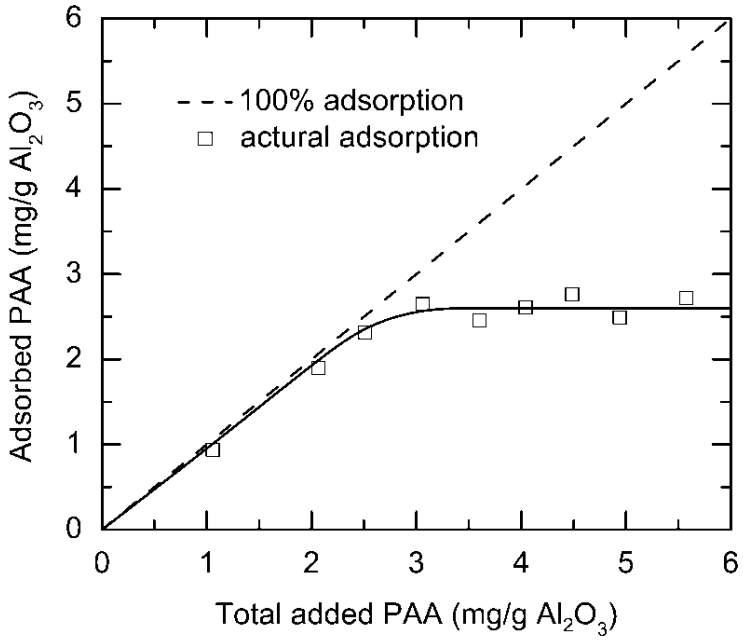

Figure 3.4 The adsorption curves of PAA onto Al_2O_3 particles.

3.3.3 Stress sweep

The stress sweep measurements revealed distinct linear viscoelastic regions for each of the ink studied.

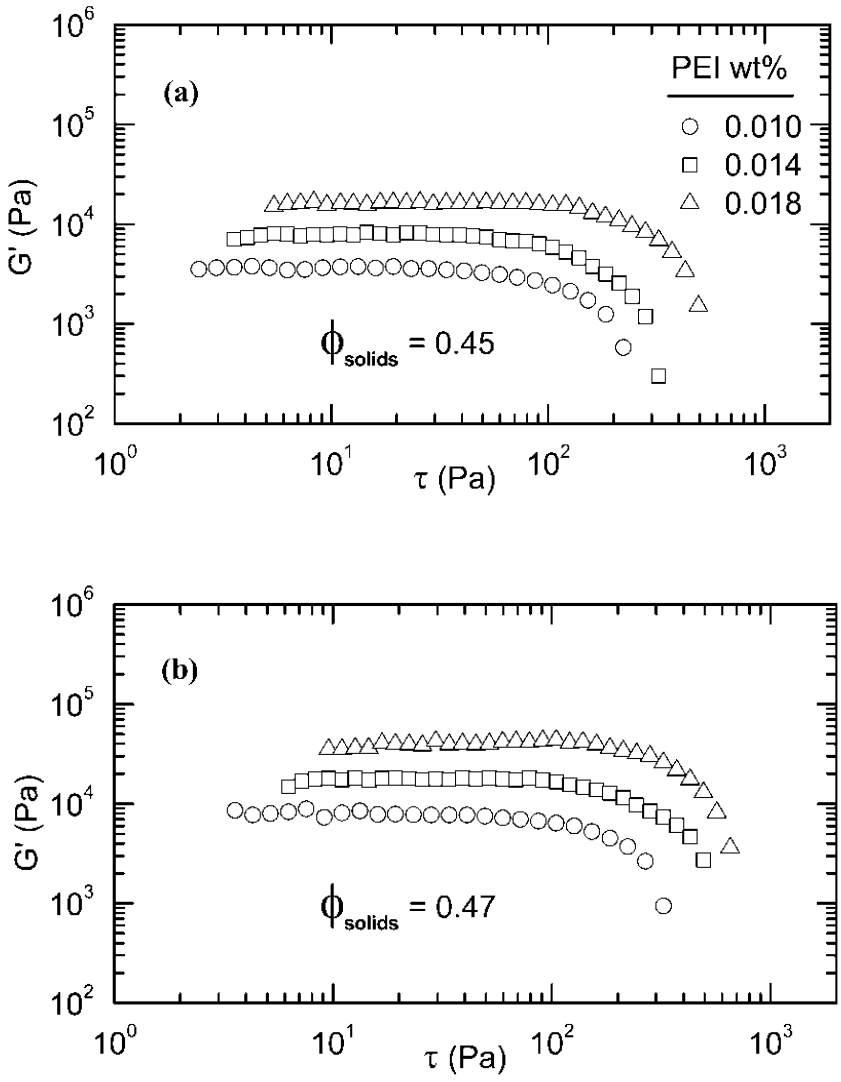

Figure 3.5 Linear viscoelastic regions of Al_2O_3 gels as a function of PEI wt% for ϕ_{solids}= (a) 0.45, (b) 0.47, and (c) 0.49.

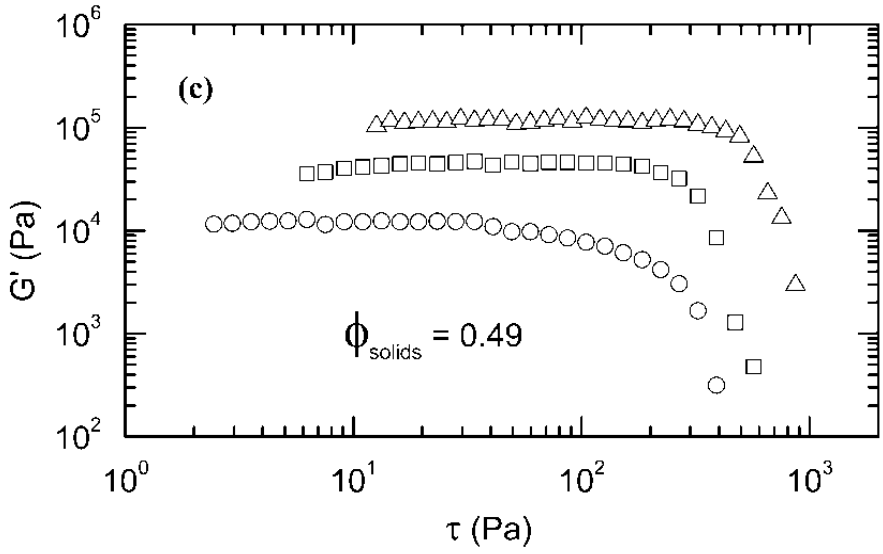

Figure 3.5 Linear viscoelastic regions of Al_2O_3 gels as a function of PEI wt% for ϕ_{solids}= (a) 0.45, (b) 0.47, and (c) 0.49.

As illustrated in Figure 3.5, when the shear stress τ logarithmically increases from low to high value, the elastic modulus G' keeps constant as equilibrium elastic modulus G'_{eq} until critical value τ_c. After that, the elastic modulus G' decreases dramatically. The scaling of equilibrium elastic modulus G'_{eq} and critical stress τ_c with solid fraction ϕ_{solids} for varying PEI wt% are illustrated in Figure 3.6 and 3.7. The trends are as expected: for a fixed value of ϕ_{solids}, the plateau modulus G'_{eq}, and critical stress τ_c increases with increasing PEI wt% (i.e., stronger gels). For a given PEI wt%, the G'_{eq} and τ_c increases with ϕ_{solids}. Furthermore, G'_{eq} of Al_2O_3 inks are more sensitive to PEI wt% than to ϕ_{solids}.

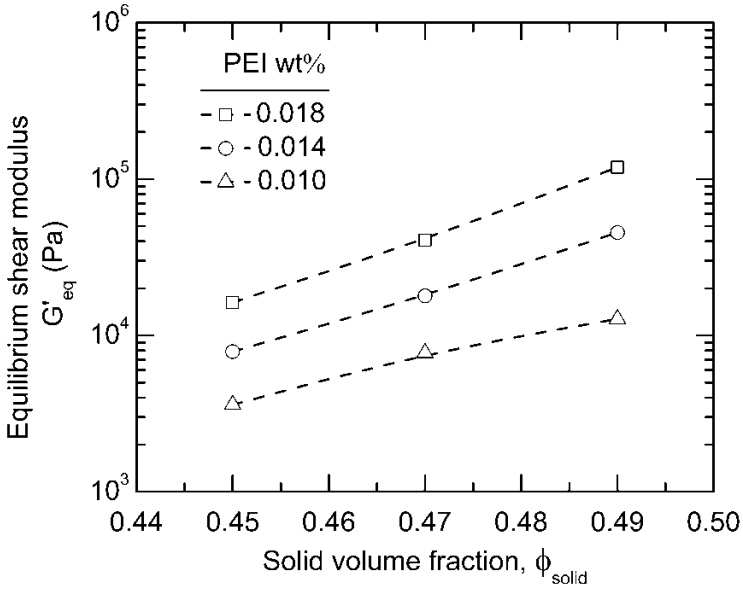

Figure 3.6 Variation of equilibrium elastic shear modulus G'_{eq} with solids fraction ϕ_{solids} for Al_2O_3 inks with varying PEI wt%.

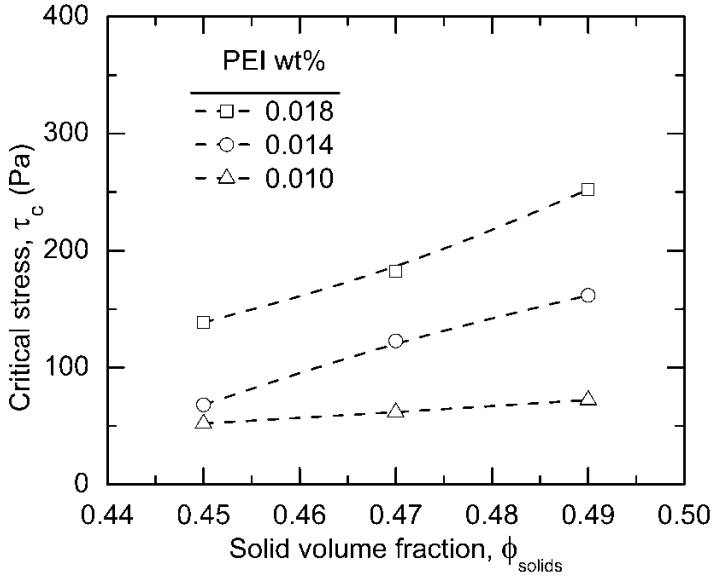

Figure 3.7 Variation of critical stress τ_c with solids fraction ϕ_{solids} for Al_2O_3 gels with varying PEI wt%.

3.3.4 Theoretical modeling of creep and recovery behavior

Creep and recovery test within linear viscoelastic region can keep the microstructure of the sample materials undisturbed and especially help to investigate the dynamic behavior of sample materials existing under the constant stress. Mass-less mechanical models, combining the purely elastic springs and purely viscous dashpots can be used to describe the deformation of a viscoelastic system by fitting the creep and recovery data. The most common mechanical analogs include the Maxwell model, Kelvin-Voigt model and Burgers model as illustrated in Figure 3.8.

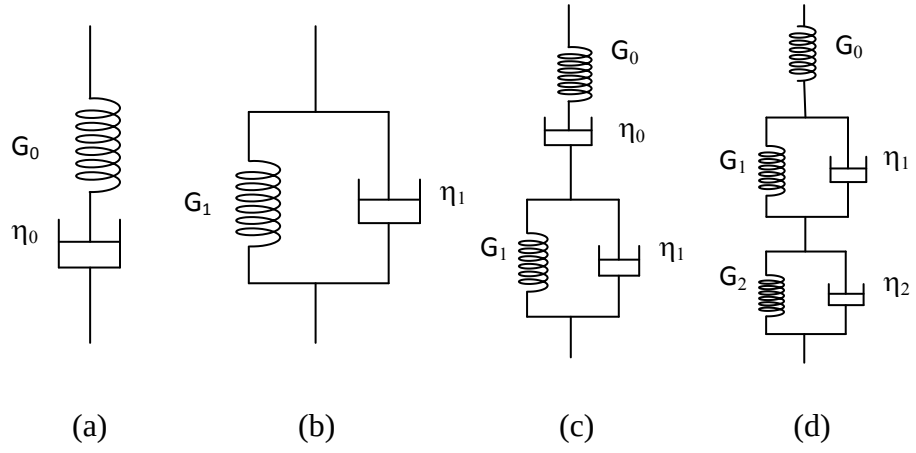

Figure 3.8 Schematic illustrations of mechanical models. (a) Maxwell model; (b) Kelvin-Voigt model; (c) four-element Burgers model; (d) modified Burgers model.

In Maxwell model, the spring and dashpot is associated in series, where G_0 is elastic modulus of free spring, and η_0 is the Newtonian viscosity of free dashpot. [66, 67] The compliance can be expressed as:

$$J(t) = \frac{1}{G_0} + \frac{t}{\eta_0} \tag{3.2}$$

In Kelvin-Voigt model, they are associated in parallel, where G_1 is retarded elastic modulus, and η_1 is internal viscosity. [66, 68] Stress τ, strain $\gamma(t)$ and its rates of change with respect to time t are governed by the equation of the form:

$$\tau = G_1\gamma(t) + \eta_1 \frac{d\gamma(t)}{dt} \tag{3.3}$$

By integrating Eq. (3.3), the strain $\gamma(t)$ would approach the deformation for the pure elastic material τ/G_1 with the difference decaying exponentially:

$$\gamma(t) = \frac{\tau}{G_1}\left[1 - \exp\left(-\frac{G_1}{\eta_1}t\right)\right] \tag{3.4}$$

Thus, the creep compliance can be expressed as:

$$J(t) = \frac{1}{G_1}\left[1 - \exp\left(-\frac{G_1}{\eta_1}t\right)\right] \tag{3.5}$$

The Burgers model, comprising the association in series of the Maxwell model and the Kelvin-Voigt model is most widely used for the acceptable results obtained in many cases [69]. It has the following format:

$$J(t) = \frac{1}{G_0} + \frac{t}{\eta_0} + \frac{1}{G_1}\left[1 - \exp\left(-\frac{G_1}{\eta_1}t\right)\right] \tag{3.6}$$

The ink used in direct-write assembly of 3D structures is complex two-phase, multi-component, and concentrated colloidal gel. It is a special flocculated system, in which a gel network is formed by closely packed flocs. The resulting gels have a large volume fraction of particles well above the gelation threshold, a very high viscosity, and a finite

shear modulus. We assume that in linear viscoelastic region, the colloidal ink is a solid-like viscoelastic system. That means when stress applied, the gel can be deformed with time, and after stress released, the gel will recover to its original state gradually. Thus, a modified Burgers model with one free spring and two Kelvin-Voigt components connected in series, as illustrated in Figure 3.8 (d) will be used to fit the creep and recovery data. The different components of this model can be connected to specific gels microstructure evolution. The free spring in this model represents the instantaneous strain of overall gel network. The first Kelvin-Voigt component stands for the delayed strain of overall gel network. The second Kelvin-Voigt component indicates the delayed strain of floc structures. Here, we assume that the overall gels network deforms very fast, while the floc structures induced response to stress are relatively slow. The creep ($J_c(t)$) and recovery ($J_r(t)$) mathematical model can be expressed by Eq. (6.7) and (6.8).

$$J_c(t) = \frac{1}{G_0} + \frac{1}{G_1}\left[1 - \exp\left(-\frac{G_1}{\eta_1}t\right)\right] + \frac{1}{G_2}\left[1 - \exp\left(-\frac{G_2}{\eta_2}t\right)\right] \tag{3.7}$$

$$J_r(t) = \frac{1}{G_1}\left[1 - \exp\left(-\frac{G_1}{\eta_1}t'\right)\right]\exp\left[-\frac{G_1}{\eta_1}\left(t - t'\right)\right] + \frac{1}{G_2}\left[1 - \exp\left(-\frac{G_2}{\eta_2}t'\right)\right]\exp\left[-\frac{G_2}{\eta_2}\left(t - t'\right)\right] \tag{3.8}$$

where t' is the time point when the stress is released, and creep phase changed to recovery phase.

3.3.5 Creep and recovery compliance

Figure 3.9 shows the experimental results of compliance function, J(t) as a function of time is for the same set of Al_2O_3 gels used in the stress sweep measurements. Hence, the nine data sets represent iteration at the three ϕ_{solids} values of 0.45, 0.47, and 0.49 with

each having PEI = 0.010, 0.014, and 0.018 wt%. Since each gel has a unique value of G'_{eq} and τ_c, a common magnitude of stress in the creep tests was not selected. Rather, a stress in the range of $\tau = 0.8\ \tau_c$ to $0.9\ \tau_c$ was selected for each ink.

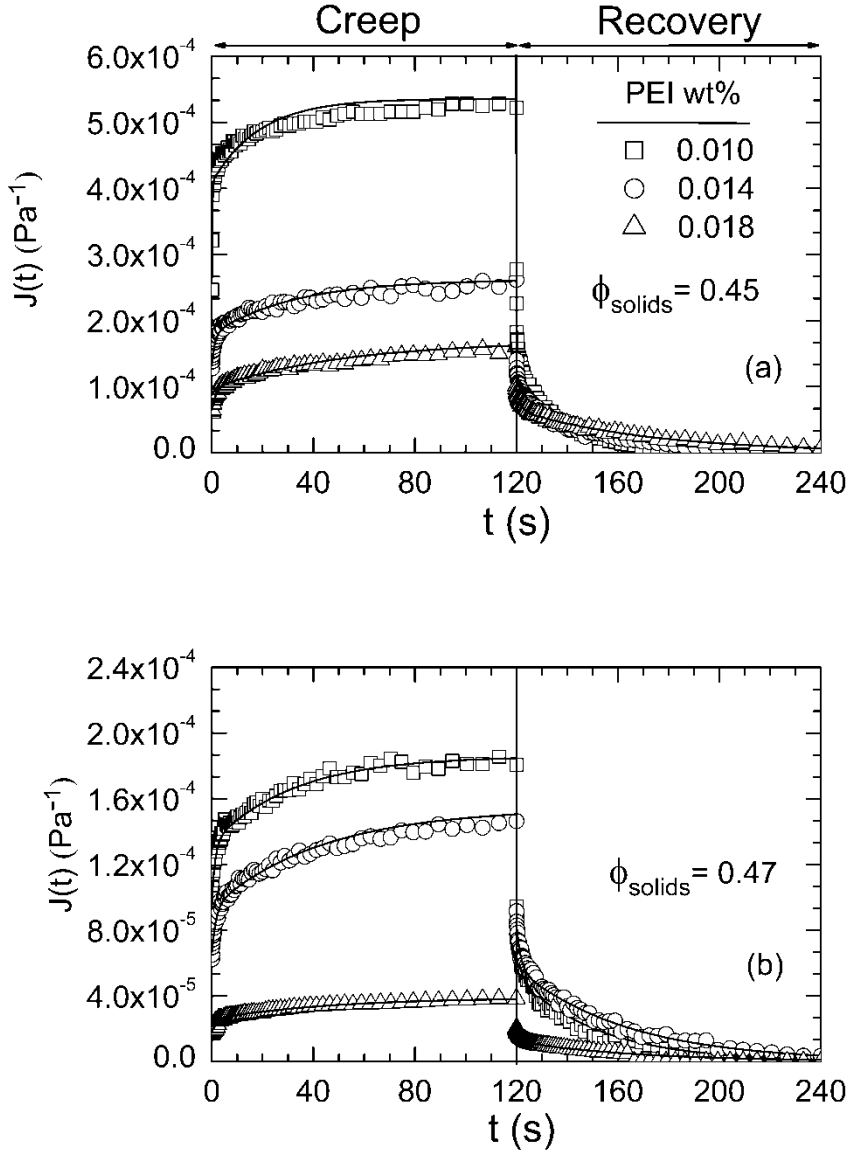

Figure 3.9 Compliance J(t) of Al_2O_3 gels plotted for creep and recovery experiments as a function of PEI wt% and ϕ_{solids} = (a) 0.45, (b) 0.47, and (c) 0.49.

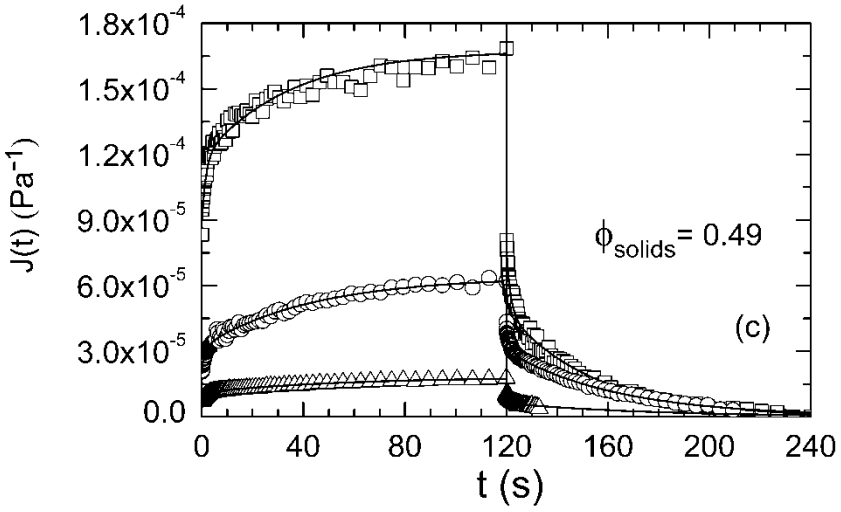

Figure 3.9 Compliance J(t) of Al_2O_3 gels plotted for creep and recovery experiments as a function of PEI wt% and ϕ_{solids} = (a) 0.45, (b) 0.47, and (c) 0.49.

In these curves, the time-dependence of the compliance J(t) resembles logarithmic growth in the creep experiment and exponential decay in the recovery experiment. The differences between the various PEI wt% are quite clear: the creep deformation is much larger for the low PEI wt% than for high one. In addition, at fixed PEI wt%, increasing the ϕ_{solids} reduces the creep deformations. However, the influence of PEI wt% on the creep deformation is much more sensitive than that of ϕ_{solids}. Similar observation was recorded during the stress sweep measurements.

The continuous lines drawn in Figure 3.9 are the results of fitting the creep and recovery data to our previous proposed mechanical model and the fitting parameters are summarized in Table 1. The column $1/G_0$ represents the instantaneous unit stress deformation at t=0. The decrease observed in $1/G_0$ when the PEI wt% is increased from 0.010 to 0.018 is an indication of the colloidal gels network shift from weak floc

structures at low ionic strength to flocculated structures at high ionic strength. The columns $1/G_1$ and $1/G_2$ represent the maximum potential unit stress deformation of two Kelvin-Voigt components. Both of them have the same change trend as $1/G_0$.

Table 3.1 Fitting parameters of creep and recovery model

ϕ	PEI wt%	$1/G_0 \times 10^{-5}$ (Pa^{-1})	$1/G_1 \times 10^{-5}$ (Pa^{-1})	$1/G_2 \times 10^{-5}$ (Pa^{-1})	η_1/G_1 (s)	η_2/G_2 (s)	r^2
	0.010	6.81	6.81	4.23	0.17	18.87	0.996
0.45	0.014	3.33	1.15	2.07	1.23	32.26	0.994
	0.018	1.28	0.67	1.44	1.67	52.63	0.993
	0.010	3.28	1.15	1.77	1.32	32.26	0.991
0.47	0.014	1.65	0.69	1.52	1.61	43.48	0.995
	0.018	0.32	0.15	0.41	1.96	47.62	0.992
	0.010	2.98	0.96	1.65	1.61	34.48	0.996
0.49	0.014	0.56	0.24	0.80	1.69	43.48	0.954
	0.018	0.14	0.08	0.14	1.72	55.56	0.936

The columns η_1/G_1 and η_2/G_2 represent the characteristic relaxation times of two Kelvin-Voigt components, respectively. The relaxation time η_1/G_1, on the order of few seconds, corresponds to the first Kelvin-Voigt component. The relaxation time η_2/G_2, on the order of tens of seconds, corresponds to the second Kelvin-Voigt component. There is no clear trend in these data; however they are still similar to the recovery times found in previous work on concentrated $BaTiO_3$ gels using an oscillatory type measurement. [40]

Table 3.2 Compliance percentage of each model component

ϕ_{solids}	PEI wt%	J_{FS}%	J_{KV1}%	J_{KV2}%
	0.010	38.15	38.15	23.70
0.45	0.014	50.84	17.56	31.60
	0.018	37.76	19.76	42.48
	0.010	52.90	18.55	28.55
0.47	0.014	42.75	17.88	39.38
	0.018	36.36	17.05	46.59
	0.010	53.31	17.17	29.52
0.49	0.014	35.00	15.00	50.00
	0.018	38.89	22.22	38.89

The full mechanical characterization of this system can be established by calculating the contribution of each component of the model, at the maximum deformation (i.e., t = 120 s) to which the system is subjected. The percentage deformation of each component of the model can be calculated by

$$J\% = \frac{J_{component}}{J_{sum}} \times 100 \tag{3.9}$$

where $J_{component}$ is the corresponding component compliance: free spring compliance $J_{FS} = 1/G_0$; the compliance of the first Kelvin-Voigt component, which can be expressed as:

$$J_{KV1}(120) = \frac{1}{G_1}\left(1 - \exp\left(-120\frac{G_1}{\eta_1}\right)\right) \tag{3.10}$$

, and the compliance of the second Kelvin-Voigt component, which can be expressed as:

$$J_{KV2}(120) = \frac{1}{G_2}\left(1 - \exp\left(-120\frac{G_2}{\eta_2}\right)\right) \tag{3.11}$$

J_{sum} is the summation of all components compliance. The compliance percentage of each component is reported in Table 3.2.

3.4 Summary

For Al_2O_3 inks prepared in this work, PAA was adsorbed on the particle surface to promote stabilization. The zeta potential behavior of bare and PAA-coated Al_2O_3 particles in suspension was quantitatively described. Excess PAA had little effect on the colloidal stability. The bare particles displayed an IEP around pH = 8.3. The addition of the PAA shifted the IEP of the coated particles to pH = 4.6. A surface saturation of PAA was reached at 2.4 mg PAA/g Al_2O_3, as determined by the Potentiometric titrations measurements. In the chosen processing range, the PAA was ionized and provided sufficient colloidal stability to formulate suspensions.

The linear viscoelastic regions of Al_2O_3 colloidal gels have been determined by stress sweep tests. The viscoelastic measurements show that the alumina gels are usually more elastic within larger flocculant/dispersant ratio and solid fraction. Creep and recovery analyses disclosed internal structure dynamics of colloidal gels system. Creep-recovery curves were fitted to a modified Burgers model. This allowed us to simulate the viscoelastic behavior using this mechanical model. From the parameters values of this model, the elastic and viscous contributions to the general viscoelastic behavior were analyzed for each solid fraction and each flocculant/dispersant ratio. On this basis, the Al_2O_3 colloidal gels viscoelastic studies were complete.

CHAPTER 4 THIXOTROPIC RHEOLOGY OF COLLOIDAL INKS

4.1 Introduction

Previous studies have attributed the equilibrium shape deformation to the equilibrium elastic modulus of ink materials [4]. Despite the accuracy of this method in describing the equilibrium shape of deposited structures, it is still uncertain how the complex rheology of colloidal inks will affect dynamic shape evolution of as-deposited structures. The equilibrium rheology of colloidal inks in a steady state has been described by using Hershel-Bulkley model, and the corresponding extrusion flow dynamics has been predicted [54]. The simulation results indicated that extrudate was in a state of non-equilibrium only during extrusion and recovers at once upon deposition. However, recent studies such as, direct flow visualization, finite element modeling, and classical fluid mechanics indicated that the colloidal structure is actually in a state of transition during extrusion and afterwards [70, 71]. Moreover, previous experience showed that both the extrusion flow in the capillary tube and the shape evolution after deposition occurs only in several few seconds [4]. It can be deduced that the short duration unsteady state flow behavior is of significance in this case. The thixotropic rheology of colloidal inks over shorter time scales seems to be critical important from the perspective of colloidal structures evolution during flow dynamics and after deposition.

Thixotropy is defined as a decrease of viscosity under constant shear stress or shear rate as a function of time, and followed by a gradual recovery when the shear is removed [72]. Although thixotropic fluids have found widely industrial applications, it is still hard to provide an exact definition of thixotropy that can be extensively accepted due to their complex mechanisms [72-74]. Various thixotropic models have been developed to describe the thixotropy behavior by combining the thixotropic assumption and the constitutive equation of a Non-Newtonian fluid, and most of them can be found in the reviews [72-75]. Generally, these models can be divided into two approaches: direct microstructural approach, and indirect microstructural approach. The direct microstructural approach is based on a description of the density of transient entanglements or of the aggregation of particles. While the latter one is based on a scalar parameter equation representing the change of structural breakdown and rebuild. Currently, structural kinetic theory is a more general approach to describe the thixotropic rheology based on microstructure dynamics. Moore [76] first introduced a scalar structural parameter to explain the flow behavior of ceramic pastes. Cheng and Evans [77] extended it to account for the thixotropic materials. From then on, the structural kinetics theory was established and applied to different phenomenological models to investigate thixotropic rheology of a variety of purely viscous systems [12-17].

The previous chapter showed that concentrated colloidal inks generally display strong viscoelastic behavior. The viscoelastic system makes it difficult sometimes to distinguish the effect of thixotropy from that of viscoelasticity clearly [72]. Acierno et al., [78] first postulated a constitutive model based on a series of Maxwell elements, and this model was modified to combine with Jeffrey's model later [79]. These models extended the

linear viscoelastic mechanical analogs through a series of ideal springs and dashpots combination, and incorporate structural kinetic theory to describe the thixotropic rheology. Doraiswamy et al., [80] assumed that the concentrated suspensions have an initial elastic behavior before yielding and a purely viscous behavior afterwards. Mujumdar et al., [75] extended this model to describe the smooth transition of concentrated suspensions from an elastic dominated phase to a viscous dominated phase. Based on these works, Dullaert and Mewis [81] developed a general structural kinetics model for thixotropic colloidal suspensions to describe both structure-dependent elastic and viscous contributions of particles and medium.

Currently, structural kinetic models have been successfully applied to describe the thixotropic rheology of numerous colloidal dispersions or weakly flocculated suspensions with low solid volume fraction [75, 79-84]. And this is the first time to analyze the thixotropy of concentrated colloidal gels with viscoelastic properties using this method. In this chapter, concentrated Al_2O_3 colloidal gels were employed as a model ink material to investigate the thixotropic rheology as the first part of a series of shape evolution experiments. An innovative engineering model based on the structural kinetics theory was proposed to quantify viscoelastic thixotropy of Al_2O_3 colloidal inks. This relatively simple and practical model can be used to predict the dynamic rheology of the ink and found to be in good agreement with experimental results.

4.2 Experimental Procedure

4.2.1 Materials

Here, three concentrated Al_2O_3 colloidal gels of 49% solid volume fraction with varying PEI concentrations of 0.010, 0.014, and 0.018wt% were prepared following previous chapter's methods. At the beginning of each measurement, the sample was dominated by a pre-shear of 0.2 s^{-1} for 1 minute and then left undisturbed for 30 min to attain an approximately fully structured initial equilibrium state to avoid any pre-shear effect during gels preparation.

4.2.2 Rheological measurements

Three common rheological test modes (i.e., start-up experiment, shear rate step-change experiment, and hysteresis loop experiment) were adopted to test the thixotropic behavior of model materials [72, 73, 75]. The first set of experiments consisted of a series of start-up shear flow of colloidal inks. A shear rates $\dot{\gamma}$ was applied to static state samples abruptly and kept constant until steady state was reached. The second set of experiments consisted of a series of continuous shear rate step changes. The shear rate $\dot{\gamma}$ was suddenly increased or decreased from a previous steady state to a new value until reach a new steady state. All measurements were maintained for 1 min, which was sufficient to attain the steady state in all cases. The third set of experiments consisted of hysteresis loops with different sweep time, where the shear rate was linearly increased from none to $100s^{-1}$ and decreased to zero at the same speed. The corresponding shear stress was recorded for each measurement. Figure 4.1 shows the shear history schematics of shear rate step-change and hysteresis loop experiment.

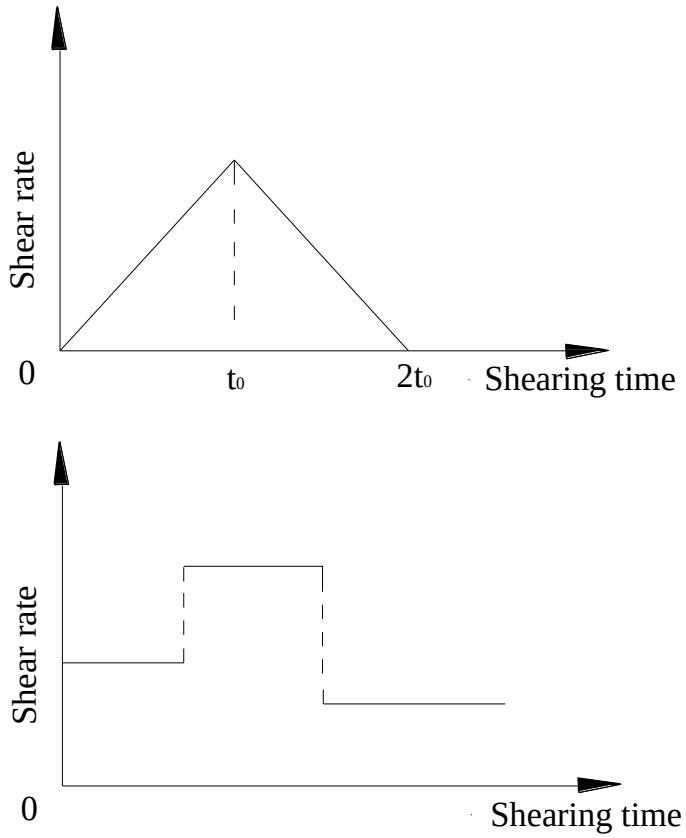

Figure 4.1 Schematic illustrations of (a) hysteresis loop and (b) shear-stress changes with time in shear-rate changes for a thixotropic material.

All measurements were performed under the Bohlin rheometer under the isothermal condition at 25^0C by digital temperature controller. A cup and bob measuring system (C14, Cup ID = 16mm and Bob OD = 14mm) with serrated wall was used to prevent the wall slip. Besides, to prevent water evaporation during the long periods required for measurements, a custom-made water trap was placed around the measuring device providing saturated atmosphere over the sample. In order to make sure the precision of the data, every measurement was repeated three times.

4.3 Development of Time Dependent Rheological Model

The thixotropic behavior of concentrated colloidal gels, depending on their internal structure changes with time under different shear rates has been linked theoretically to gel networks rupture, attrition and restructuring processes [9-12], as shown in Figure 4.2. From a microstructure perspective, gel network is a collection of closely packed flocs, which are fractal aggregation of colloidal particles. When the shear is imposed to gels, gels network will evolve due to the individual flocs deform with weak inter-flocs interactions and even rupture into smaller flocs until the structural changes reach dynamic equilibrium. When the shear is removed, small flocs will incorporate into larger ones, and the connection between flocs will reagglomerate toward its initial agglomeration degree. The rate of agglomeration and breakdown of flocs are determined by Brownian motion and shear history, which lead to the time dependent characteristics.

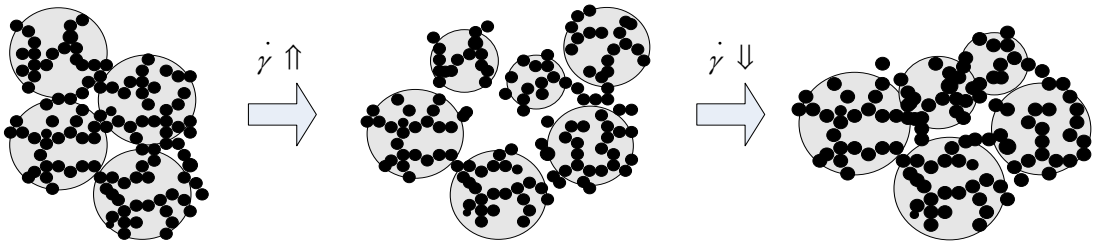

Figure 4.2 Schematic microstructure evolutions of colloidal gels with shear rate change. The larger circles indicate flocs in the gel consisted of gelled particles. The small dark circles indicate single particles.

4.3.1 Structural kinetics

We follow the classic structural kinetic theory to propose a normalized structural parameter, $\lambda\left(\phi_{solids}, \dot{\gamma}, t\right)$(i.e., $0 \leq \lambda \leq 1$), to describe the thixotropic behavior of the gel. For constant ϕ_{solids}, at any fixed location, it is considered to be a function of time t, and $\dot{\gamma}$ only. A fully structured gel has $\lambda = 1$, whereas a stable colloidal sol has $\lambda = 0$. The evolution of λ is assumed to be a first-order rate equation, analogue to reversible chemical reaction kinetics due to the flocs structure breakdown rate and agglomeration rate during the shear flow. The breakdown rate is assumed to be proportional to the instantaneous breakdown probability (i.e., λ), while the agglomeration rate is assumed to be proportional to the instantaneous agglomeration probability (i.e., $1 - \lambda$). Thus, the first-order kinetic equation can be written as [81, 85, 86]:

$$\frac{\partial\lambda\left(\dot{\gamma}, t\right)}{\partial t} = -K_b\lambda + K_a\left(1-\lambda\right) \tag{4.1}$$

where K_b is the overall breakdown rate constant, K_a is the overall agglomeration rate constant. The complete structural kinetics contains shear-induced breakdown, shear-induced agglomeration and Brownian motion induced agglomeration [81]. The breakdown rate is the product of collision frequency and probability of breakdown. Since collision frequency is proportional to $\dot{\gamma}$ [86, 87], K_b is assumed to be proportional to $\dot{\gamma}$ as [86]:

$$K_b = k_b\dot{\gamma} \tag{4.2}$$

where k_b is specific breakdown rate constant. The agglomeration rate should increase with the $\dot{\gamma}$ increase due to collision frequency and agglomeration probability increase. However, Gautham and Kapur [88] raised that higher shear rates will reduce the duration of collision significantly to make the agglomeration rate decrease eventually to zero. They [88] developed the agglomeration rate constant expression, based on Fan and Chen's assumption [87] as:

$$K_a = \frac{k_a^{'}\dot{\gamma} + k_0}{k_a^{''}\dot{\gamma}^{\rho} + 1} \tag{4.3}$$

where $k_a^{'}$ and $k_a^{''}$ are specific agglomeration rate constant, ρ is a exponential factor ($\rho > 1$), and k_0 is a Brownian motion induced agglomeration rate constant.

Once the colloidal system achieves equilibrium at a given $\dot{\gamma}$, the agglomeration rate will equal the breakdown rate of flocs, and the structure of the system will approach an equilibrium value characterized by a single equilibrium structural parameter λ_e. This dynamic balance can be expressed as:

$$K_a\left(1-\lambda_e\right) = K_b\lambda_e \rightarrow \lambda_e = \frac{K_a}{K_a + K_b} \tag{4.4}$$

By integrating Eq. (4.1) and substituting Eq. (4.4), the λ has the following form as:

$$\lambda = \lambda_e + \left(\lambda_i - \lambda_e\right)\exp\left[-\left(K_a + K_b\right)t\right] \tag{4.5}$$

where λ_i is the structural parameter value prior to the $\dot{\gamma}$ changes, (i.e., $\lambda\ (t = 0) = \lambda_i$).

4.3.2 Constitutive relationship

In this study, the Al_2O_3 colloidal gel was treated as a single-phase viscoelastic material with thixotropy. The elastic stress τ^{el} and the viscous stress τ^{vis} are decoupled as in Dullaert and Mewis model [81], and the total stress τ_{total} of flocs structure is the summation of these two terms as:

$$\tau_{total} = \tau^{el} + \tau^{vis} \tag{4.6}$$

The τ^{el} arising from the hydrodynamic interaction of the flocs, is assumed to obey a Hookean elastic response as:

$$\tau^{el} = G(\lambda)\gamma \tag{4.7}$$

where $G(\lambda)$ is a structural dependent shear modulus, and γ is the elastic strain. The $G(\lambda)$ is assumed to vary proportionally to the λ [79, 81] as:

$$G(\lambda) = \lambda G_m \tag{4.8}$$

where G_m is the maximum shear modulus before shear flow starts (i.e., $\lambda = 1$). The γ will increase linearly from zero to some critical strain γ_c when the shear flow starts, and remain constant as long as the deformation process continues in the same direction [80]. It can be expressed as:

$$\gamma = \gamma_c \left[1 - \exp\left(-m\dot{\gamma}t^{\alpha}\right)\right] \tag{4.9}$$

where m and α are characteristic parameters. For the simplicity, we define a maximum of elastic yield stress τ_y as:

$$\tau_y = G_m \gamma_c \tag{4.10}$$

The τ^{el} can now be written as:

$$\tau^{el} = \lambda \tau_y \left[1 - \exp\left(-m\dot{\gamma} t^{\alpha}\right)\right] \tag{4.11}$$

The τ^{vis} originating from the transient flocs network, consists of two terms: one describes the apparent viscosity decay $\eta_{de}(\lambda, \dot{\gamma})$ due to flocs structure breakdown, and the other describes the infinite apparent viscosity η_∞ at completely destroyed flocs structure (λ = 0). It can be given as:

$$\tau^{vis} = \eta_{de}(\lambda, \dot{\gamma})\dot{\gamma} + \eta_\infty \dot{\gamma} \tag{4.12}$$

The viscosity decrement term $\eta_{de}(\lambda, \dot{\gamma})$ is assumed to be proportional to λ and obey an exponential decay with the $\dot{\gamma}$ as [89]:

$$\eta_{de}(\lambda, \dot{\gamma}) = \lambda \eta_m \exp\left(-n\dot{\gamma}^{\beta}\right) \tag{4.13}$$

where η_m is zero-shear viscosity, n and β are material characteristic parameters. Hence, the constitutive equation can be written as:

$$\tau(\lambda, \dot{\gamma}) = \lambda \tau_y \left[1 - \exp\left(-m\dot{\gamma} t^{\alpha}\right)\right] + \lambda \eta_m \dot{\gamma} \exp\left(-n\dot{\gamma}^{\beta}\right) + \eta_\infty \dot{\gamma} \tag{4.14}$$

The instantaneous apparent viscosity η is defined as:

$$\eta = \frac{\tau_{total} - \tau^{el}}{\dot{\gamma}} = \lambda \eta_m \exp\left(-n\dot{\gamma}^{\beta}\right) + \eta_\infty \tag{4.15}$$

Eq. (4.15) can also be applied to the equilibrium states, so we can get equilibrium apparent viscosity η_e as:

$$\eta_e = \lambda_e \eta_m \exp\left(-n\dot{\gamma}^{\beta}\right) + \eta_\infty \tag{4.16}$$

4.3.3 Estimation of parameters

There are twelve basic parameters in the proposed model, including five structural kinetic parameters k_b, $k_a^{'}$, $k_a^{''}$, ρ, and k_0; three steady state elasticity parameters τ_y, m, and α; and four steady state viscosity parameters η_m, n, β, and η_∞. All parameters are constrained to be positive.

Table 4.1 Model parameters for Al_2O_3 inks of ϕ_{solids} = 0.49 with varying PEI wt%

PEI (wt %)	0.010%	0.014%	0.018%
$k_b \times 10^3$	5.57	3.05	1.27
$k_a^{'} \times 10^3$	8.23	5.10	2.16
$k_a^{''} \times 10^4$	2.98	2.84	2.59
ρ	1.99	1.95	1.93
$k_0 \times 10^2$	5.58	3.70	1.79
τ_y (Pa)	70	164	245
m	13.47	16.58	18.25
α	1.54	1.46	1.36
η_m (Pa s)	580	1720	3400
n	2.458	3.088	3.597
β	0.198	0.170	0.153
η_∞ (Pa s)	1.199	1.688	1.960

During the estimation, some basic parameters can be combined as lumped parameters to estimate, such as $K_a = \frac{k_a^{'}\dot{\gamma} + k_0}{k_a^{''}\dot{\gamma}^{\rho} + 1}$, $K_b = k_b\dot{\gamma}$, and $\lambda_e = \frac{K_a}{K_a + K_b}$. These parameters were evaluated separately with various data to minimize possible mathematical coupling. Firstly, the steady state shear flow data are used to estimate η_m, n, β, η_∞, and λ_e. Secondly, a series of start-up shear flow and continuous step change shear rate data are used to estimate k_b, $k_a^{'}$, $k_a^{''}$, ρ, and k_0, combining with λ_e. Finally, the transient start-up shear flow data at very small shear rate (i.e. $\lambda \approx 1$) are used to estimate τ_y, m, and α. The estimated parameters obtained from above procedures are listed in Table 4.1. They can be used to validate the predictive capability of this model.

4.4 Results and Discussion

4.4.1 Steady state rheology

Figure 4.3 showed the structural kinetics parameters K_b, and K_a changes as a function of the $\dot{\gamma}$. As plotted, the higher PEI concentration results in lower K_b and K_a value in the entire $\dot{\gamma}$ range. Since higher PEI concentration leads to stronger strength between flocs, the stronger gels breakdown and agglomeration rates are slower than weak ones. Besides, K_b increases simply linearly along the $\dot{\gamma}$, while K_a shows initially increase until peak value and drop after that. When the $\dot{\gamma}$ is terminated, the K_a is equal to k_0 in that only Brownian motion induced agglomeration exists. As the $\dot{\gamma}$ increases from low to intermediate value, the shear induces higher collision frequency of flocs, which leads to K_a increase. As the $\dot{\gamma}$ increases from intermediate to high value, the shear induces both higher collision frequency and shorter collision duration of flocs, which leads to K_a

decrease. The peak of the K_a is the transition point, where agglomeration rate changes from increment to decrement with the $\dot{\gamma}$.

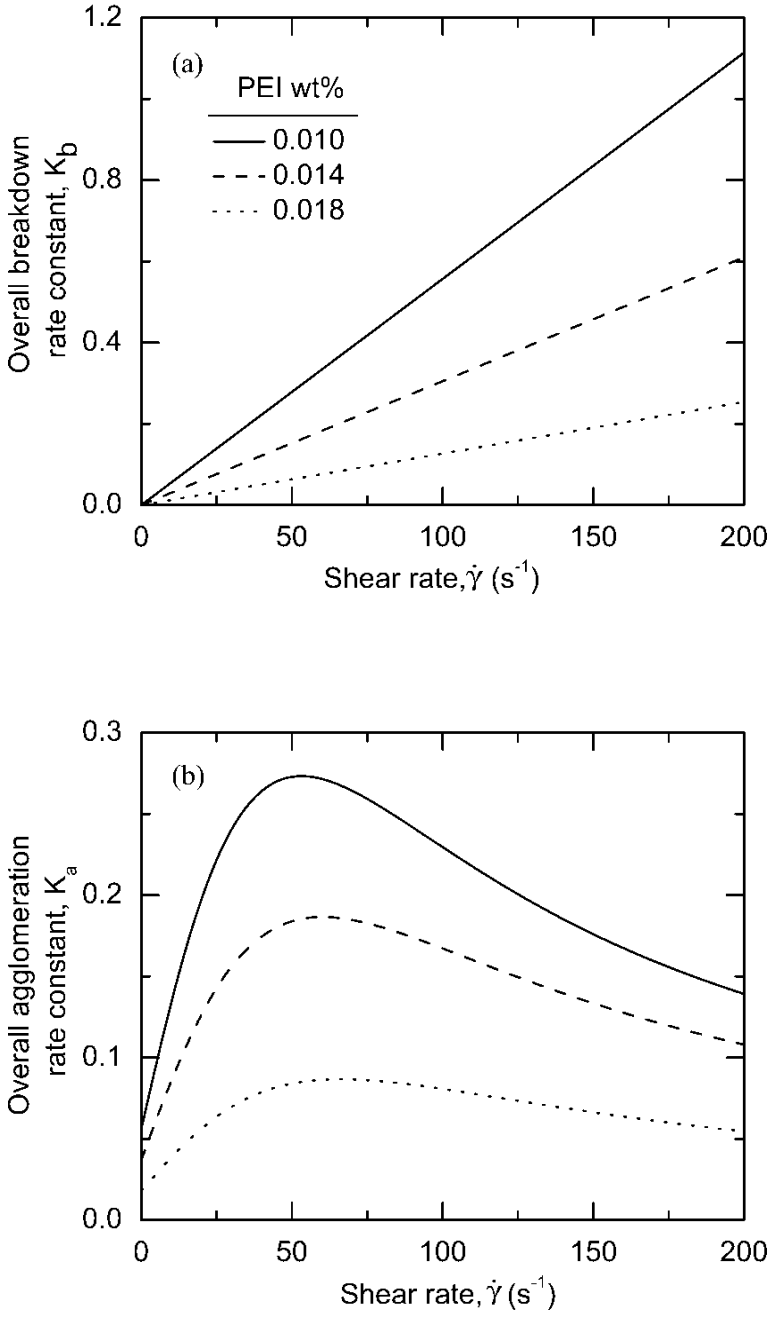

Figure 4.3 The variation of (a) overall breakdown constant K_b and (b) overall agglomeration constant K_a as a function of the shear rate $\dot{\gamma}$.

After obtaining the function of K_a and K_b, the λ_e can be calculated from Eq. (4.4), and the steady state flow curve can be predicted by substituting λ_e into Eq. (4.14). Since there are two variables of $\dot{\gamma}$ and t in the time-dependent rheological model, the equilibrium flow curve can eliminate the time evolution influence. The steady state rheological measurements were carried out by applying different constant shear rates to record the shear stress changes with time until equilibrium state.

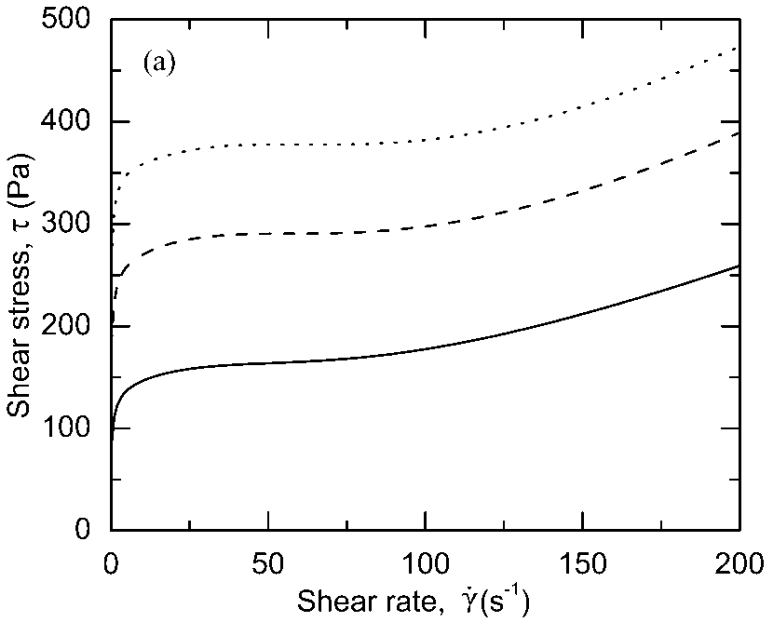

Figure 4.4 The steady state flow curves: (a) steady stress-shear rate curves, (b) steady apparent viscosity-shear rate curves.

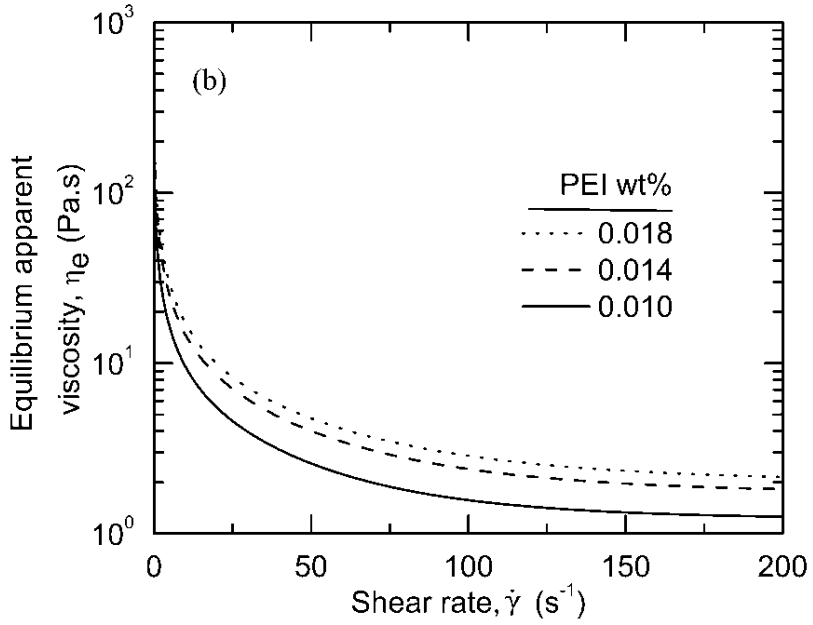

Figure 4.4 The steady state flow curves: (a) steady stress-shear rate curves, (b) steady apparent viscosity-shear rate curves.

As shown in Figure 4.4, the equilibrium flow curve shows a yield stress, and shear thinning behavior in the middle of measurement ranges. At higher $\dot{\gamma}$, the flow curve shows approximate Newtonian fluid characterization. The stronger gel shows higher yield stress, which implies a stronger elastic response. The higher PEI concentration also leads to higher shear stress at any instant $\dot{\gamma}$.

4.4.2 Hysteresis loops

Hysteresis measurements have been widely used as a tool to demonstrate the existence and extent of the thixotropic behavior of complex fluids. Early attempts to analyze thixotropic behavior were focused on qualitative or empirical concepts obtained from hysteresis-loop measurements [90]. The shape and area of the hysteresis loop have

been used to evaluate the thixotropic degree (i.e., larger area means larger thixotropic degree). However, hysteresis in flow curves is non-equilibrium behavior and hence highly dependent on the time span of the measurement [91].

Hysteresis loops, observed in Figure 4.5 confirms the thixotropic behavior of colloidal inks, when the shear rate was linearly increased from static state and subsequently decreased with the same speed to its initial value. The shear stress of the forward and backward curves encloses an area of hysteresis loops which indicates the thixotropy degree. These loops are positive, i.e., the up-curve is higher than down-curve, which indicates that the progressive breakdown of the ink structure under shear followed by its gradual recovery when the shear decreases. Figure 4.5 (a) revealed the variation in hysteresis loops with different PEI concentration under the same sweep time. Qualitative observation indicates that thixotropy increases with gel strength. Figure 4.5 (b) showed the sweep times influence to the hysteresis loops. As the sweep time increased, the loops area decreased, and especially the down-curve approached the steady state flow curves. Although the hysteresis loops are not accurate enough for modeling, they have verified the shorter time-dependent behavior of colloidal gels. The solid lines represent model predictions. By comparing with experimental results, the thixotropic rheology model showed excellent prediction ability.

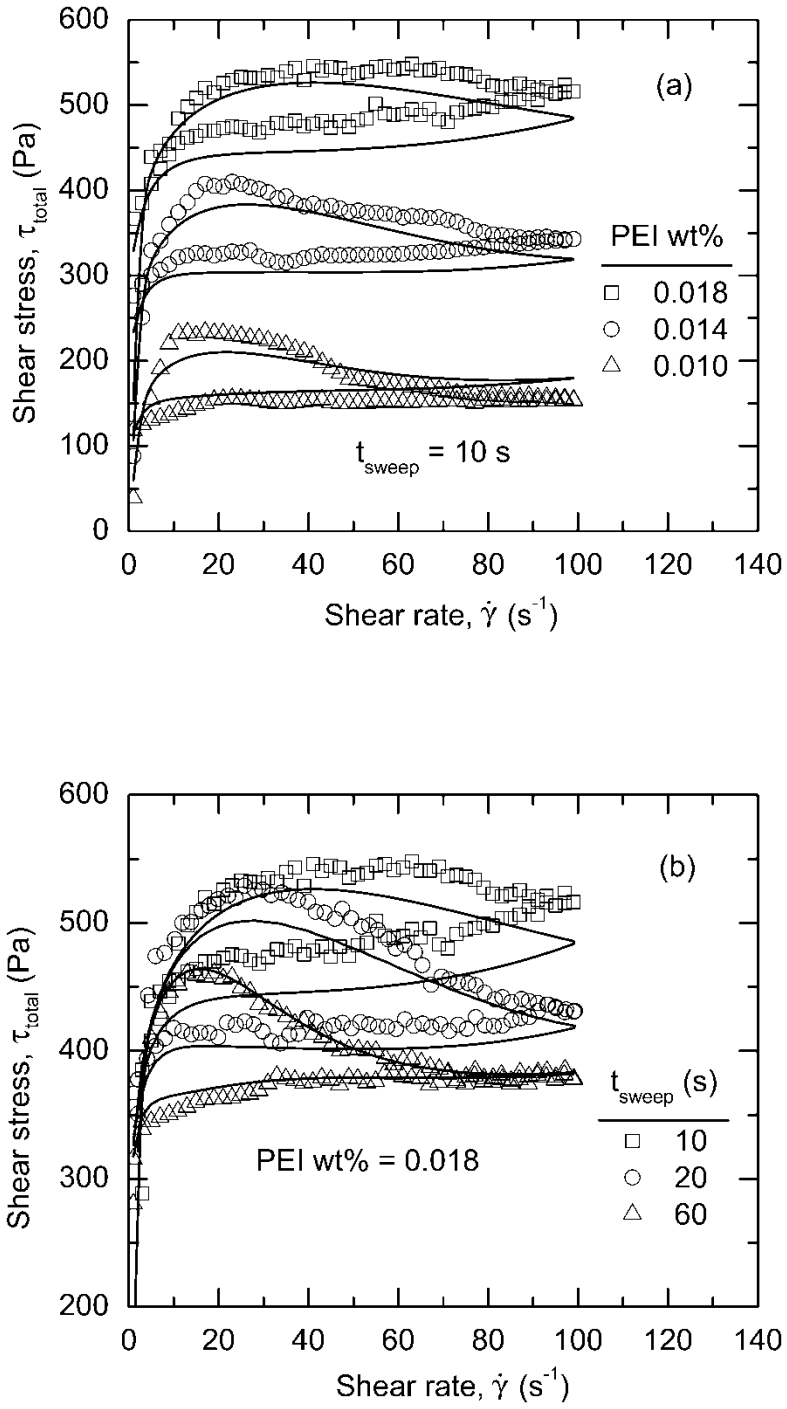

Figure 4.5 The hysteresis loops of experimental results comparing with model prediction: (a) varying PEIwt% at sweep time of 10 s, (b) at varying sweep times.

4.4.3 Breakdown and build-up curves

Although the above-described hysteresis experimental procedure was easy and quick to perform, it has the drawback that two variables of shear rate and time were continuously changed simultaneously. And it is difficult to establish whether the observed change in viscosity is due to time or to the change in shear stress. This makes it difficult to determine that the shear stress change is due to shear rate or time. Therefore, in order to counter this drawback, flow measurements at equilibrium were carried out by applying different constant shear stresses whereas the time evolution of the resulting deformation was monitored.

Figure 4.6 illustrated the continuous shear rate step change experimental results, compared with model predictions for Al_2O_3 inks with varying PEI concentrations. In Figure 4.6 (a), the shear rate was suddenly applied to static sample inks and continuous increased to 5, 30, 60, and 120s^{-1}. At each step, the shear rate was retained for 1 min to ensure to attain equilibrium. The initial shear stress overshoot was obvious, and relaxation time decreased as shear rate increased. Figure 4.6 (b) illustrated the shear stress as a function of shear rate step-down from initial 30 s^{-1} to 10, 5, 1, and 0.1 s^{-1}. The shear stress recovered very fast from initial undershoots. The prediction of the recovery curves is relatively poor with current model. This may be caused by the mechanical and measuring systems geometry error of the rheometer after large shear rates.

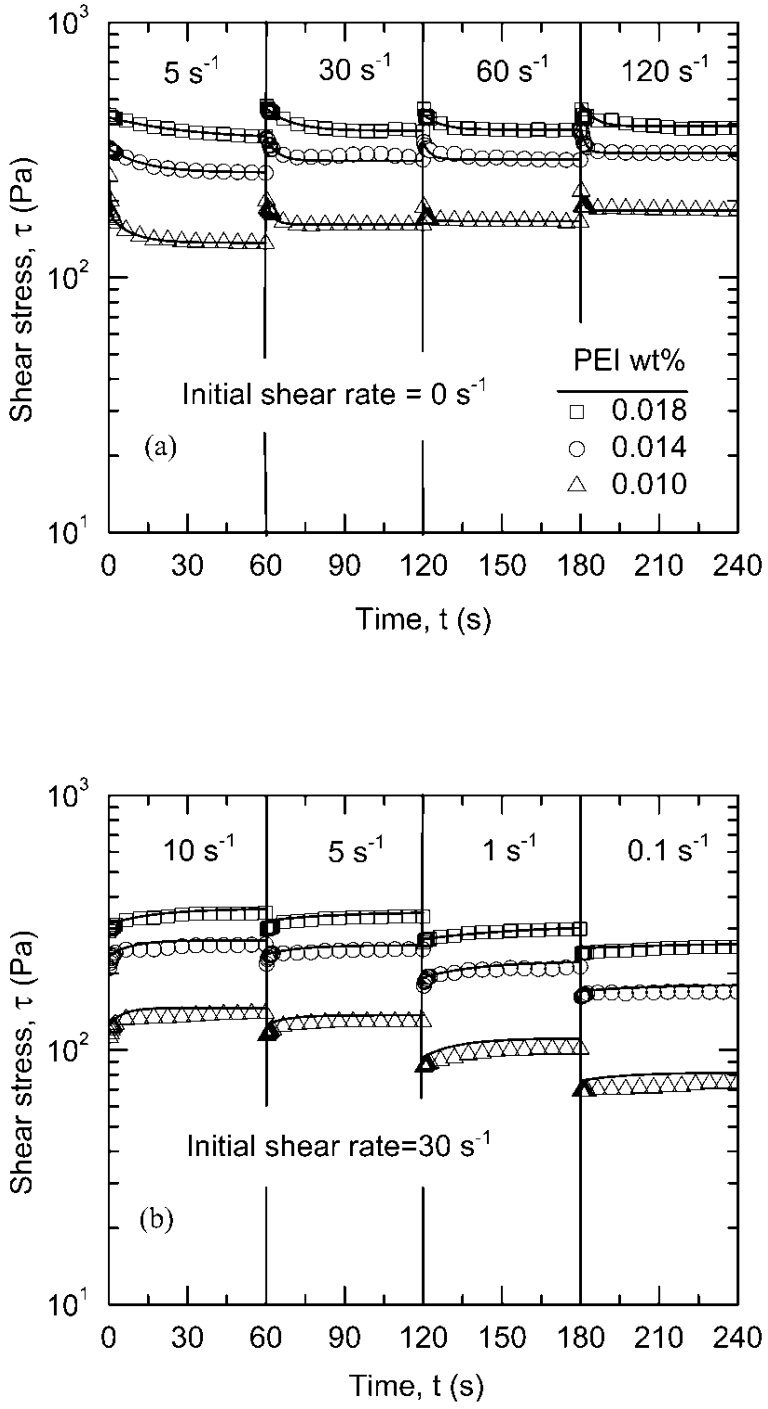

Figure 4.6 The shear rate step change of experimental results comparing with model prediction. (a) shear rate step-up measurements, (b) shear rate step-down measurements.

4.4.4 Start-up transient shear flow

In a next step, some features of this model will be assessed in more detail to discriminate the elastic and viscous contributions by analyzing the start-up transient flow curves. The shear stress produced displays an initial overshoot before reaching a steady state value. Due to the very fast destruction process, low shear rates were chosen, namely $\dot{\gamma}$ = 0.01 s^{-1}, 0.1 s^{-1}, and 1 s^{-1}. Besides, lower shear rates can dramatically decrease the relative importance of viscous properties.

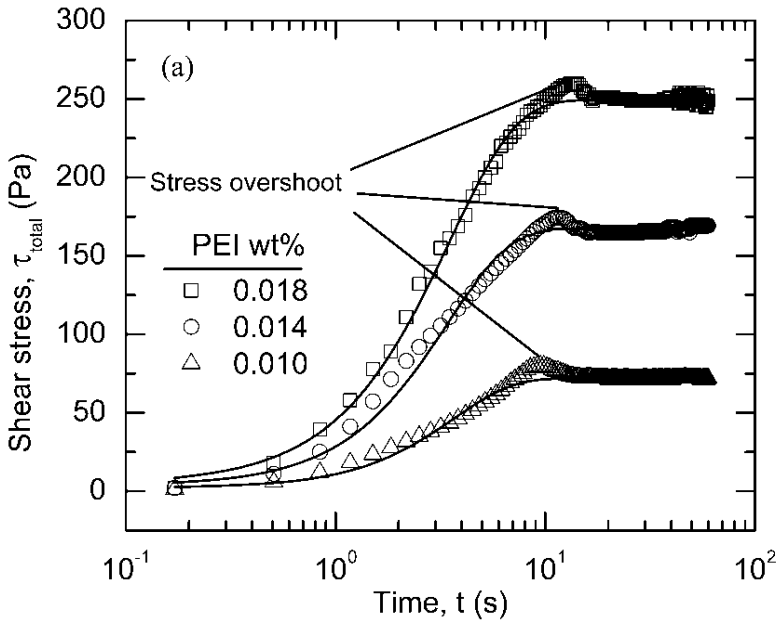

Figure 4.7 Start-up shear flow of Al_2O_3 inks of ϕ_{solids} = 0.49 and PEI wt% = 0.018 for $\dot{\gamma}$ = (a) 0.01s^{-1}, (b) 0.1s^{-1}, and (c) 1s^{-1}.

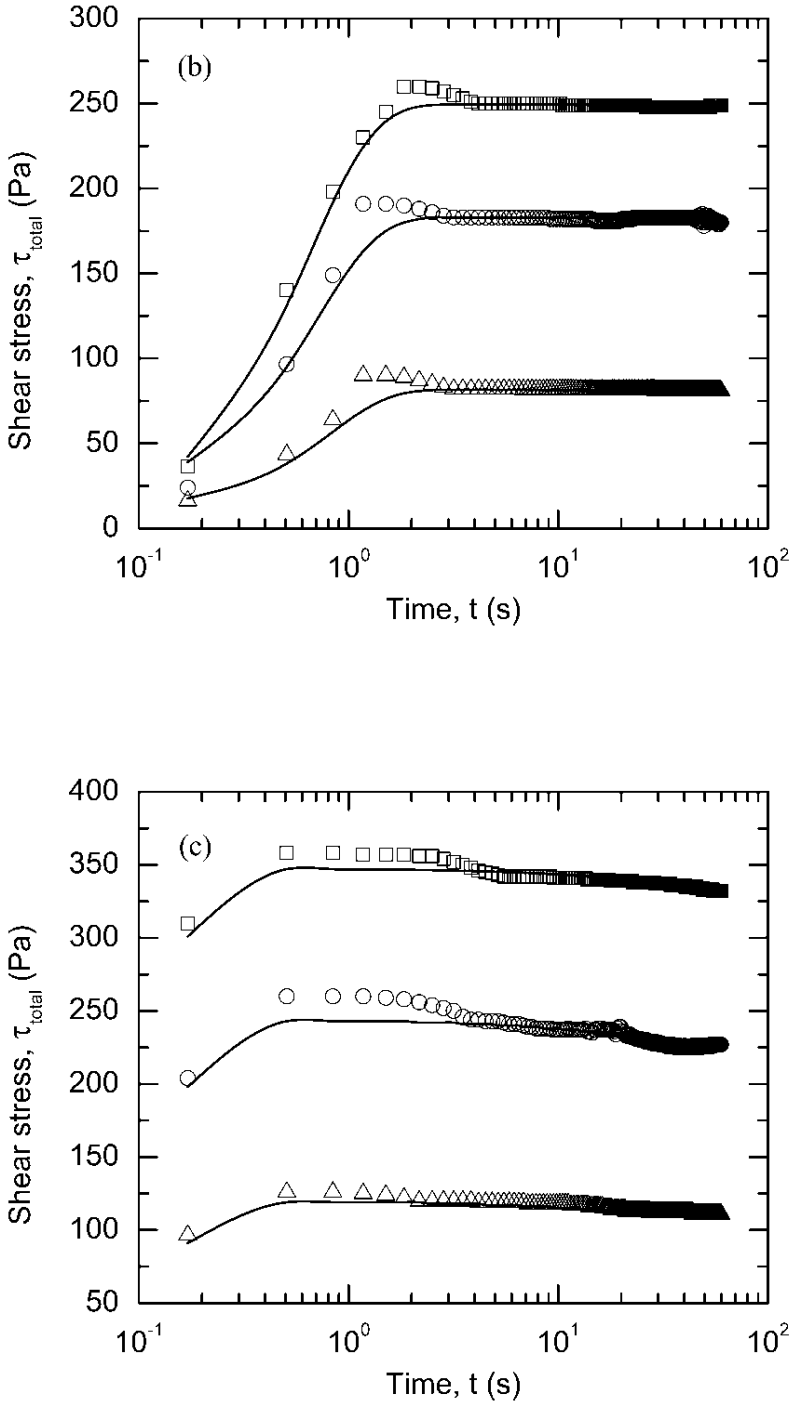

Figure 4.7 Start-up shear flow of Al_2O_3 inks of ϕ_{solids} = 0.49 and PEI wt% = 0.018 for $\dot{\gamma}$ = (a) $0.01s^{-1}$, (b) $0.1s^{-1}$, and (c) $1s^{-1}$.

Figure 4.7 demonstrated the shear stress evolution dynamics of Al_2O_3 inks with varying PEI concentrations under lower shear rates. In Figure 4.7 (a), the shear stress initially increases approximate linearly corresponding to an elastic deformation of the sample. As the shear proceeds, the elastic response transits from static to dynamic equilibrium. The same trends were also observed in Figure 4.7 (b), and (c). An overshoot is observed at shorter times, which indicates the presence of elasticity of colloidal gels. The overshoot before reaching a steady state value represents the transition of elastic properties. The overshoot value is somewhat larger than the yield stress, and cannot be tracked by current model. The overshoot point is also strongly related to the level of the imposed shear rate value. The larger the shear rate is, the earlier the overshoot advents. When the shear rate is large enough, the overshoot will disappear since the viscous properties are much more important than the elastic properties.

The data showed an increase in the maxima shear stress and a decrease in the corresponding times with increasing PEI concentrations. Another noticeable feature revealed by these experiments was the variation of the shear stress maxima as a function of shearing time and shear rate. The experimental data were found to be satisfactorily correlated by the hyperbolic form as:

$$\dot{\gamma} \cdot t \approx 10 \tag{4.17}$$

As expected, this also confirmed the existence of a critical shear strain as pointed out before and in agreement with the previous model assumptions.

4.4.5 Structural evolution after cessation of shear flow

After shear rates removed, the disrupted flocs can still aggregate at a specific rate with time toward the initially undisturbed value of structural parameter $\lambda_e = 1$. From Eq. (4.5) evolution of the structure parameter with no shear can be expressed by:

$$\lambda = 1 + (\lambda_i - 1)\exp(-k_0 t) \tag{4.18}$$

From Eq. (4.18), it can be seen that structural parameter increases with time from initial value of λ_i and approaches unity in the limit. It turns out that Eq. (4.18) permits simulation of the development of the structure after the ink deposited from the syringe tip, which is of importance to the final product quality.

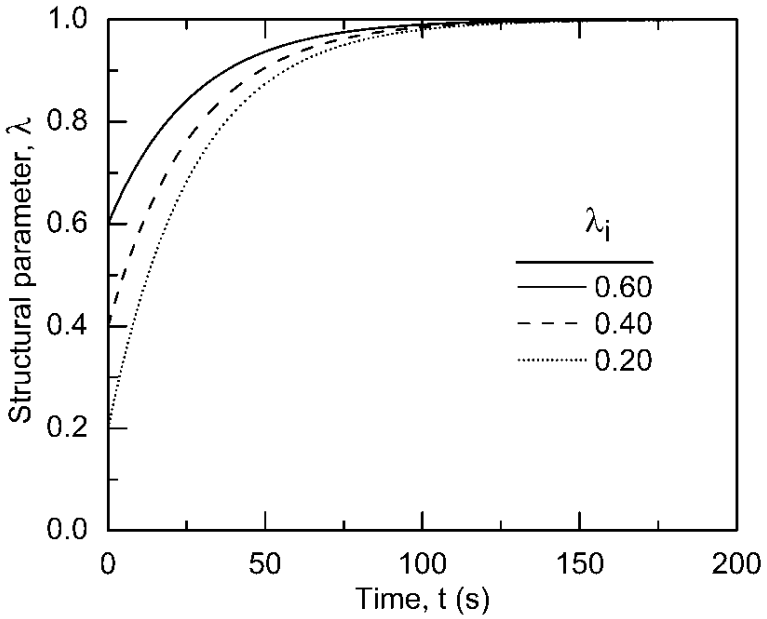

Figure 4.8 Structural parameter evolution of Al_2O_3 inks of ϕ_{solids} = 0.49 and PEI wt% = 0.018 after cessation of shear flow from different initial state.

In Figure 4.8, the evolution of λ with time after cessation of shear flow was computed from Eq. (4.17) for different initial values of λ_i. The λ increased rapidly at beginning, and gradually slowed down until reached the maximum value eventually. It is obvious that the structural recovery path depends on λ_i, which can be altered by the prior history of the ink.

4.5 Summary

This chapter is the first part of a comprehensive research carried out to evaluate the shape evolution of 3D structures fabricated by direct-write assembly. The systematic understanding of complex rheological behavior of colloidal gels used in SFF can provide necessary information for dynamic flow during deposition and structural recovery after deposition. From the foregoing data, the following conclusions can be made:

(1) The thixotropic rheology of Al_2O_3 colloidal gels have been observed and confirmed through shear rate step change, and hysteresis loops experiments. It provides a rational explanation for the dynamic shape deformation of deposited structures.

(2) By introducing the structural parameter changing with time, a generalized time-dependent single phase rheological model for concentrated colloidal gels with viscoelasticity has been developed and applied to the experimental results. The results are in agreement with the predicted values from the model. Our model is simple with few model parameters, and provides better overall simulation results.

(3) Colloidal gels strength has been considered as a factor influencing the thixotropic degree. The experimental data and simulation results have demonstrated that the colloidal gels with higher PEI concentrations have stronger thixotropy.

CHAPTER 5 STRUCTURE OF COLLOIDAL INKS DURING EXTRUSION FLOW

5.1 Introduction

The rheological behavior of colloidal inks depends on the composition and formulation. A typical colloidal ink comprises of particles, dispersant, binders, plasticisers, and liquid phase. Such inks normally dewater or phase-separate during extrusion process. This effect arises because the liquid phase may migrate significantly more rapidly than the dispersed phase (particles) under the application of a pressure gradient. The flow of colloidal gels invariably involves interactions at the interface between the material and walls. The material flow response is highly dependent on the interfacial characteristics of the boundary. During extrusion flow, the interfacial resistance naturally induces inhomogenities within the flow. These inhomogenities in the flow produce complex stress and shear rate fields within the bulk of the flowing ink. The development of the slip layer produces a lubricating effect, making flow easier and not representative of the bulk material.

A number of extrusion flow dynamics of colloidal gels have been reported in previous studies. Morissette and Lewis [20, 92] first calculated the shear rate profile in the extrusion filament by assuming the ink material as Newtonian fluids. Smay et al., [4] used Herschel-Bulkley model to simulated the capillary flow dynamics of PZT

colloidal inks and raised a core-shell architecture as a result of a radically varying shear stress within the extrusion nozzle. Roberts et al., [70] measured the flow profiles of colloidal gels of varying volume fraction in square microchannels by microscopic particle image velocimetry. Conrad et al., [71] investigated the structure and flow profiles of attractive colloidal suspensions in microchannels with direct imaging technique. All these investigations treat inks as time-independent materials, and the extrudate is in a state of non-equilibrium only during extrusion and recovers at once upon deposition. Besides, no-slip wall boundary conditions were always adopted in these studies for Newtonian or simple rheological fluids, and led to good agreement with experimental observations [4, 20, 70, 71, 92]. However, the rheologically complex fluids are known to violate the no-slip boundary conditions [93]. During the extrusion process, wall slip of the gel is thought to occur due to a thin solvent rich, but particle depleted layer near the deposition nozzle wall [45]. This phenomenon will significantly change the flow behavior in comparison to the flow under no-slip conditions, and lead to the different analysis results of colloidal structure evolution. These factors make it a challenge to characterize the structure and fundamental flow behavior for colloidal inks in extrusion process.

In our previous study, we developed a thixotropic rheological model to characterize Al_2O_3 colloidal gels by incorporating a time-dependent structural parameter. This model will be employed to simulate the inks flow dynamics and structure evolution. This paper is the second part of a series of shape evolution experiments and we still use Al_2O_3 colloidal gels as model materials. The flow dynamic simulation was first implemented into a 3D computer code to predict the isothermal flow field, yield surfaces, and distribution parameters in a capillary flow with no slip boundary conditions. Then a series

of extrusion pressure experiments were carried out to determine the wall slip effect to accurately convey the flow dynamics information. Finally, the flow dynamics will be associated with the microstructure of colloidal gels through a structural parameter quantitatively. These studies help the researchers in understanding the effects of properties of colloidal gels, the parameters of operations and their interactions in controlling filament formation and will be useful while optimizing a delivery system for extrusion process.

5.2 Mathematical Modeling and Numerical Simulation

In the deposition process, colloidal inks undergo a steady transition flow from a relatively low velocity within the barrel to the final extrusion velocity within the nozzle. Too high or too low extrusion velocity is meaningless for the mechanical limitations of the extrusion flow, and normal operation condition is to keep the extrusion velocity in the range of 2 ~ 20 mm/s. The flow type of the ink can be regarded as laminar plug flow for the low Reynolds number in this process.

5.2.1 Rheological model

The previously proposed time-dependent rheological model of Al_2O_3 colloidal gels consists of structural kinetics equation and constitutive equation. Since the extrusion flow keeps steady state during the deposition process, we use equilibrium rheological to carry out the CFD simulation. The equilibrium rheological model can be simplified as:

$$\begin{cases} \dfrac{d\lambda}{dt} = -K_b\lambda + K_a\left(1-\lambda\right) \Rightarrow \lambda_e = \dfrac{K_a}{K_a + K_b} \\ \tau\left(\lambda, \dot{\gamma}\right) = \left[\tau_y + \eta_0\dot{\gamma}\exp\left(-a\dot{\gamma}^{\alpha}\right)\right]\lambda_e + \eta_\infty\dot{\gamma} \end{cases} \tag{5.1}$$

Table 4.1 showed the parameters values used for defining the rheological constitutive relationship used.

5.2.2 Numerical simulation

In this case, the ink is assumed to be an incompressible fluid, with constant density and isothermal without heat exchange. By neglecting the inertia term, the mass and momentum conservation equations based on Navier-Stokes equation can be written as:

$$\frac{\partial u_i}{\partial x_i} = 0 \tag{5.2}$$

$$-\frac{\partial P}{\partial x_i} + \frac{\partial \tau_{ij}}{\partial x_j} = 0 \tag{5.3}$$

Inlet boundary condition is fixed velocity and outlet boundary condition is fixed pressure. Two wall boundary conditions are considered: no-slip boundary and slip boundary conditions with constant wall stress obtained by extrusion pressure measurements. The commercial program COMSOL Multiphysics 3.5a (COMSOL, Burlington, MA) was used to solve the governing equations. The resolution is based upon an iterative Newton scheme. Convergence is achieved when norm of the change in solution vector between successive iterations is less than 10^{-6}. All simulations in this paper were performed on Intel Pentium IV 2.0 GHz with 3 GB RAM PC machines.

5.3 Experimental Procedure

5.3.1 Materials

In this chapter, three concentrated Al_2O_3 colloidal gels of 49% solid volume fraction with varying PEI concentrations of 0.010, 0.014, and 0.018wt% were used, which are the same with the inks used in previous chapter for consistency.

5.3.2 Extrusion pressure measurement

The analysis of wall slip requires a precise determination of the true wall stress. Since the syringe barrel has a significantly larger diameter than that of the nozzle, it is important to correct the pressure loss at the entrance of the nozzle to specify the wall stress. Bagley correction [94] was performed here by using data from nozzles of same diameter but different length. The true wall stress τ_w after Bagley correction can be expressed as:

$$\tau_w = \frac{D\Delta P}{4\left(L_n + e\right)} \tag{5.4}$$

where e is the equivalent length caused by ends effect. And it can be determined by extrapolating ΔP versus the L_n curve to $L_n = 0$. Since the flow rate is another influence factor to the excess pressure drop due to these end effects [95], various deposition speeds $\bar{V}$ were performed. Here, we use apparent shear rate $\dot{\gamma}_a$ as controllable variable, and it can be related to the $\bar{V}$ as:

$$\dot{\gamma}_a = \frac{8\bar{V}}{D} \tag{5.4}$$

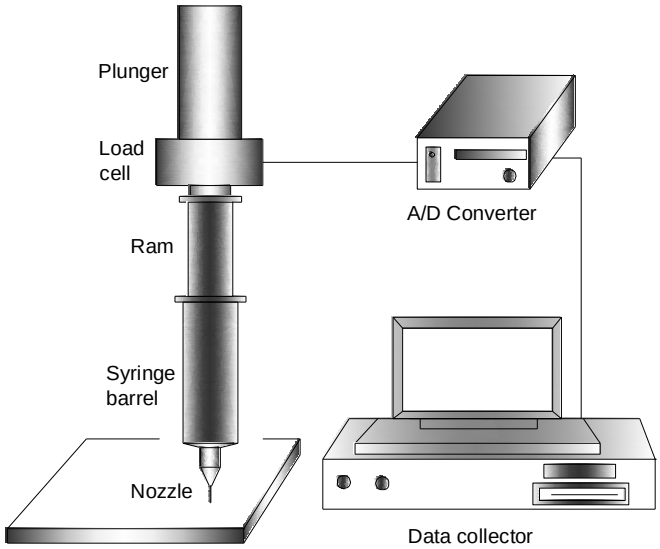

Figure 5.1 Schematic illustration of extrusion pressure drop measurement setup.

The extrusion pressures were measured by using a robotic deposition apparatus (Robocaster, Oklahoma State University, Stillwater, OK), a pressure transducer (load cell, LCGD 25, OMEGA Engineering Inc., Stamford, CT), and data conversion and acquisition systems. The sample material was loaded into a 3 ml syringe barrel (Nordson EFD, East Providence, RI) fitted with extrusion nozzles (Nordson EFD, East Providence, RI) with varying length. The plunger of robocaster was connected to the load cell, and pushed the ram downward to extrude the gel at a fixed velocity. The load cell between the plunger and the ram measured the applied force and transfer the data to the data acquisition system. Figure 5.1 illustrates the schematics of the experimental apparatus and setup. The interfacial friction generated between the ram and the syringe barrel walls is negligible compared to the extrusion load. The dimensions of the components and operation conditions were listed in Table 5.1.

Table 5.1 Dimensions of extrusion system and operation conditions

Syringe diameter, D_0 (mm)	9.6
Nozzle diameter, D (mm)	0.2
Nozzle length, L (mm)	6.3, 12.7, 19.1
Deposition speed, $\bar{V}$ (mm/s)	1, 2, 4, 8, 12

5.4 Results and Discussion

5.4.1 Bagley end correction

In Figure 5.2, the extrusion pressure drop ΔP of three gels was plotted as a function of nozzle length L_n under various apparent shear rate $\dot{\gamma}_a$. The ΔP values show excellent linear dependence on the L_n due to the small scatter of the results (less than 2%). The gel with higher PEI concentration, or under higher $\dot{\gamma}_a$ necessarily exhibits larger ΔP value.

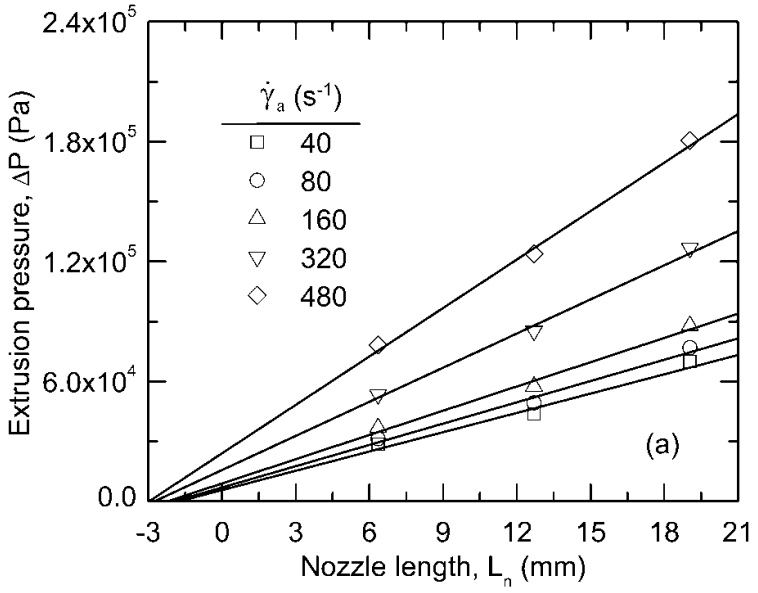

Figure 5.2 Bagley plots for Al_2O_3 colloidal inks of ϕ_{solids} = 0.49 with varying PEI wt% = (a) 0.010, (b) 0.014, (c) 0.018.

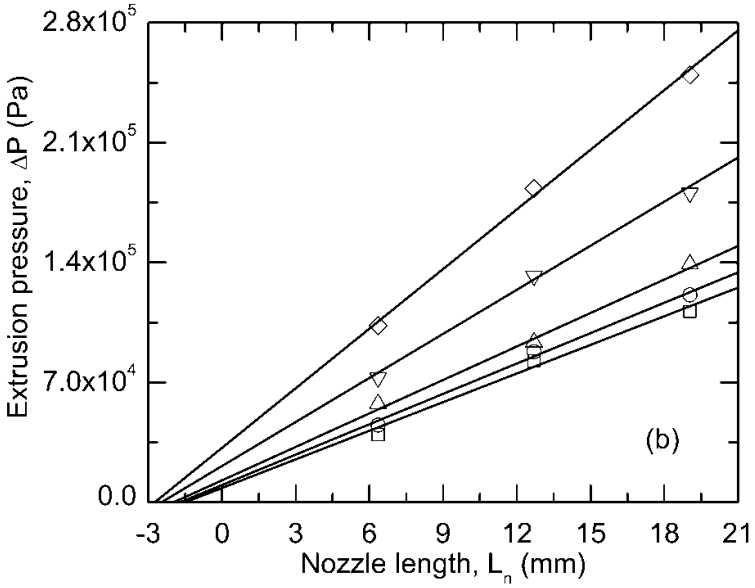

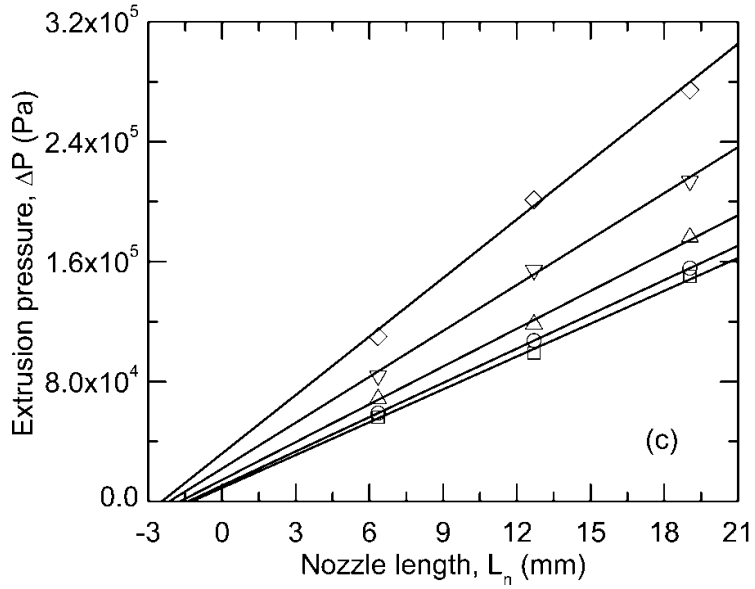

Figure 5.2 Bagley plots for Al_2O_3 colloidal inks of ϕ_{solids} = 0.49 with varying PEIwt% = (a) 0.010, (b) 0.014, (c) 0.018.

All three gels show negative intercepts on the nozzle length axis, and this intercept is equivalent length e in Eq. (5.4). As the $\dot{\gamma}_a$ is increased, the equivalent length e increases correspondingly. That means higher inlet flow rate can intensify the end effects at the contraction entrance. Besides, the slope of Bagley correction curves in Figure 5.2 also increases with the $\dot{\gamma}_a$. This qualitatively describes the wall stress increases with the inlet flow rate.

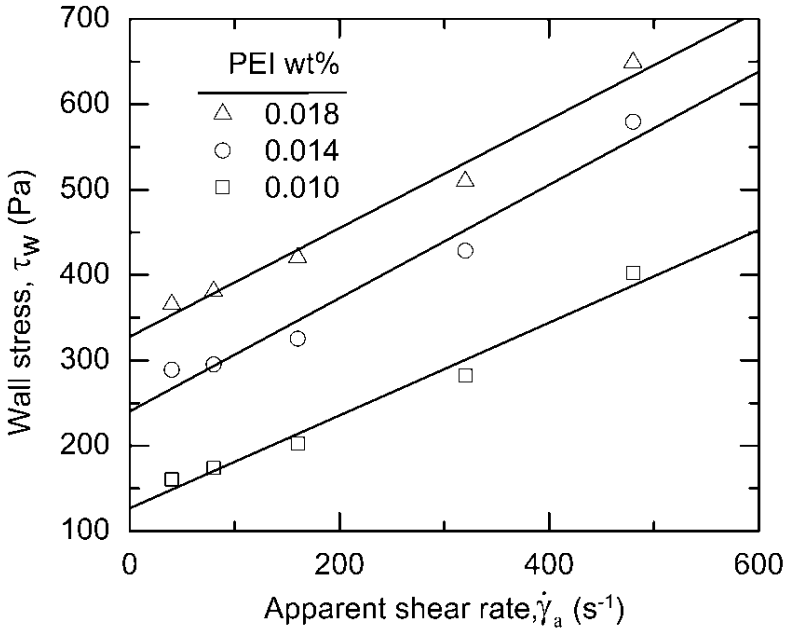

Figure 5.3 Computed wall stress τ_w as a function of apparent shear rate $\dot{\gamma}_a$ for nozzle length of L_n = 12.7 mm.

Due to the highly linear relationship between the ΔP and the L_n, Bagley correction can be successfully implemented according to Eq. (5.4) to compute the true wall stress τ_w at varying $\dot{\gamma}_a$. Figure 5.3 shows the computed τ_w change with the $\dot{\gamma}_a$ for three gels extruded from nozzles with length L_n = 12.7 mm. We can see that the τ_w also shows

approximately linear dependence on the $\dot{\gamma}_a$. That means the τ_w can be directly predicted through the $\dot{\gamma}_a$ for the nozzle with the same L_n.

5.4.2 Flow dynamics simulation

After getting the τ_w as a function of the $\dot{\gamma}_a$, the wall slip effects and bulk flow dynamics can be obtained and compared with the CFD simulation results with no slip wall conditions. Figure 5.4 shows the extrusion velocity *v* profiles as a function of the distance from the center x at the exit of the nozzle for varying $\dot{\gamma}_a$. Each flow profile is normalized by its deposition speed $\bar{V}$, and plotted against the dimensionless position in the nozzle x/D. The solid spot represents the simulation results from CFD with no slip wall conditions. The solid line represents the calculated results by using measured constant wall stress as boundary conditions. All the shape of flow profiles shows a solid-like core enclosed by a fluid-like shell. At lower $\dot{\gamma}_a$, $v_r/\bar{V}$ is constant across a large fraction of the diameter, indicative of behavior similar to plug flow. As the $\dot{\gamma}_a$ is increased, the core fraction shrinks, and shear flow in the shell region dominate the structure. Due to the wall slip effects, the significant improvement to the topology of the gels structure can be observed. And larger $\dot{\gamma}_a$ can lead to more significant wall slip, and is more pronounced for gels with higher PEI concentration. To better illustrate the change trend of the core region, the core fraction, r_c / R was plotted as a function of the $\dot{\gamma}_a$, as shown in Figure 5.5. The r_c / R shows a monotonic decrease with increasing $\dot{\gamma}_a$ for all three gels.

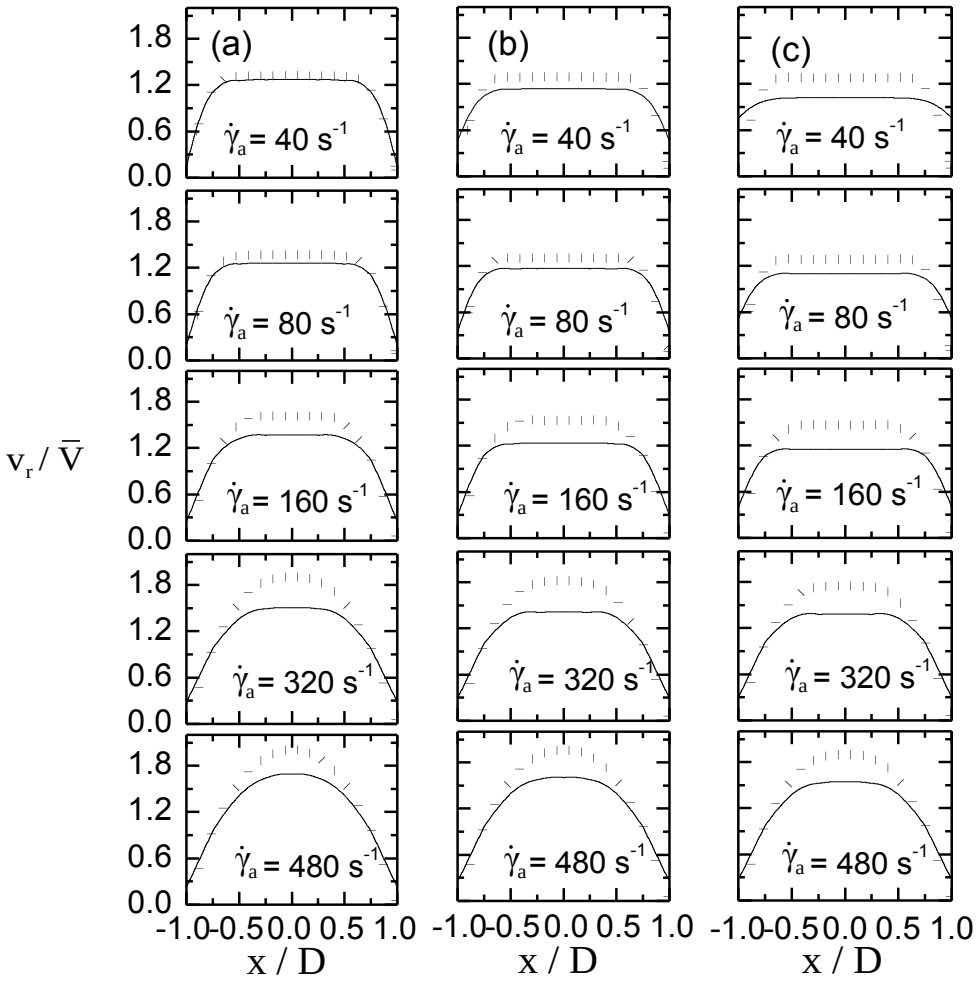

Figure 5.4 Dimensionless velocity profiles under various apparent shear rate compared with no-slip boundary condition CFD simulation results for Al_2O_3 gels of ϕ_{solids} = 0.49 with different PEIwt% = (a) 0.010, (b) 0.014, and (c) 0.018 extrusion flow in nozzles of L_n = 12.7 mm.

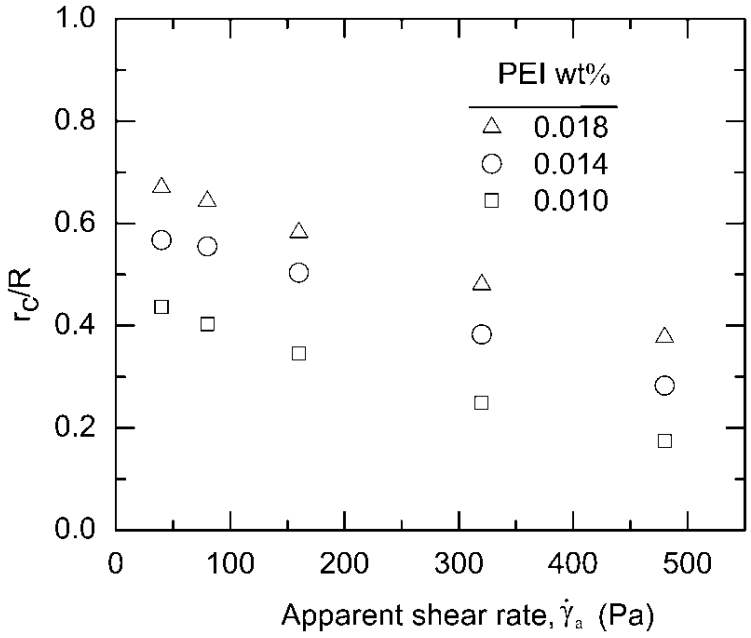

Figure 5.5 Core fraction as a function of apparent shear rate $\dot{\gamma}_a$ for Al_2O_3 gels of ϕ_{solids} = 0.49 with varying PEI wt% in nozzles of L_n = 12.7 mm.

Based on Smay's derivation [54], the total volume flow rate, Q can be calculated by

$$Q = \int_0^R 2\pi v_r dr \tag{5.6}$$

Integrating this equation by parts, we can get

$$Q = \pi R^2 v_s - \pi \int_0^R r^2 \left(\frac{dv_r}{dr} \right) dr \tag{5.7}$$

where $-\left(\frac{dv_r}{dr} \right) = \dot{\gamma}$. The radial shear stress τ_r is proportional to the radius r:

$$\frac{r}{R} = \frac{\tau_r}{\tau_w} \Rightarrow dr = \frac{R}{\tau_w} d\tau_r \tag{5.8}$$

Substituting equation (5.8) into (5.7) and rearranging it, we can get

$$\dot{\gamma}_a = \frac{4Q}{\pi R^3} = \frac{4V_s}{R} + \frac{1}{\tau_w^3}\int_{\tau_y}^{\tau_w} \tau_r^2 \dot{\gamma} d\tau_r \tag{5.9}$$

Figure 5.6 shows the wall slip velocity V_s as a function of the $\dot{\gamma}_a$. We can find the slip velocity also shows linear dependence on $\dot{\gamma}_a$ for three gels. As the apparent shear rate increased, the wall slip velocity also increases at the same rate. This relationship is only applicable in the experimental range, and cannot be extrapolated to the outside region.

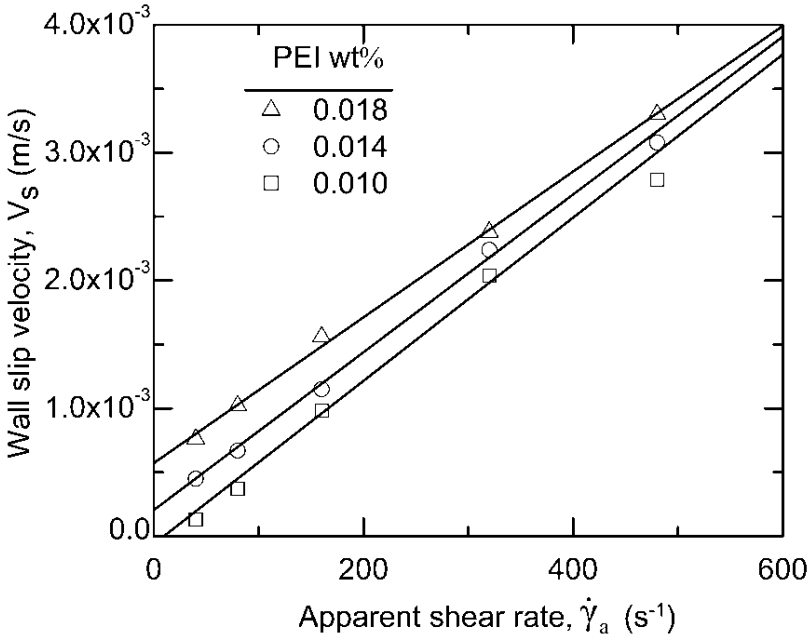

Figure 5.6 Computed wall slip velocity V_s as a function of apparent shear rate $\dot{\gamma}_a$ for L_n = 12.7 mm.

5.4.3 Structure dynamics of colloidal inks

Figure 5.7 shows the equilibrium structural parameter λ_e profiles of three gels as a function of normalized radius position at the nozzle exit under apparent shear rate. These structural parameter curves quantitatively describe gels structures breakage extent. For the same apparent shear rate, the gel with higher PEI concentration owns larger core region, and larger structural parameters at any position. For each gel, larger apparent shear rate leads to stronger structural breakage. At the lower apparent shear rate, there exists a core region and a shear-thinning region outside. At the higher apparent shear rate, the shear-thinning region shrinks very fast, and there is a Newtonian fluid-like region at the outside, where the structural parameter decrease very slow.

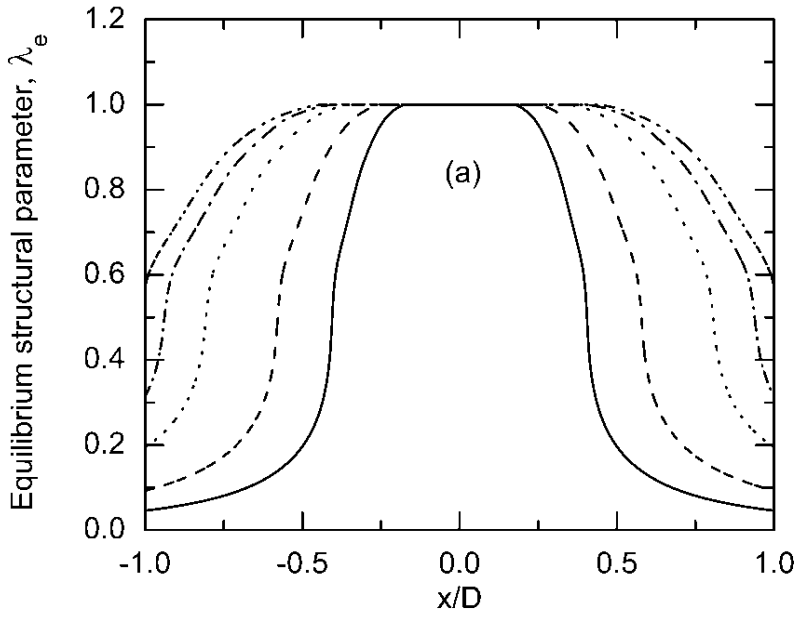

Figure 5.7 Structural parameter change profile under different apparent shear rate for Al_2O_3 gels of ϕ_{solids} = 0.49 with varying PEI wt% = (a) 0.010, (b) 0.014, (c) 0.018.

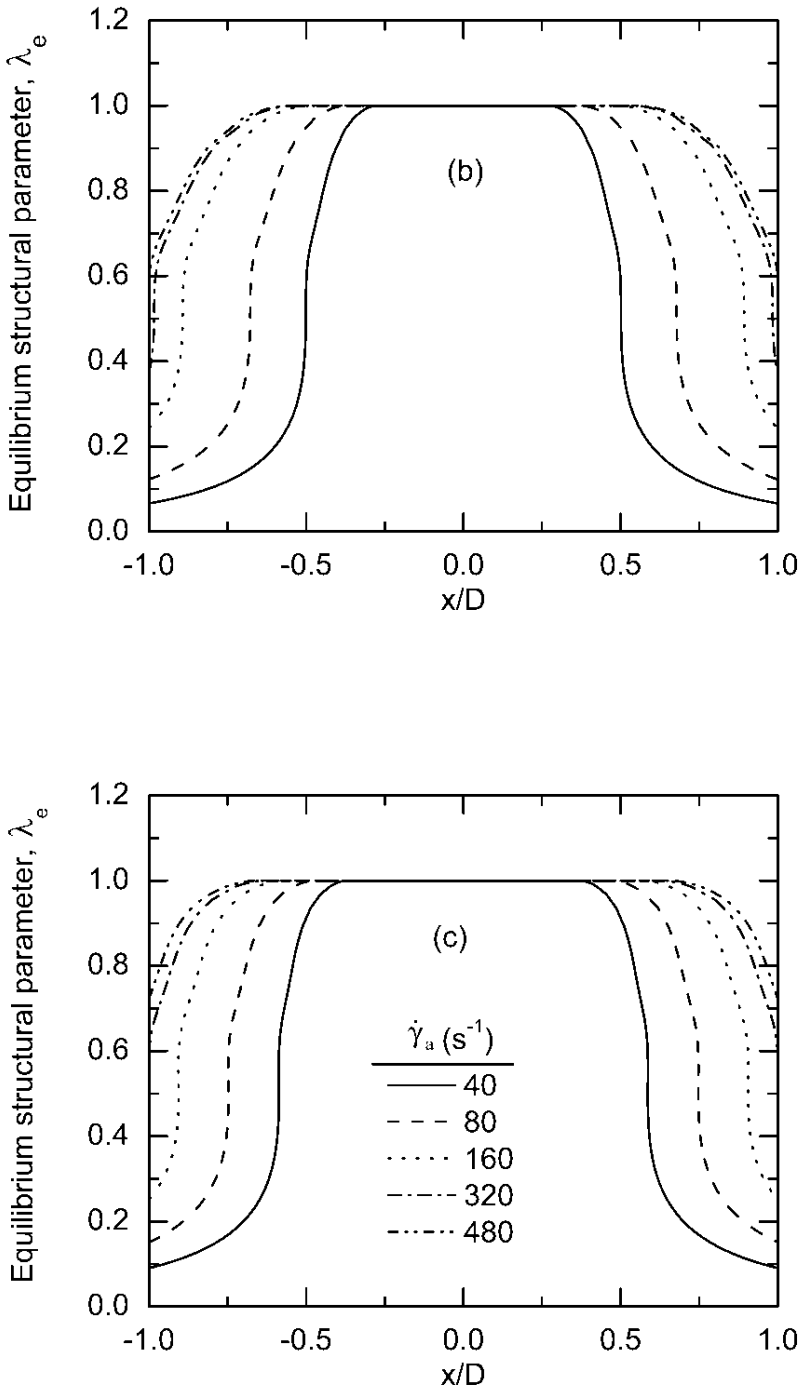

Figure 5.7 Structural parameter change profile under different apparent shear rate for Al_2O_3 gels of ϕ_{solids} = 0.49 with varying PEI wt% = (a) 0.010, (b) 0.014, (c) 0.018.

After deposition, the structure of the gel will recover from the initial equilibrium state (i.e., $\lambda_i = \lambda_e$) to fully structured state ($\lambda = 1$). Figure 5.8 shows the structural parameters recovery as a function of time after deposition at different radial position. The three gels are all deposited at $\dot{\gamma}_a = 480\ s^{-1}$, and start to reconstruct their network from time t = 0. The core region does not increase much after a long recovery time. The Newtonian region recovers relatively faster and at almost the same rate. In the shear thinning region, the recovery rate slows as the radial position decreases.

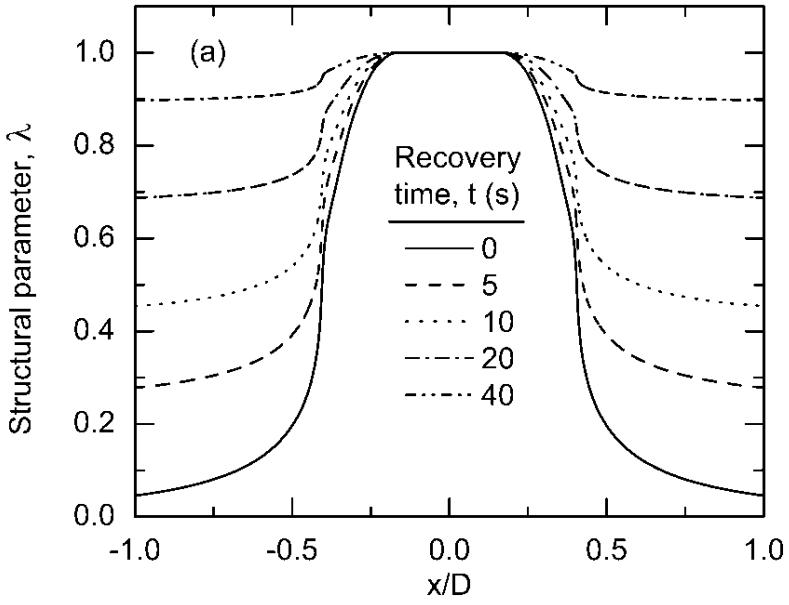

Figure 5.8 Structure profiles recovery after deposition as a function of time for Al_2O_3 gels of $\phi_{solids} = 0.49$ with varying PEI wt% = (a) 0.010, (b) 0.014, (c) 0.018.

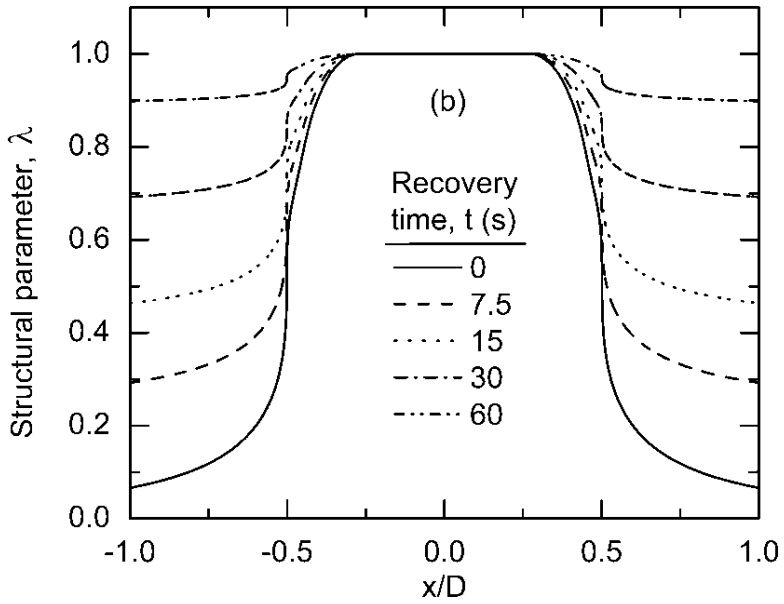

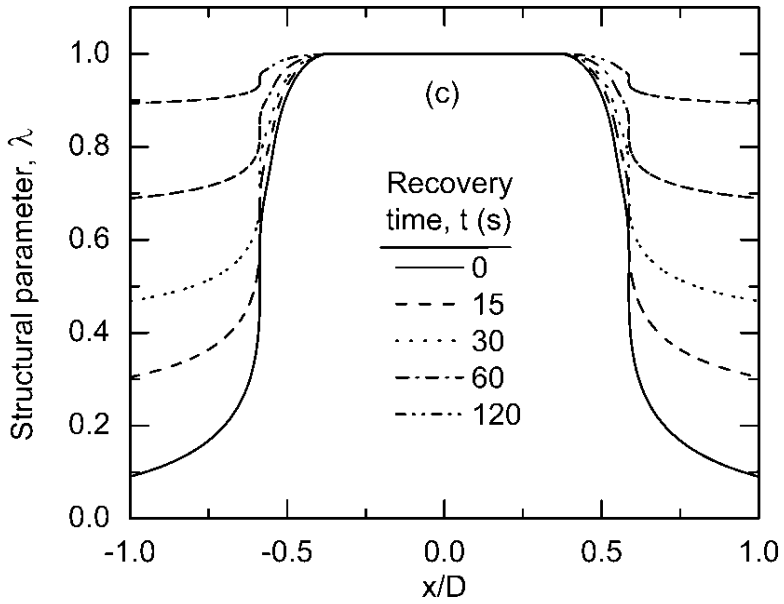

Figure 5.8 Structure profiles recovery after deposition as a function of time for Al_2O_3 gels of ϕ_{solids} = 0.49 with varying PEI wt% = (a) 0.010, (b) 0.014, (c) 0.018.

5.5 Summary

In this investigation, wall slip effect has been taken into account to accurately describe the flow dynamics of colloidal gels. A series of experiments using different diameters and lengths of capillary tips were conducted to measure the wall stress under different apparent shear rate. The analytical procedures for treating the experimental data are now well established, including the end correction effects by Bagley and subsequent treatment of wall slip phenomena. Based on the results of the experiments, a new method to predict the internal flow profile and slip velocity was proposed. The simulation results can convey the rheological information of the colloidal gels flow. The structural parameter was introduced to quantitatively describe the microstructure of the colloidal gels during extrusion process. These results offer new insight into the relationship between flow behavior and gels structure evolution.

CHAPTER 6 SHAPE EVOLUTION OF AS-DEPOSITED SPANNING ELEMENTS

6.1 Introduction

Currently, three basic periodic structures have been most widely assembled, including space filling layers, high aspect ratio walls, and spanning elements, as illustrated in Figure 6.1. Space filling layers require the deposited ink to form a continuous body without gap between layers. While, high aspect ratio walls need the deposited filament have spacing between individual layers exceeding filament width. Spanning elements set a series of spacing parallel layers to stack up, and the gap in underlying layers is bridged by overlying layers. In these structures, spanning elements are especially important due to its versatile applications in the areas of electronics [7, 8], composites [10, 13, 14], and biological science [96].

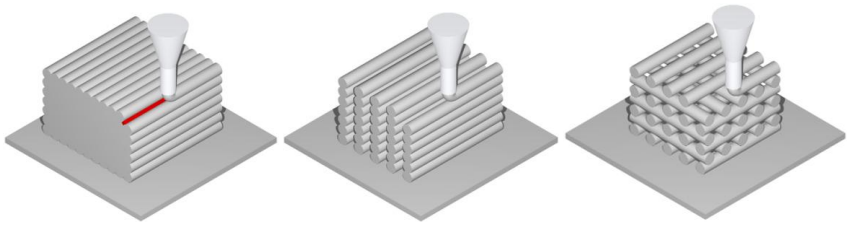

(a) (b) (c)

Figure 6.1 Schematic illusions of 3D periodic structures: (a) space filling layers, (b) high aspect ratio walls, and (c) spanning elements.

The deflection of suspended elements has been studied and modeled by a number of investigators. Smay et al., [4] first related equilibrium shear rheological properties of PZT inks to the shape of circular spanning filaments by applying static Euler-Bernoulli beam theory with an effective homogeneous modulus G'_{eff}. This ideal model was then applied to analyze the deflection of spanning filaments fabricated by ceramic inks [3, 15], organic inks [22], and fugitive inks [97]. Rao et al., [38] applied this model to investigate the deflection of hexagonal and square filaments. The relation of equilibrium shear properties to final shape is a simple view of the actual processes happening during the extrusion steps. During the extrusion, the ink must sustain the creep deformation caused by the extrusion pressure induced shear stress. The spanning elements inevitably undergoes sagging deformation due to capillary and gravity induced tensile stresses after deposition prior to the final solidification step [4]. Therriault et al., [17] modified this quasi-static Euler-Bernoulli equation to a dynamic form by replacing the elastic modulus with the time-dependent tensile creep compliance. However, this model can only provide good predictive values for high aspect ratio spanning filaments with length-to-diameter $L/D > 20$. There are two limitations, which make the beam theory inaccurate for predicting the deflection of spanning filaments from colloidal inks. Firstly, the mesoscale spanning filaments fabricated by direct-write assembly generally exhibit low aspect ratio (i.e., $L/D < 10$), which is beyond the beam theory assumptions (i.e., $L/D > 20$). Secondly, colloidal inks belong to viscoelastic materials, whose viscous properties were neglected in beam theory. During the deposition of spans, the extruding filament bends 90 degree upon exiting the nozzle to traverse the gap between to supports. That means the elements have both viscous flexibility and elastic flexural rigidity.

In this chapter, we first use dimensional analysis to reduce several process variables into dimensionless groups. An empirical equation was used to relate these dimensionless groups. By comparing with experimental data, this model was verified to be able to predict the maximum deflection of mid-span point. Then, we assumed that the instantaneous shape of spanning filaments resembles that of a viscoelastic catenary, and evolves with time. The dynamic evolution process is correlated to the viscoelastic characteristics of colloidal inks and operation parameters. A time-dependent viscoelastic catenary model was developed to simulate the dynamic shape evolution process. The simulation results were compared to previously experimental observations.

6.2 Empirical Modeling of Dimensional Analysis

6.2.1 Dimensionless Groups

Although previous simply supported beam model [4] is an idealized view of spanning phenomena, it is still possible to provide useful information about impact factors on deformation of spanning elements. When using this model to fit deflection profiles of spanning elements, the maximum deflection of mid-span δz_{mid} can be written as:

$$\delta z_{mid} = -\frac{5wL^4}{384EI} \tag{6.1}$$

In this model, the suitable G'_{eff} was selected to replace the G'. Although the relationship between G'_{eff} and other variables has been demonstrated, it is still not a direct method to disclose how the different factors influence the deflection degree of the spanning elements. Here, we assume that the effective elastic modulus G'_{eff} is the function of deposition speed $\bar{V}$ and equilibrium elastic modulus G'_{eq}. Therefore, deposition speed $\bar{v}$

(2 ~ 10mm/s), equilibrium shear modulus G'_{eq} (4×10^4 ~ 1.5×10^5Pa), span distance L (0.5 ~ 2.5mm), filament diameter D (~ 0.2mm), and gel density ρ_{gel} (~ 4.1g/cm^3) become important parameters on δz_{mid}.

In the case of all these variables, dimensionless analysis will reduce the number of variables to a more tractable set of dimensionless groups to characterize interrelationships. The Buckingham Pi method [98] is a systematic procedure for finding characteristic dimensionless groups associated with particular problem and then discovering functional relationships between these numbers. Three elementary dimensions (i.e., mass, length, and time) are taken to implement Buckingham Pi theorem, and there should be 3 (= 6 – 3) independent dimensionless groups. Three dimensionless groups are then defined as follows:

$$\pi_1 = \frac{\delta z_{mid}}{D} = \frac{\text{Midpoint deflection}}{\text{Filament diameter}} \tag{6.2}$$

$$\pi_2 = \frac{L}{D} = \frac{\text{Filament length}}{\text{Filament diameter}} \tag{6.3}$$

$$\pi_3 = \frac{\rho_{gel}\bar{V}^2}{G'_{eq}} = \frac{\text{Motion energy}}{\text{Elastic potential energy}} \tag{6.4}$$

Although the dimensionless groups are not unique, most of them still have a specific and explicit physical meaning. Physically, the first and second group indicates the deflection, and length of spanning filaments with respect to the filament diameter. The third group can be regarded as the ratio of motion energy and elastic potential energy.

6.2.2 Relations of dimensionless groups

Based on the above dimensional argument, three relevant dimensionless groups can be written as:

$$\frac{\delta z_{mid}}{D} = f\left(\frac{L}{D}, \frac{\rho_{gel}\bar{V}^2}{G'_{eq}}\right) \tag{6.5}$$

where f is an as-yet undetermined correlating function, which is either monomial or non-monomial form [99]. There are various possible forms of three dimensionless groups' combination. Firstly, the monomial (i.e., power series) form of f function was tried as:

$$\frac{\delta z_{mid}}{D} = y_0\left(\frac{L}{D}\right)^{y_1}\left(\frac{\rho_{gel}\bar{V}^2}{G'_{eq}}\right)^{y_2} \tag{6.6}$$

where y_0, y_1, and y_2 are constants to be determined. Generally speaking, in order to seek the dependence of one dimensionless group upon the others, one must keep the remaining groups constant and plot the curve of one group versus the others. In order to investigate the effect of L/D and $\rho_{gel}\bar{V}^2/G'_{eq}$ on $\delta z_{mid}/D$, their values were plotted while keeping another group constant in Figure 6.2.

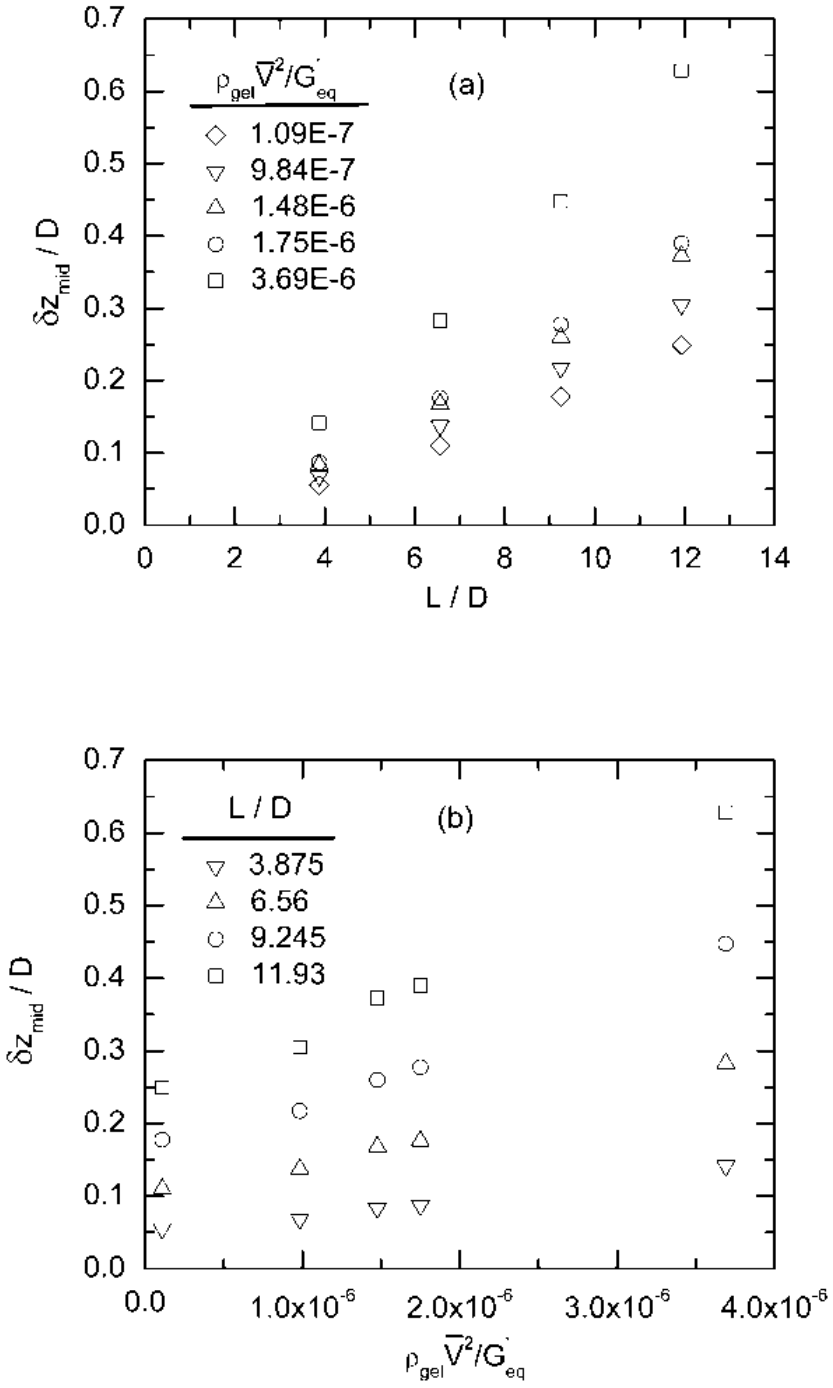

Figure 6.2 Relations between dimensionless groups (a) $\delta z_{mid}/D$ as a function of L/D by keeping $\rho_{gel}\bar{V}^2/G'_{eq}$ constant; (b) $\delta z_{mid}/D$ as a function of $\rho_{gel}\bar{v}^2/G'_{eq}$ by keeping L/D constant.

In Figure 6.2 (a), the $\delta z_{mid}/D$ shows a monotone increasing power function trend with L/D at different constant $\rho_{gel}\bar{V}^2/G'_{eq}$. In Figure 6.2 (b), the same trend of $\delta z_{mid}/D$ as a function of $\rho_{gel}\bar{V}^2/G'_{eq}$ at varying constant L/D except for the existence of intercept when $\rho_{gel}\bar{V}^2/G'_{eq}$ approaches zero. Then, the monomial Eq. (6.6) was modified to non-monomial form by adding another undetermined constant y_3 as follows:

$$\frac{\delta z_{mid}}{D} = y_0\left(\frac{L}{D}\right)^{y_1}\left(y_3 + \left(\frac{\rho_{gel}\bar{V}^2}{G'_{eq}}\right)^{y_2}\right) \tag{6.7}$$

The values of y_0, y_1, y_2, and y_3 were calculated from experimental data by using least squares regression, and listed in Table 6.1.

Table 6.1 Empirical constants obtained by least-square regression

y_0	y_1	y_2	y_3
1.24×10^{5}	1.33	1.28	7.19×10^{-8}

6.2.3 Validation and prediction of empirical model

Figure 6.3 showed the comparison of empirical model predictions with previous experimental data. It is clear from the figure that the model is in good agreement with experimental data and the deviations between the empirical model predictions and experimental data mostly fall into ±10% error ranges. Besides, Figure 6.4 illustrated the predicted values of $\delta z_{mid}/D$ as a function of both L/D and $\rho_{gel}\bar{V}^2/G'_{eq}$.

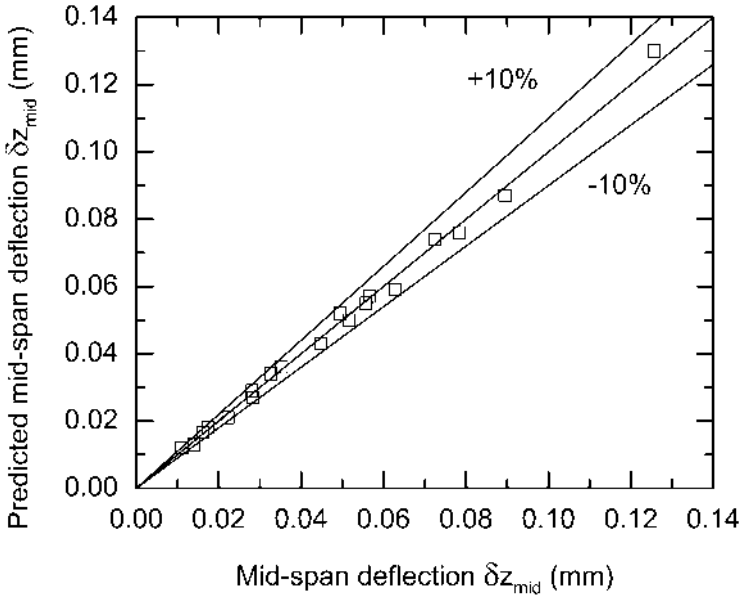

Figure 6.3 Comparison of model predictions with experimental data.

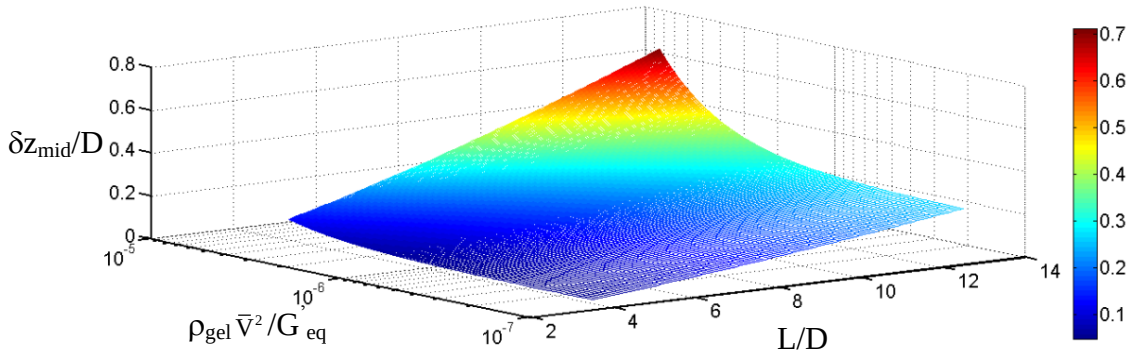

Figure 6.4 Model predictions as a function of dimensionless groups and compared with experimental data.

6.3 Mathematical Modeling of Viscoelastic Catenary

6.3.1 Bending moment of viscoelastic materials

The stress-strain behavior of a viscoelastic material under a constant tensile stress σ can be analogue to Kelvin-Voigt model with parallel combination of two ideal rheological elements, spring and dashpot, as illustrated in Figure 3.8 (b). The spring represents the elastic behavior, and the dashpot represents the viscous behavior of the material. The traction coefficient of the dashpot ξ is determined by the viscosity η with the relationship $\xi = 3\eta$. The relationship between the tensile stress σ_e and the tensile strain ε_e in the spring element is given by Hooke's law as:

$$\sigma_e = E \cdot \varepsilon_e \tag{6.8}$$

The relationship between the traction force σ_v and the traction strain ε_v in the dashpot element can make an analogy to shear flow constitutive equation of Newtonian fluid as:

$$\sigma_v = \xi \cdot \left(d\varepsilon_v / dt \right) \tag{6.9}$$

The total stress σ is the sum of elastic and viscous stress as:

$$\sigma = \sigma_e + \sigma_v = E \cdot \varepsilon_e + \xi \cdot \left(d\varepsilon_v / dt \right) \tag{6.10}$$

Since the total strain ε is equal to the ε_e and ε_v as:

$$\varepsilon = \varepsilon_e = \varepsilon_v \tag{6.11}$$

Eq. (6.10) can be rewritten as:

$$\sigma = E \cdot \varepsilon + \xi \cdot \left(d\varepsilon / dt \right) \tag{6.12}$$

Assuming that a plane cross section normal to the axis of the filament remains plane after bending, it can be easily shown by simple bending theory that at any section of the filament, the longitudinal strain ε can be expressed as:

$$\varepsilon = Y / R \tag{6.13}$$

where Y is the distance of surface from neutral axis, and R is the radius of curvature of the filament. Here, we set θ (s, t) as the kinetic angle of the tangent to the centerline with the horizontal, where s is the arc-length coordinate. By simply setting$\partial a/\partial b = a_b$, the curvature $d\theta/ds$ can be expressed as:

$$d\theta / ds = \theta_s = 1/R \tag{6.14}$$

Then, substituting Eq. (6.13) and (6.14) into Eq. (6.12), multiplying it by YdA, and integrating it over the section of the filament:

$$\int \sigma \cdot Y dA = E \cdot \theta_s \int Y^2 dA + \xi \cdot \theta_{st} \int Y^2 dA \tag{6.15}$$

where $\int \sigma \cdot Y\, dA$ is the bending moment M and $\int Y^2 dA$ is the area moment of inertia I. Thus, the M of viscoelastic filament can be expressed as [100]:

$$M = EI \cdot \theta_s + \xi I \cdot \theta_{st} \tag{6.16}$$

6.3.2 Viscoelastic catenary model development

The planar forces and moments analysis of the viscoelastic filament element is shown in Figure 6.5. The filament is assumed to be under uniformly distributed load. The length of the element ds can be separated into horizontal component dx, and vertical component

dy. The gravity force acting on the element can be expressed by the product of weight distribution w, and element length ds. At the lower end, there exist a tangential tension force T, a normal shear force N, and a counter clockwise direction bending moment M. At the upper end, there exist opposite direction tangential tension force T + dT, normal shear force N + dN, and bending moment M + dM, respectively. The bending slope at any position of the filament can be measured by slope angle θ. The derivation of viscoelastic catenary model follows the viscous catenary model derived by Teichman et al. [101].

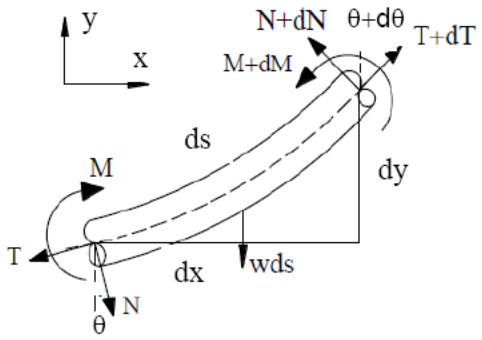

Figure 6.5 Forces and moments acting on an element of the filament.

Horizontal forces balance: $\sum F_H = 0$

$$\begin{aligned} &\frac{d}{ds}\left(T\cdot\cos\theta - N\cdot\sin\theta\right) = 0 \\ &\Rightarrow T_s\cdot\cos\theta - T\cdot\sin\theta\cdot\theta_s - N_s\cdot\sin\theta - N\cdot\cos\theta\cdot\theta_s = 0 \end{aligned} \tag{6.17}$$

Vertical forces balance: $\sum F_V = 0$

$$\begin{aligned} &\frac{d}{ds}\left(T\cdot\sin\theta - N\cdot\cos\theta\right) = 0 \\ &\Rightarrow T_s\cdot\sin\theta + T\cdot\cos\theta\cdot\theta_s + N_s\cdot\cos\theta - N\cdot\sin\theta\cdot\theta_s = w \end{aligned} \tag{6.18}$$

The tension force T, and shear force N in Eq. (6.17) and (6.18) can be expressed respectively as [102]:

$$T = \frac{w \cdot \cos\theta - N_s}{\theta_s} \tag{6.19}$$

$$N = \frac{T_s - w \cdot \sin\theta}{\theta_s} \tag{6.20}$$

By eliminating the tension force T in Eq. (6.19) and (6.20), we can get

$$2w \cdot \sin\theta + N \cdot \theta_s + \frac{N_{ss}}{\theta_s} + \frac{w \cdot \cos\theta}{\theta_s^2} - \frac{N_s \cdot \theta_{ss}}{\theta_s^2} = 0 \tag{6.21}$$

The universal relationship between shear force N and bending moment M has the form:

$$M_s + N = 0 \tag{6.22}$$

And previous derivation has showed the bending moment of viscoelastic filament in Eq. (6.16), so the Eq. (6.22) can be rewritten as:

$$N = -M_s = -\left(EI \cdot \theta_{ss} + \xi I \cdot \theta_{sst}\right) \tag{6.23}$$

Substituting Eq. (6.23) into Eq. (6.21), multiplying by cosθ, and integrating it, we can get

$$EI\left(\frac{\theta_{sss}}{\theta_s} \cdot \cos\theta + \theta_{ss} \cdot \sin\theta\right) + \xi I\left(\frac{\theta_{ssst}}{\theta_s} \cdot \cos\theta + \theta_{sst} \cdot \sin\theta\right) + w \cdot \frac{\cos^2\theta}{\theta_s} = f_1(t) \tag{6.24}$$

where $f_1(t)$ is a constant of integration. By setting θ = 0, Eq. (6.24) can be turned into

$$EI \cdot \frac{\theta_{sss}}{\theta_s} + \xi I \cdot \frac{\theta_{ssst}}{\theta_s} + \frac{w}{\theta_s} = f_1(t) \tag{6.25}$$

Substituting Eq. (6.23) into Eq. (6.19), the result can be written as:

$$EI \cdot \frac{\theta_{sss}}{\theta_s} + \xi I \cdot \frac{\theta_{ssst}}{\theta_s} + \frac{w}{\theta_s} = T(x,t) \tag{6.26}$$

Comparing Eq. (6.25) with (6.26), using the setting condition $\theta = 0$, we can get

$$f_1(t) = T(x,t) = T(0,t) \tag{6.27}$$

That means the tension force T (x, t) is only a time dependent variable as:

$$T_x = 0; T(x,t) = T(t) \tag{6.28}$$

Substituting Eq. (6.27), and (6.28) into Eq. (6.24), it turned into

$$EI\left(\frac{\theta_{sss}}{\theta_s} \cdot \cos\theta + \theta_{ss} \cdot \sin\theta\right) + \xi I\left(\frac{\theta_{ssst}}{\theta_s} \cdot \cos\theta + \theta_{sst} \cdot \sin\theta\right) + w \cdot \frac{\cos^2\theta}{\theta_s} = T(t) \tag{6.29}$$

Multiplying Eq. (6.29) by $\theta_s/\cos^2\theta$ and integrating it, we can get

$$\left(EI \cdot \theta_{ss} + \xi I \cdot \theta_{sst}\right) \cdot \sec\theta + ws = T(t) \cdot \tan\theta + f_2(t) \tag{6.30}$$

where $f_2(t)$ is a constant of integration. The symmetry determines that $\theta(0,\ t) = \theta_{ss}(0,\ t) = \theta_{sst}(0,\ t) = 0$, that means $f_2(t) = 0$. Besides, the boundary conditions at the supported ends are $\theta(\pm L/2,\ t) = 0$. Thus, Eq. (6.30) can be formulated as:

$$\left(EI \cdot \theta_{ss} + \xi I \cdot \theta_{sst}\right) \cdot \sec\theta + ws = T(t) \cdot \tan\theta \tag{6.31}$$

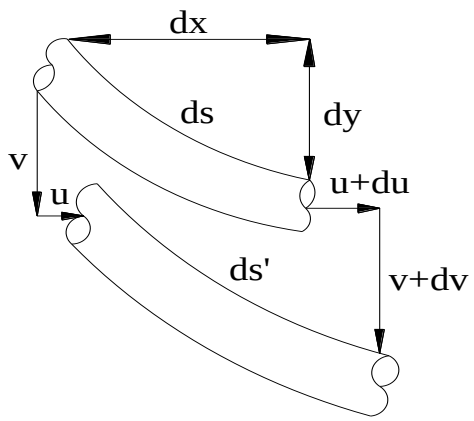

Figure 6.6 Time dependent displacement of an element of the filament [103].

In order to figure out the time-dependent expression for tension force T(t), we need to analyze the filament movement dynamics during shape evolution. Figure 6.6 shows the element movement during the filament sagging process. Setting u(x, t) is the horizontal displacement, and v(x, t) is the vertical displacement of a cross-section element at location x. If ds is the original length of the element, and ds' is its new length, they can be expressed respectively as:

$$ds^2 = dx^2 + dy^2 \tag{6.32}$$

$$ds'^2 = (dx + du)^2 + (dy + dv)^2 \tag{6.33}$$

For small to moderate deflection, $\theta < 1$, $s \approx x$, so that $v_x \approx \theta$. Corrected to the second order of small quantities, the filaments fractional change in length can be expressed as:

$$\left(\frac{ds' - ds}{ds}\right) = u_x + \frac{v_x^2}{2} \tag{6.34}$$

Then, the tension T(t) in the viscoelastic filament can be expressed as:

$$T(t) = EA\left(\frac{ds' - ds}{ds}\right) + \xi A\left(\frac{ds' - ds}{ds}\right)_t = EA\left(u_x + \frac{v_x^2}{2}\right) + \xi A\left(u_{xt} + v_x v_{xt}\right) \tag{6.35}$$

Integrating Eq. (6.35) by using the boundary condition $u_t(\pm L/2, t) = 0$, and the symmetry of the problem which leads to $u_t(0, t) = 0$, we can get

$$\begin{aligned} &\int_0^{L/2} T(t)\,dx = (L/2)T(t) = EA\int_0^{L/2} \frac{v_x^2}{2}\,dx + \xi A\int_0^{L/2}\left(\frac{v_x^2}{2}\right)_t dx \Rightarrow \\ &T(t) = \frac{EA}{L}\int_0^{L/2}\theta^2 dx + \frac{\xi A}{L}\int_0^{L/2}\left(\theta^2\right)_t dx \end{aligned} \tag{6.36}$$

By substituting Eq. (6.36) into Eq. (6.31), the final equation of filament dynamic catenary with boundary condition can be written as:

$$\begin{cases} \left(EI\cdot\theta_{xx} + \xi I\cdot\theta_{xxt}\right) - \theta\cdot\left(\frac{EA}{L}\int_0^{L/2}\theta^2 dx + \frac{\xi A}{L}\int_0^{L/2}\left(\theta^2\right)_t dx\right) = -wx \\ \theta(0, t) = \theta(\pm L/2, t) = 0;\ \theta(x, 0) = 0 \end{cases} \tag{6.37}$$

The first term on the left hand of Eq. (6.37) represents the resistance to viscoelastic bending effect; and the second term represents the resistance to viscoelastic stretching effect; the inhomogeneous force term on the right hand arises from the weight of the filament.

6.3.3 Analytical method for model solution

During the early stage of deflection, $\theta << 1$, the second term on the left hand of Eq. (6.37) can be neglected, and it can be simplified as:

$$EI\cdot\theta_{xx} + \xi I\cdot\theta_{xxt} = -wx \tag{6.38}$$

Integrating Eq. (6.38) with the initial condition $\theta(0,\ t) = 0$, $\theta(\pm L/2,\ t) = 0$, and $\theta(x,\ 0) = 0$, yields

$$\theta(x,t) = \left(-\frac{wx^3}{6EI} + \frac{wL^2x}{24EI}\right)\left[1 - \exp\left(-\int_0^t \frac{E}{\xi}dt\right)\right] \tag{6.39}$$

The vertical displacement v (x, t) is

$$v(x,t) = \int_{-L/2}^{x} \theta dx = -\frac{w}{24EI}\left[\left(\frac{L}{2}\right)^2 - x^2\right]^2\left[1 - \exp\left(-\int_0^t \frac{E}{\xi}dt\right)\right] \tag{6.40}$$

This solution is resemble to the elastic beam deflection expression, and describes the initial bending deflection of whole filament in very short time. As time progresses, the stretching effect starts to dominate the deflection process from the mid-span point to lateral supported ends. And the bending effect will be localized to a $\delta x(t)$ neighborhood of the lateral attachment boundaries, while elsewhere the filament is subject primarily to stretching strain without cross-section shrinkage. Thus, over most of the filament we have a balance between stretching and gravity for the stretching solution, which satisfies:

$$\begin{cases} \theta \cdot \left[\dfrac{EA}{L}\displaystyle\int_0^{L/2}\theta^2 dx + \frac{\xi A}{L}\int_0^{L/2}\left(\theta^2\right)_t dx\right] = wx \\ x \in \left[-L/2 + \delta x,\ L/2 - \delta x\right] \end{cases} \tag{6.41}$$

Squaring Eq. (6.41), and integrating it, we can get

$$\int_0^{L/2}\theta^2 dx = \frac{w^2L^5}{24A^2}\left[E\int_0^{L/2}\theta^2 dx + \xi\int_0^{L/2}\left(\theta^2\right)_t dx\right]^{-2} = \frac{L^3\theta^2}{24x^2} \tag{6.42}$$

Similarly, we can also integrate $\left(\theta^2\right)_t$ to get

$$\int_0^{L/2}\left(\theta^2\right)_t dx = \frac{L^3\left(\theta^2\right)_t}{24x^2} \tag{6.43}$$

Substituting Eq. (6.42) and (6.43) into Eq. (6.41), we can get

$$E\theta^3 + \frac{2}{3}\xi\left(\theta^3\right)_t = \frac{24wx^3}{AL^2} \tag{6.44}$$

Integrating Eq. (6.44), it yields

$$\theta\left(x, t\right) = x\left[\frac{24w}{EAL^2}\left(1-\exp\left(-\int_0^t \frac{3E}{2\xi}dt\right)\right)\right]^{1/3} \tag{6.45}$$

The vertical displacement v(x, t) is

$$v\left(x, t\right) = \int_{-L/2}^{x}\theta dx = \left(\frac{x^2}{2}-\frac{L^2}{8}\right)\left[\frac{24w}{EAL^2}\left(1-\exp\left(-\int_0^t \frac{3E}{2\xi}dt\right)\right)\right]^{1/3} \tag{6.46}$$

In lateral boundaries, the filament must be highly curved, and the stretching solution need to change rapidly to match the supported end condition, $\theta(\pm L/2, t) = 0$. By balancing the bending term in Eq. (6.38), $EI\,\theta_{xx} + \xi I\,\theta_{xxt} \sim ED^4/\delta x^2 + \xi D^4\,\theta/(\delta x^2 t)$ with the weight wx, and substituting stretching solution Eq. (6.39), yields the scaling width $\delta x(t)$ of the bending boundary layer, $\delta x \sim (E^2/3+\xi E^{-1/3}/t)^{1/2}\,(D^5/wL)^{1/3}\,[1\text{-}\exp(-\int_0^t 3E/2\xi dt)]^{1/6}$.

6.3.4 Equilibrium shape profiles of viscoelastic spanning elements

As the time $t \to \infty$, the spanning filament reached its equilibrium shape, and the equilibrium width $\delta x\,(t \to \infty)$ of the bending boundary layer can be scaled as $\delta x \sim (ED^5/wL)^{1/3}$. In the lateral bending boundary layer, the equilibrium shape was

calculated through the bending solution Eq. (6.40); while in the middle stretching layer, the equilibrium shape was calculated through the stretching solution Eq. (6.46).

$$\begin{cases} v\left(x, t \to \infty\right) = -\dfrac{w}{24EI}\left[\left(\dfrac{L}{2}\right)^2 - x^2\right]; x \in \left[-L/2, -L/2+\delta x\right] \cap \left[L/2-\delta x, L/2\right] \\ v\left(x, t \to \infty\right) = \left(\dfrac{x^2}{2} - \dfrac{L^2}{8}\right)\left(\dfrac{24w}{EAL^2}\right)^{1/3}; x \in \left[-L/2+\delta x, L/2-\delta x\right] \end{cases} \tag{6.47}$$

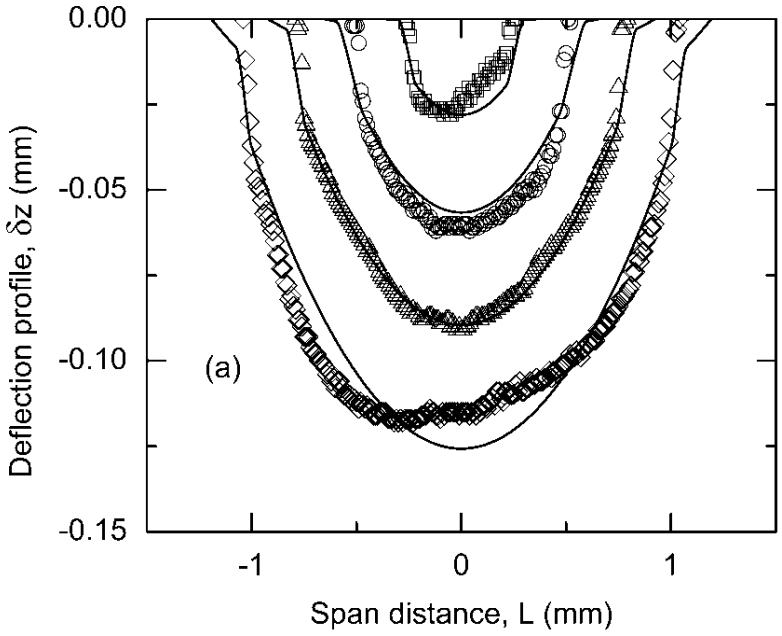

Figure 6.7 Equilibrium deflection profiles of spanning filaments deposited at a speed of 6 mm/s for span distances L = 0.775 (□), 1.312 (○), 1.849 (△), and 2.386 (◇) mm from PZT colloidal inks at varying pH = (a) 7.60, (b) 6.85, and (c) 6.15.

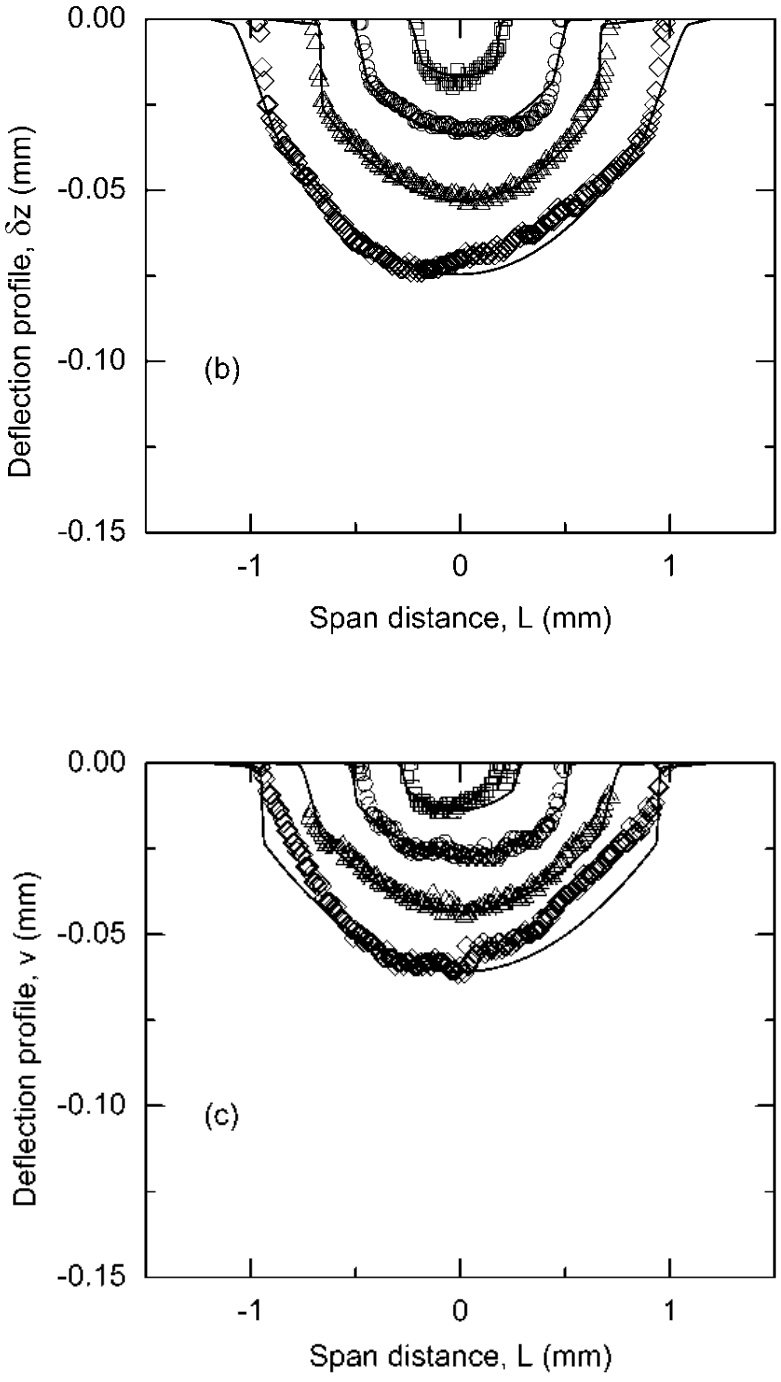

Figure 6.7 Equilibrium deflection profiles of spanning filaments deposited at a speed of 6 mm/s for span distances L = 0.775 (□), 1.312 (○), 1.849 (△), and 2.386 (◇) mm from PZT colloidal inks at varying pH = (a) 7.60, (b) 6.85, and (c) 6.15.

From Eq. (6.47), we can see that the final shape of the spanning filament is determined by its weight distribution w, diameter D, span distance L, and elastic modulus G'. For a specific colloidal ink deposited by the same tip, only span distance L, and elastic modulus G' are variables for this model equation. Previous research [40] has correlated the G' to the shear history. Here, we assume that the properly effective elastic modulus G'_{eff} needs to be selected and predetermined to fit the data.

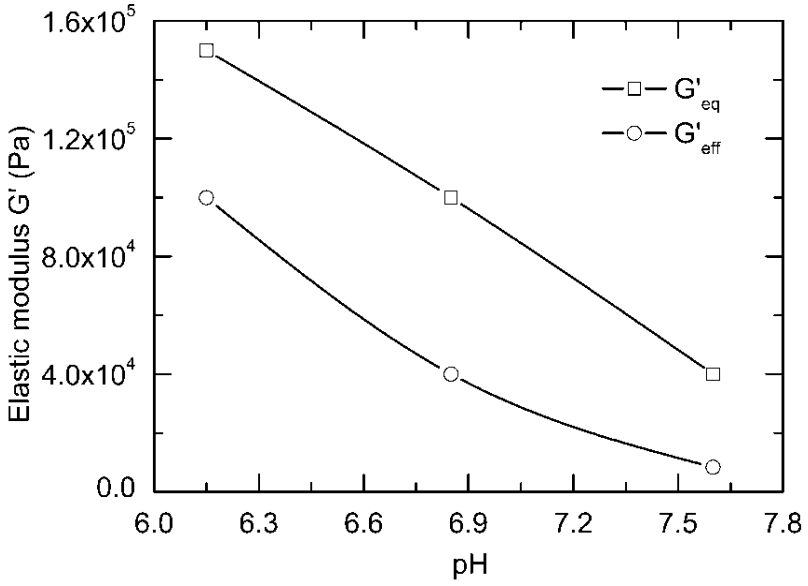

Figure 6.8 Comparison of effective elastic modulus G'_{eff} and equilibrium elastic modulus G'_{eq} of PZT colloidal inks as a function of pH at a deposition speed of 6 mm/s.

Figure 6.7 shows the equilibrium deflection profile of selected filaments at different pH values. We can see that as the pH value decreases, the corresponding deflection decreases remarkably. This phenomenon is the result of the gel strength reduction with the pH decrease. Besides, the span distance augment leads to the increase of filaments deflection profile at all pH values. Here, we use a piecewise function of Eq. (6.47) to

describe the deflection profile in the whole intervals of span distance. Although this method will lead to the unsmooth of the fitting curve and inaccurate in the lateral range, the fitting curve still can provide precise prediction in the middle range and boundary layer near two support ends.

Figure 6.8 shows the varying trend of the G'_{eff} with the pH value of PZT colloidal inks at the same deposition speed of 6 mm/s. As the pH value increases, the gel strength is attenuated, so that the corresponding G'_{eq} decreases simultaneously. Due to the shear flow during extrusion process, the G'_{eff} is always below the G'_{eq} for PZT colloidal inks with different gel strength. And the G'_{eff} also decreases with the descending of the gel strength caused by the pH reduction.

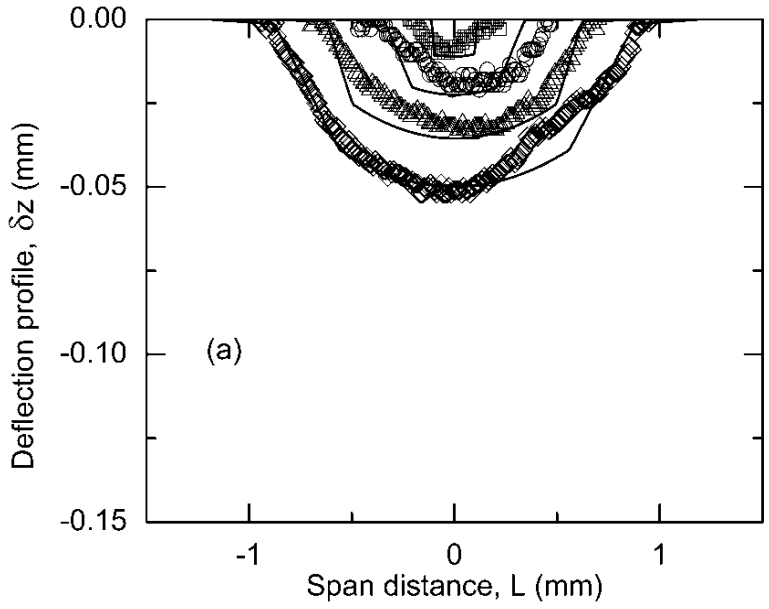

Figure 6.9 Equilibrium deflection profiles of spanning filaments deposited at speeds of (a) 2mm/s, (b) 8mm/s, for span distances L = 0.775 (□), 1.312 (○), 1.849 (△), and 2.386 (◇) mm from PZT colloidal inks at pH = 6.15.

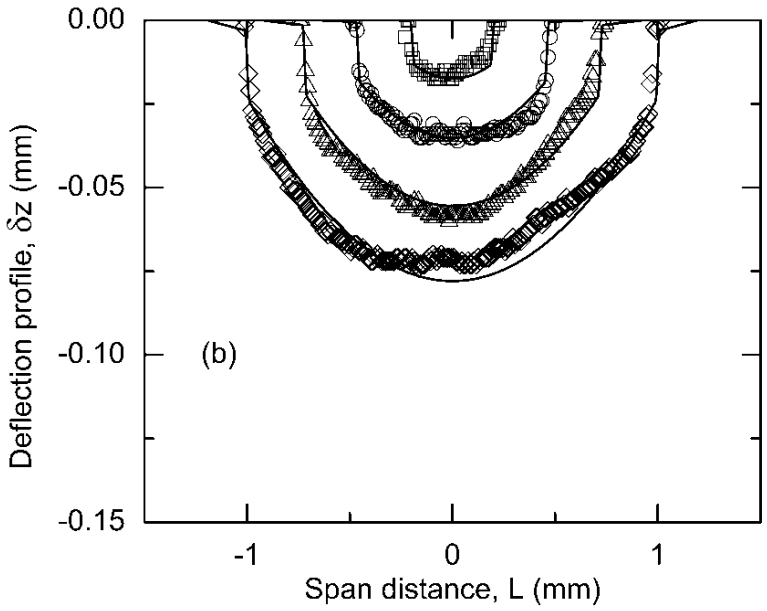

Figure 6.9 Equilibrium deflection profiles of spanning filaments deposited at speeds of (a) 2mm/s, (b) 8mm/s, for span distances L = 0.775 (□), 1.312 (○), 1.849 (△), and 2.386 (◇) mm from PZT colloidal inks at pH = 6.15.

Figure 6.9 shows the deposition speed's influence on the equilibrium deflection profiles for PZT colloidal inks at pH = 6.15. We can find that the higher deposition can generate larger deflection profile for various span distances. This can be explained by the relationship between the deposition speed and G'_{eff}. Here the pH is a constant of 6.15, the only factor can alter the G'_{eff} is the deposition. According to the selected values of G'_{eff}, we can know the G'_{eff} decreases as the deposition speed increases, as illustrated in Figure 6.10. In Figure 6.10, the G'_{eff} varying trend of PZT colloidal inks at pH = 6.15 was illustrated as a function of deposition speeds. Comparing to the G'_{eq} (dash-dot line), the G'_{eff} get close to the G'_{eq} at lower deposition speed, and as the deposition speed increases,

the G'_{eff} decreases from slow to dramatically. This trend indicates that the G'_{eff} is sensitive to the deposition speed, whose increase can greatly attenuate the G'_{eff}.

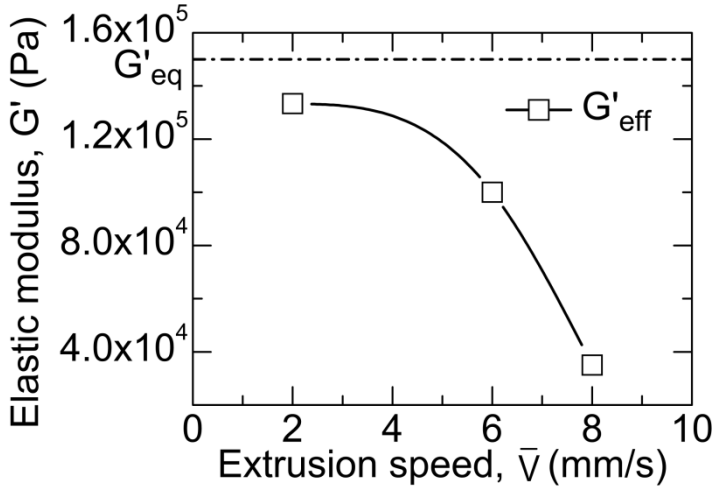

Figure 6.10 The effective elastic modulus G'_{eff} of PZT colloidal inks at pH = 6.15 vary with deposition speeds.

6.3.5 Time dependent shape evolution of viscoelastic spanning filaments

Since the initial bending is in very short time, we just use the stretching function of Eq. (6.46) to track the mid-span point dynamic deflection by setting x = 0 as:

$$v(0,t) = -\frac{1}{4}\left[\frac{3wL^4}{EA}\left(1-\exp\left(-\int_0^t \frac{3E}{2\xi}dt\right)\right)\right]^{1/3} \tag{6.48}$$

Although Eq. (6.48) is not accurate enough to describe the initial deflection, it still shows the whole deflection dynamics of mid-span point. From Eq. (6.48) we can see that except for the G'_{eff}, the ratio of Young's modulus and traction coefficient E / ξ is another important factor to control the deflection velocity.

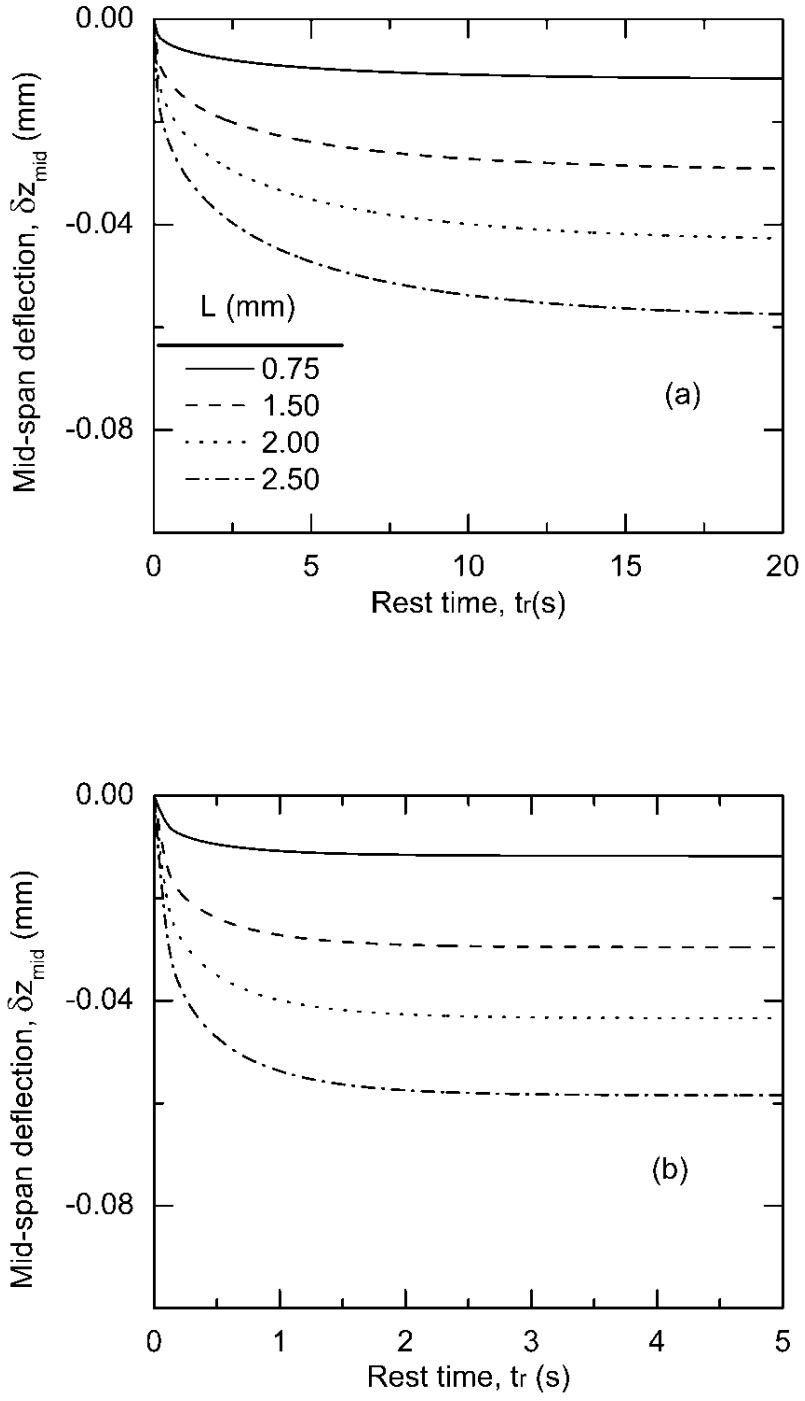

Figure 6.11 Mid-span point dynamic deflection of spanning filaments from PZT colloidal inks at pH = 6.15 by assuming $G'_{eff} = 10^5$Pa; and E / ξ = (a) 0.1, (b) 1.0, and (c) 10.

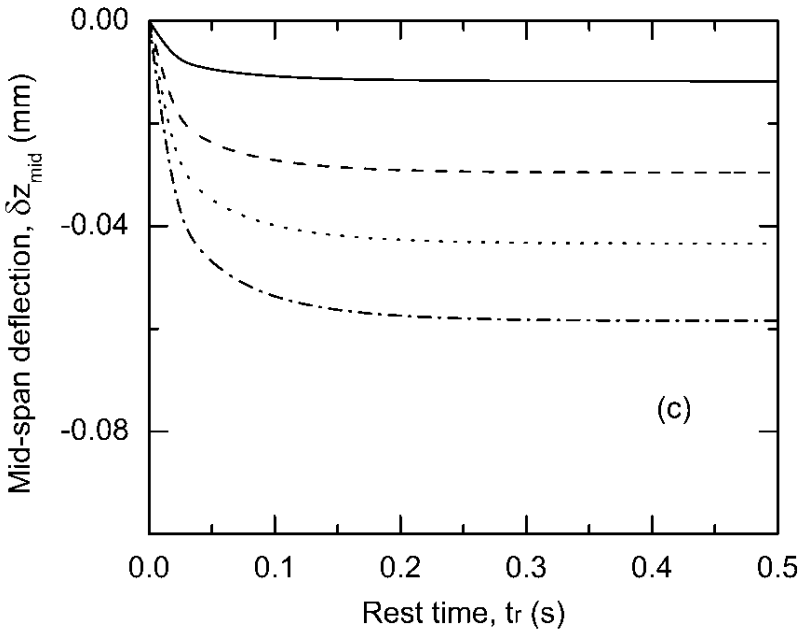

Figure 6.11 Mid-span point dynamic deflection of spanning filaments from PZT colloidal inks at pH = 6.15 by assuming $G'_{eff} = 10^5$Pa; and E / ξ = (a) 0.1, (b) 1.0, and (c) 10.

As we can see from Figure 6.11, the increase of span distance results in the increase of deflection at any instant. The deflection velocity exponentially decreases with the rest time. As the E / ξ increases, the time for mid-span point to reach its equilibrium state decreases dramatically. It can be concluded that the viscosity of the ink after deposition can significantly change the deflection velocity.

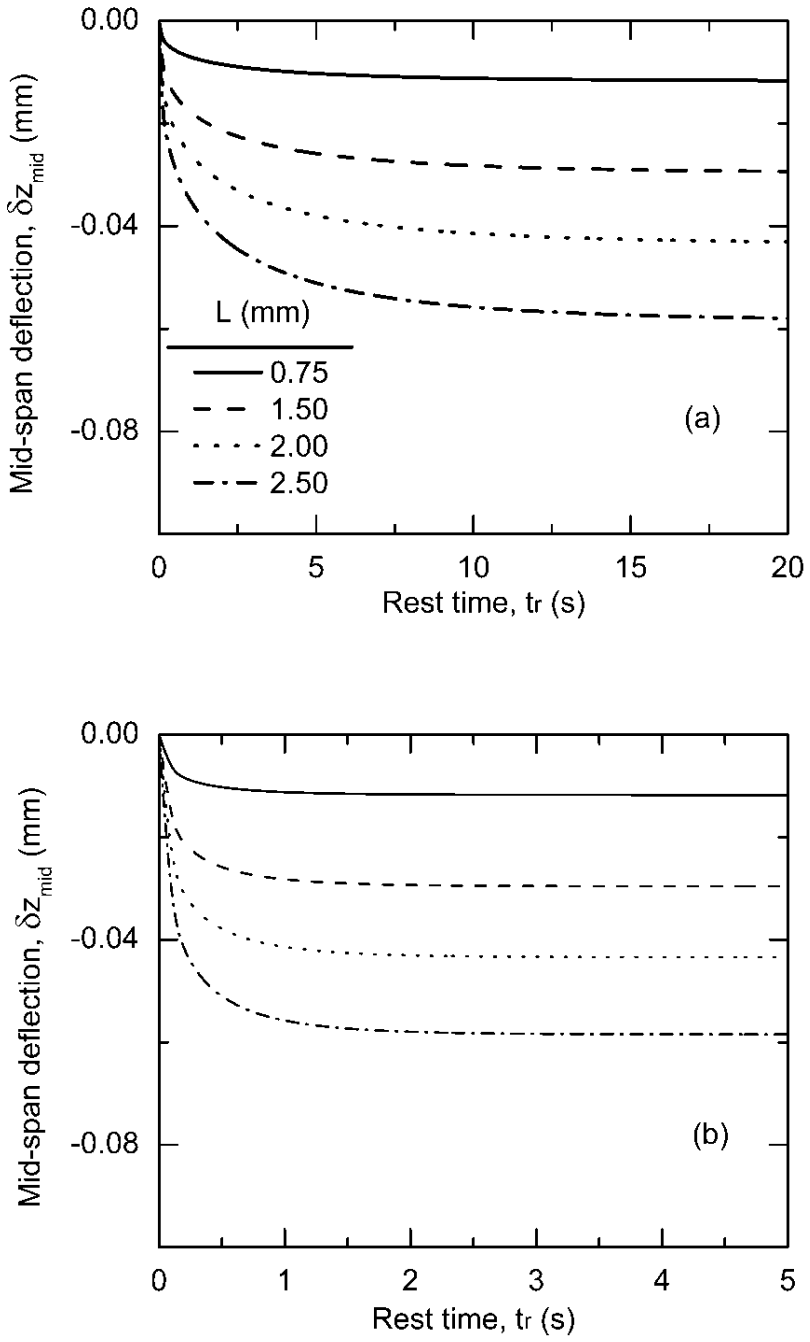

Figure 6.12 Mid-span point dynamic deflection of spanning filaments from PZT colloidal inks at pH = 6.15 by assuming $G'_{eff} = 10^5$Pa; $E / \xi_{eq} = 1.0$; $\eta_i = 0.6\ \eta_0$; and τ_e = (a) 0.1, (b) 1.0, and (c) 10s.

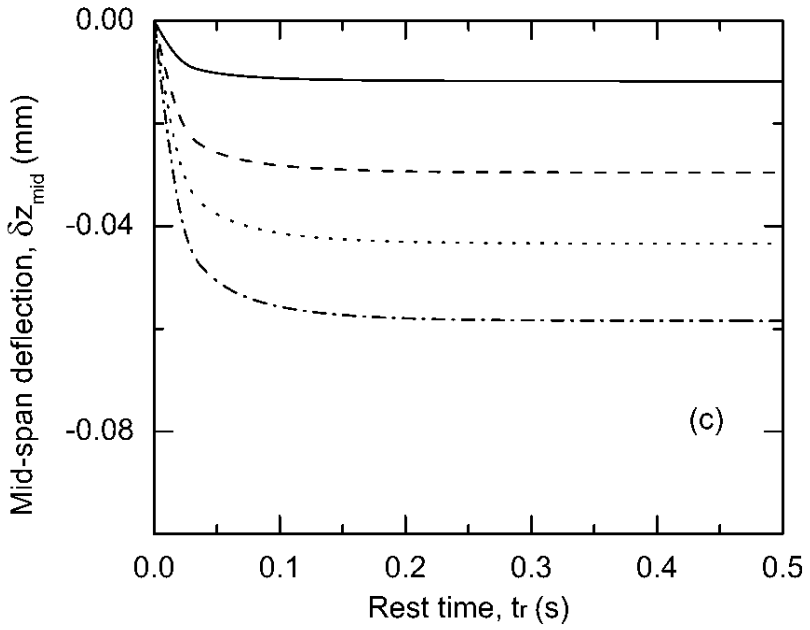

Figure 6.12 Mid-span point dynamic deflection of spanning filaments from PZT colloidal inks at pH = 6.15 by assuming $G'_{eff} = 10^5$Pa; $E / \xi_{eq} = 1.0$; $\eta_i = 0.6\ \eta_0$; and τ_e = (a) 0.1, (b) 1.0, and (c) 10s.

However, owing to the shear history during the deposition, the viscosity of the ink is not in an equilibrium state but a transition state from a lower value to equilibrium value. We assume that the instant viscosity η obeys an exponential increase as:

$$\eta = \eta_0 \left[1 - \left(1 - \eta_i / \eta_0 \right) \exp\left(-t / \tau_e \right) \right] \tag{6.49}$$

where η_i is the initial viscosity after deposition, η_o is the equilibrium viscosity, and τ_e is the relaxation time. Figure 6.12 shows the viscosity recovery's influence on the mid-span point deflection of spanning filaments with varying span distances. As the relaxation time τ increases, the mid-span point deflection velocity increases very fast.

6.4 Summary

Direct-write assembly provides flexible and inexpensive routes to rapidly design and assemble 3D mesoscale structures, whose functions are greatly determined by their physical geometry. Especially, the lattice structures with spanning filaments are widely fabricated into various 3D functional structures. In this work, a viscoelastic catenary model has been developed to describe the time dependent deflection of spanning filaments. The simulation results indicated that this model provides good predictive capability for mesoscale spanning filaments. Although the current work is limited to colloidal gels, the knowledge gained here may be easily extended to other complex ink systems such as partially melted thermoplastic polymers and metals. The contributions made by this research will open new pathways to serve as guidelines for new inks designs and 3D shape evolution control.

Further refinements in process modeling are needed to characterize the ink flow inside the deposition nozzle and the structural recovery immediately after deposition. Dynamic measurements of spanning filaments deflection are also needed to be carried out to validate the time dependent behavior of this model. These analyses will provide important information for the design of future inks and help define the processing parameters. High-performance inks combined with accurate process modeling of the direct-write assembly technique will enable the creation of microvascular networks with unparalleled complexity and commercialization of technological applications in biomedical, advanced materials and micro-fluidics.

CHAPTER 7 CONCLUSIONS AND FUTURE WORKS

The effects of colloidal inks properties, and shear history of extrusion process on the shape evolution of spanning elements were investigated via a combination of experimental measurement of interparticle interactions, rheological properties, and viscoelastic properties, and theoretical analysis of mechanism models. The fundamental knowledge emerged from this investigation should advance the new ink design on a quantitatively scientific base. In addition, this thesis also has contributed more broadly to the fundamental theory regarding the deflection phenomena of spanning elements. In this chapter, the principal findings of the study are presented, followed by proposed future research directions.

7.1 Conclusions

We have systematically investigated the effects of viscoelastic properties, structural rheology, and extrusion shear flow on the shape evolution of as-deposited 3D lattice structures. The findings yield from this project provides processing guidelines for the optimizing the ink design and operation conditions used in direct-write assembly of 3D structures at the microscale level. The important conclusions derived from this study are state below.

(1) Concentrated Al_2O_3 colloidal inks were prepared by following a two-step method. The physic-chemical properties, such as surface zeta potential, polymer adsorption were characterized. The viscoelastic properties of the ink were measured by using stress sweep method, and the solid volume fraction and flocculant concentration were considered as impact factors. Besides, the creep and recovery behavior of the ink within linear viscoelastic region were described by using a mass-less mechanical analogue.

(2) The rheological behavior of colloidal inks was investigated to understand the microstructures evolution of colloidal inks under shear flow. Experimental results revealed the viscoelastic thixotropy of the ink. A thixotropic rheology model was developed based on structural kinetics theory. A normalized structural parameter was introduced to characterize the microstructure of gels network. The model parameters were obtained by using experimental data. The simulation results showed this model can be used to describe the rheology of colloidal inks.

(3) In order to demonstrate the extrusion flow dynamics of the colloidal ink, the previous rheological model was used to carry out CFD simulation. Previous experience showed that the wall slip boundary condition was inevitable in this case. The extrusion pressure measurement was designed to characterize the wall slip. Combining with Bagley end correction, the true wall stress was computed. Then, the wall slip velocity was calculated and used to predict the velocity profiles. The structure of the colloidal ink during extrusion flow and thereafter was quantitatively described using structural parameter. The radial structural evolution after deposition was also obtained.

(4) The shape evolution of as-deposited spanning elements was investigated by both empirical model and mechanism model. Firstly, the dimensional analysis was used to

reduce the impact factors into several dimensionless groups. An empirical model was developed to relate these dimensionless groups. This empirical model was verified and used to predict the maximum deflection of mid-span point. Secondly, a viscoelastic catenary model was developed based on the static force and moment balance of suspended elements. The analytical solution was used to approximately solve the model equations. This model can be used to predict not only equilibrium shape of spanning elements, but the dynamic deflection evolution with time.

7.2 Recommendations

It is strongly encouraged that continued investigations need to be done to further prove the viability of this scheme. This study has demonstrated the far-reaching consequence of 3D structures direct-write assembly, structural shape evolution, and new ink design for colloidal processing of ceramics or metals. It is a giant step in the right direction, and especially important to potential electronics and tissue engineered scaffolds fabrication.

(1) The cross section deformation of isolated or adjacent filaments can be related to the radial structure dynamics. The relevant parameters for measurement of filament cross section will be the evolution of the aspect ratio and the eccentricity of the cross section. This is especially important for the high aspect ratio wall structures.

(2) A continuous CFD simulation of colloidal inks extrusion flow from syringe barrel to deposition onto the platform can be conducted to show the whole structures evolution during process. Especially, the free surface flow of the filament exit the nozzle is of particular importance due to its 90 degrees' bending.

(3) The visualization of the extrusion flow is another pathway to detect the inks structure during extrusion flow and can be used to verify current simulations results. Currently, visualization methods have been used in dilute suspensions flow. If there is a practical method to track the structural evolution of dense material, it can benefit a lot to current research.

(4) A high sensitive and high resolution digital camera system can be set up to directly observe the dynamic deflection of spanning elements after deposition to compare the results with model prediction. The will bring improvement to current theoretical model.

REFERENCES

1. Cesarano, J., R. Segalman, and P. Calvert, Robocasting provides moldless fabrication from slurry deposition. Ceramic Industry, 1998. 148(4): p. 94-102.

2. Tuttle, B.A., et al., Robocast Pb(Zr0.95Ti0.05)O3 Ceramic Monoliths and Composites. Journal of the American Ceramic Society, 2001. 84(4): p. 872-4.

3. Smay, J.E., et al., Directed Colloidal Assembly of 3D Periodic Structures. Advanced Materials, 2002. 14: p. 1279-83.

4. Smay, J.E., J. Cesarano, and J.A. Lewis, Colloidal Inks for Directed Assembly of 3-D Periodic Structures. Langmuir, 2002. 18: p. 5429-37.

5. Stuecker, J.N., J. Cesarano, and D.A. Hirschfeld, Control of the Viscous Behavior of Highly Concentrated Mullite Suspensions for Robocasting. Journal of Materials Processing Technology, 2003. 142: p. 318-25.

6. Smay, J.E., et al., Lead Zirconate Assembly of Linear and Annular Lead Zirconate Titanate Arrays. Journal of the American Ceramic Society, 2004. 87(2): p. 293-5.

7. Tressler, J.F., et al., Functional composites for sensor, actuators and transducers. Composites Part A (Applied Science and Manufacturing), 1999. 30A(4): p. 477-82.

8. Lee, Y.J. and P.V. Braun, Tunable Inverse Opal Hydrogel pH Sensors. Advanced Materials, 2003. 15(7-8): p. 563-566.

9. Smay, J.E., et al., Piezoelectric Properties of 3-X Periodic Pb(ZrxTi1-x)O3 Polymer Composites. Journal of Applied Physics, 2002. 92(10): p. 6119-27.

10. Blaaderen, A.v., R. Ruel, and P. Wiltzius, Template-Directed Colloidal Crystallization. Nature, 1997. 385: p. 321-4.

11. Soundararajan, R., et al., Processing of mullite-aluminum composites. Journal of the American Ceramic Society, 2001. 84(3): p. 509-13.

12. Marchi, C.S., et al., Alumina-Aluminum Interpenetrating-Phase Composites with Three-dimensional Periodic Architecture. Scripta Materialia, 2003. 49: p. 861-6.

13. Therriault, D., S.R. White, and J.A. Lewis, *Chaotic mixing in three-dimensional microvascular networks fabricated by direct-write assembly*. Nature Materials, 2003. 2(4): p. 265-71.

14. Joannopoulos, J.D., P.R. Villeneuve, and S.H. Fan, Photonic crystals: putting a new twist on light. Nature, 1997. 386: p. 143-9.

15. Michna, S., W. Wu, and J.A. Lewis, Concentrated Hydroxyappatite Inks for Direct-Write Assembly of 3-D Periodic Scaffolds. Biomaterials, 2005. 26: p. 5632-9.

16. Simon, J.L., et al., In Vivo Bone Response to 3D Periodic Hydroxyappatite Scaffolds Assembled by Direct Ink Writing. Journal of Biomedical Materials Research, 2007. 83A: p. 747-58.

17. Therriault, D., S.R. White, and J.A. Lewis, Rheological Behavior of Fugitive Organic Inks for Direct-Write Assembly. Applied Rheology, 2007. 17(1): p. 10112-1-8.

18. Lewis, J.A., Direct ink writing of 3D functional materials. Advanced Functional Materials, 2006. 16: p. 2193-04.

19. Chrisey, D.B., Materials Processing: the Powder of Direct Writing. Science, 2000. 289: p. 879-881.

20. Lewis, J.A., Colloidal Processing of Ceramics. Journal of the American Ceramic Society, 2000. 83: p. 2341-59.

21. Lewis, J.A., Direct-Write Assembly of Ceramics from Colloidal Inks. Current Opinion in Solid State and Materials Science, 2002. 6: p. 245-50.

22. Lewis, J.A., Direct Ink Writing of Three-Dimensional Ceramic Structures. Journal of the American Ceramic Society, 2006. 89(12): p. 3599-609.

23. Lewis, J.A. and G.M. Gratson, Direct writing in three dimensions. Materials Today, 2004. 7: p. 32-39.

24. Sachs, E., et al., 3-Dimensional Printing Rapid Tooling and Prototypes Directly from a CAD Model. Journal of Engineering for Industry Transactions of the ASME, 1992. 114(4): p. 481-8.

25. Sachs, E., et al., Production of Injection Molding Tooling with Conformal Cooling Channels Using the Three Dimensional Printing Process. Polymer Engineering and Science, 2000. 40(5): p. 1232-47.

26. Song, J.H., M.J. Edirisinghe, and J.R.G. Evans, Formulation and Multilayer Jet Printing of Ceramic Inks. Journal of the American Ceramic Society, 1999. 82: p. 3374-80.

27. Teng, W.D., M.J. Edirisinghe, and J.R.G. Evans, Optimization of Dispersion and Viscosity of a Ceramic Jet Printing Ink. Journal of the American Ceramic Society, 1997. 80: p. 486-94.

28. Zhao, X., J.R.G. Evans, and M.J. Edirisinghe, Direct Ink-Jet Printing of Vertical Walls. Journal of the American Ceramic Society, 2002. 85: p. 2113-5.

29. Lee, D.H. and B. Derby, Preparation of PZT Suspensions for Direct Ink Jet Printing. Journal of European Ceramic Society, 2004. 24: p. 1069-72.

30. Reis, N., C. Ainsley, and B. Derby, Viscosity and Acoustic Behavior of Ceramic Suspensions Optimized for Phase-Change Ink-Jet Printing. Journal of European Ceramic Society, 2005. 24: p. 1069-72.

31. Seerden, K.A.M., et al., Ink-Jet Printing of Wax-Based Alumina Suspensions. Journal of the American Ceramic Society, 2001. 84: p. 2514-20.

32. Cesarano, J. and P. Calvert, Freeforming Objects with Low-Binder Slurry, U.S. Patent, Editor. 2000.

33. Crump and S. Scott, Modeling apparatus for 3D objects, U.S. Patent, Editor. 1992.

34. Morissette, S.L., et al., Direct-Write Fabrication of Pb(Nb,Zr,Ti)O3 Device: Influence of Paste Rheology on Print Morphology and Component Properties. Journal of the American Ceramic Society, 2001. 84(11): p. 2462-68.

35. Bruneaux, J., D. Therriault, and M.-C. Heuzey, Micro-Extrusion of Organic Inks for Direct-Write Assembly. Journal of Micromechanics and Microengineering, 2008. 18: p. 115020 (11pp).

36. Smay, J.E., S.S. Nadkarni, and J. Xu, Direct Writing of Dielectric Ceramics and Base Metal Electrodes. International Journal of Applied Ceramic Technology, 2007. 4(1): p. 47-52.

37. Li, Q. and J.A. Lewis, Nanoparticle Inks for Directed Assembly of Three-Dimensional Periodic Structures. Advanced Materials, 2003. 15(19): p. 1639-43.

38. Rao, R.B., et al., Microfabricated Deposition Nozzles for Direct-Write Assembly of Three-Dimensional Periodic Structures. Advanced Materials, 2005. 17: p. 289-93.

39. He, G., D.A. Hirschfeld, and J. Cesarano, Processing and Mechanical Properties of Si3N4 Formed by Robocasting Aqueous Slurries, in 24th International Conference & Exposition on Engineering Ceramics and Structures. 2000: Cocoa Beach, FL.

40. Nadkarni, S.S. and J.E. Smay, Concentrated Barium Titanate Colloidal Prepared by Bridging Flocculation for Use in Solid Freeform Fabrication. Journal of the American Ceramic Society, 2006. 89(1): p. 96-103.

41. Cesarano, J. and I.A. Aksay, Processing of Highly Concentrated Aqueous α-Alumina Suspensions Stabilized with Polyelectrolytes. Journal of the American Ceramic Society, 1988. 71(12): p. 1062-7.

42. Cesarano, J., I.A. Aksay, and A. Blier, Stability of Aqueous α-Alumina Suspensions with Poly (methacrylic acid) Polyelectrolyte. Journal of the American Ceramic Society, 1988. 71(4): p. 250-5.

43. Hunter, R.J., Foundations of Colloid Science. Vol. 1. 1992, New York: Oxford University Press Inc.

44. Buscall, R., et al., The Rheology of Strongly-Flocculated Suspensions. Journal of Non-Newtonian Fluid Mechanics, 1987. 24: p. 183-202.

45. Buscall, R., I.J. McGowan, and A.J. Morton-Jones, The Rheology of Concentrated Dispersions of Weakly attracting Colloidal Particles With and Without Wall Slip. Journal of Rheology, 1993. 37(4): p. 621-41.

46. Buscall, R., et al., Scaling Behavior of the Rheology of Aggregated Networks formed from Colloidal Particles. Journal of the Chemical Society Faraday Transactions I, 1988. 84(12): p. 4249-60.

47. Krieger, I.M., Rheology of Monodisperse Lattices. 1972, Netherlands: Elsevier Publishing Co. 111-36.

48. Russel, W.B., Review of the Role of Colloidal Forces in the Rheology of Suspensions. Journal of Rheology, 1980. 24(3): p. 287-317.

49. Tohver, V., et al., Nanoparticle halos: a new colloidal stabilization mechanism. Proceedings of National Academy of Science, 2001. 98: p. 8950-54.

50. Derjaguin, B. and L. Landau, Theory of the Stability of Strongly Charged Lyophobic Sols and of the Adhesion of Strongly Charged Particles in Solutions of Electrolytes. Acta Physico Chemica URSS, 1941. 14: p. 30-59.

51. EJW, V. and O. JThG, Theory of the Stability of Lyophobic Colloids. 1948, Amsterdam: Elsevier.

52. Larson, R.G., The Structure and Rheology of Complex Fluids. 1999, New York: Oxford University Press.

53. Herschel, W.H. and R. Bulkley, Konsistenzmessungen von Gummi-Benzollosungen. Kolloid Z, 1926. 39: p. 291.

54. Smay, J.E., Direct Colloidal Assembly and Characterization of PZT-Polymer Composite, in Material Science and Engineering. 2002, UIUC: Urbana.

55. Kalyon, D.M., B.A. P. Yaras, and U. Yilmazer, Rheological Behavior of a Concentrated Suspension: A Solid Rocket Fuel Stimulant. Journal of Rheology, 1993. 37: p. 35-53.

56. Rueb, C.J. and C.F. Zukoski, Viscoelastic Properties of Colloidal gels. Journal of Rheology, 1997. 41(2): p. 197-218.

57. Firth, B.A. and R.J. Hunter, Flow Properties of Coagulated Colloidal Suspensions III. The Elastic Floc Model. Journal of Colloid and Interface Science, 1976. 57(2): p. 266-75.

58. Channell, G. and C. Zukoski, Shear and Compressive Rheology of Aggregated Alumina Suspensions. AICHE Journal, 1997. 43(7): p. 1700-8.

59. Rao, R.B., Biphasic Nanoparticle Inks for Direct Write Assembly of 3-D Periodic Structures. 2008, UIUC.

60. Rao, R.B., et al., Nonlinear Elasticity and Yielding of Nanoparticle Glasses. Langmuir, 2006. 22: p. 2241-43.

61. Chen, M. and W.B. Russel, Characteristics of Flocculated Silica Dispersions. Journal of Colloid and Interface Science, 1991. 141(2): p. 564-77.

62. Grant, M.C. and W.B. Russel, Volume-Fraction Dependence of Elastic Moduli and Transition Temperatures for Colloidal Silica Gels. Physics Review E, 1993. 47(4): p. 2606-14.

63. Shigley, J.E. and C.R. Misckhe, Mechanical Engineering Design. 5th ed. 1989.

64. Napper, D.H., Polymeric Stabilization of Colloidal Dispersions. 1983, New York: Academic Press.

65. Chen, Z.C., T.A. Ring, and J. Lemaitre, Stabilization and Processing at Aqueous BaTiO3 Suspension with Polyacrylic Acid. Journal of the American Ceramic Society, 1992. 75(12): p. 3201-08.

66. Cheremisinoff, N.P., An Introduction to Polymer Rheology and Processing. 1992, Boca Raton, FL: CRC Press.

67. Dealy, J.M. and K.F. Wissburn, Melt Rheology and Its Roles in Plastics Processing. 1990, London, New York: Chapman and Hall.

68. Osanaiye, G.J., On the Rheological Properties of Suspensions, Filled Thermoplastics and Rubber Compounds. 1994, The University of Akron.

69. Burgers, Mechanical Considerations-Model System-Phenomenological Theories of Relaxation and Viscosity. In First Report on Viscosity and Plasticity. 1935, New York: Nordemann, Publishing Company.

70. Roberts, M.T., et al., Direct Flow Visualization of Colloidal Gels in Microfluidic Channels. Langmuir, 2007. 23: p. 8726-31.

71. Conrad, J.C. and J.A. Lewis, Structure of Colloidal Gels during Microchannel Flow. Langmuir, 2008. 24(15): p. 7628-34.

72. Barnes, H.A., Thixotropy-a review. Journal of Non-Newtonian Fluid Mechanics, 1997. 70: p. 1-33.

73. Mewis, J., Thixotropy-general review. Journal of Non-Newtonian Fluid Mechanics, 1979. 6(1): p. 1-20.

74. Mewis, J. and N.J. Wagner, Thixotropy. Advances in Colloid and Interface Science, 2009. 147-148: p. 214-227.

75. Mujumdar, A., A.N. Beris, and A.B. Metzner, Transient phenomena in thixotropic systems. Journal of Non-Newtonian Fluid Mechanics, 2002. 102: p. 157-178.

76. Moore, F., The Rheology of Ceramic Slips and Bodies. Transactions and Journal of the British Ceramic Society, 1959. 58: p. 470-94.

77. Cheng, D.C.H. and F. Evans, Phenomenological characterization of the rheological behavior of inelastic reversible thixotropic and antithixotropic fluids. British Journal of Applied Physics, 1965. 16: p. 1599-1617.

78. Acierno, D., et al., Nonlinear viscoelastic model with structure-dependent relaxation times. 2. Comparison with LD Polyethylene transient stress results. Journal of Non-Newtonian Fluid Mechanics, 1976. 1: p. 147-157.

79. Yziquel, F., et al., Rheological modeling of concentrated colloidal suspensions. Journal of Non-Newtonian Fluid Mechanics, 1999. 86: p. 133-155.

80. Doraiswamy, D., et al., The Cox-Merz rule extended: a rheological model for concentrated suspensions. Journal of Rheology, 1991. 34: p. 647-685.

81. Dullaert, K. and J. Mewis, A Structural Kinetics Model for Thixotropy. Journal of Non-Newtonian Fluid Mechanics, 2006. 139: p. 21-30.

82. Dullaert, K. and J. Mewis, Stress Jumps on Weakly Flocculated Dispersions: Steady State and Transient Results. Journal of Colloid and Interface Science, 2005. 287: p. 542-551.

83. Dullaert, K. and J. Mewis, Thixotropy: Build-up and Breakdown Curves during Flow. Journal of Rheology, 2005. 49(6): p. 1213-1230.

84. Labanda, J. and J. Llorens, A Structural Model for Thixotropy of Colloidal Dispersions. Rheology Acta, 2006. 45: p. 305-14.

85. Şakar-Deliormanlı, A., E. Çelik, and M. Polat., Rheological behavior of PMN gels for solid freeform fabrication. Colloids and Surfaces A: Physicochemical and Engineering Aspects., 2008. 324(1-3): p. 159-66.

86. Toorman, E.A., Modeling the thixotropic behavior of dense cohesive sediment suspensions. Rheology Acta, 1997. 36: p. 56-65.

87. Chen, J.Y. and Z. Fan, Modelling of Rheological Behavior of Semisolid Metal Slurries Part 2-Steady State Behavior. Material Science and Technology, 2002. 18: p. 243-249.

88. Gautham, B.P. and P.C. Kapur, Rheological Model for Short Duration Response of Semi-Solid Metals. Material Science and Engineering A, 2005. 393: p. 223-228.

89. Kee, D.D. and G. Turcotte, Viscosity of biomaterials. Chemical Engineering Communication, 1980. 6: p. 273-282.

90. Joye, D.D. and G.W. Poehlein, Characteristics of Thixotropic Behavior. Transaction of the Society of Rheology, 1971. 15: p. 51-61.

91. Nakagawa, T. and M. Kobe, Rheology. 1965, Tokyo: The publishing House of Misuzu.

92. Morissette, S.L., et al., Solid freeform fabrication of aqueous alumina-poly(vinyl alcohol) gelcasting suspensions. Journal of the American Ceramic Society, 2000. 83(10): p. 2409-16.

93. Barn, H.A., A Review of Slip (Wall Depletion) of Polymer Solutions, Emulsions, and Particle Suspensions in Viscometers: Its Cause, Character, and Cure. Journal of Non-Newtonian Fluid Mechanics, 1995. 56: p. 221-251.

94. Bagley, E.B., End Correction in the Capillary Flow of Polyethylene. Journal of Applied Physics, 1957. 28: p. 624-7.

95. Jastrzebski, Z.D., Entrance Effects and Wall Effects in an Extrusion Rheometer during the Flow of Concentrated suspensions. Industrial and Engineering Chemistry Fundamentals, 1967. 6(3): p. 445-453.

96. Xie, B., et al., Synthesis Direct Writing of Three Dimensional Polymer Scaffolds Using Colloidal Gels. Advanced Functional Materials, 2006. 16(13): p. 1685-93.

97. Therriault, D., et al., Fugitive Inks for Direct-Write Assembly of Three-Dimensional Microvascular Network. Advanced Materials, 2005. 17(4): p. 395-9.

98. Munson, B.R., D.F. Young, and T.H. Okiishi, Fundamentals of Fluid Mechanics. 2002, New York: John Wiley & Sons, Inc.

99. Szirtes, T., Applied Dimensional Analysis and Modeling. 1998, New York: McGraw-Hill.

100. Lenczner, D., Deflection of Beams and Composite Walls Subject to Creep Building Science, 1971. 6: p. 45-51.

101. Teichman, J. and L. Mahadevan, The Viscous Catenary. Journal of Fluid Mechanics, 2003. 478: p. 71-80.

102. Love, A.E.H., A Treatise on the Mathematical Theory of Elasticity. 1944: Dover.

103. Irvine, H.M., Cable Structures. 1981, New York: Dover Publication, Inc.

VITA

Cheng Zhu

Candidate for the Degree of

Doctor of Philosophy

Thesis: SHAPE EVOLUTION OF 3D PERIODIC STRUCTURE FABRICATED BY DIRECT-WRITE ASSEMBLY OF CONCENTRATED COLLOIDAL GELS

Major Field: Chemical Engineering

Biographical:

Personal Data: Cheng Zhu was born on November 21, 1980, in Wuxi, China to Keang Zhu and Shuangfeng Chen.

Education: He received the Bachelor of Science in Bioengineering at Wuxi University of Light Industry, Wuxi, China in 2003. He earned the Master of Science in Chemical Engineering at East China University of Science and Technology, Shanghai, China in 2006. He completed the requirements for the Doctor of Philosophy in Chemical Engineering at Oklahoma State University, Stillwater, Oklahoma in December, 2010.

Experience: Employed at Oklahoma State University, School of Chemical Engineering as Research Assistant, 2006-2010
Employed at East China University of Science and Technology, School of Chemical Engineering as Research Assistant, 2003-2006

Professional Memberships: The American Ceramic Society
Materials Research Society
AICHE

Name: Cheng Zhu Date of Degree: December, 2010

Institution: Oklahoma State University Location: Stillwater, Oklahoma

Title of Study: SHAPE EVOLUTION OF 3D PERIODIC STRUCTURE FABRICATED BY DIRECT-WRITE ASSEMBLY OF CONCENTRATED COLLOIDAL GELS

Pages in Study: 126 Candidate for the Degree of Doctor of Philosophy
Major Field: Chemical Engineering

Scope and Method of Study: 3D periodic structures were fabricated by direct-write assembly of concentrated colloidal gels with self-supporting features. The rheological behavior of the gel was characterized in linear viscoelastic regions. The flow behavior of the gel was modeled by using structural kinetics theory. Based on this model, the dynamic extrusion process of the gel was simulated by incorporating slip wall boundary conditions. A viscoelastic catenary model was developed to describe span shape and compare the results to previous results that used a simple elastic beam theory. The shape evolution (i.e., spanning behavior) of spanning filaments observed was related to shear stress conditions and a limited set of rheological parameters.

Findings and Conclusions: The rate and magnitude of microstructure change within a colloidal gel ink are crucial factors for shape evolution of 3D structures assembled by direct write techniques. The events that set the equilibrium shape of 3D structure occur within the initial few seconds after deposition and gels microstructure recovery within this period is critical to geometric fidelity. The shape evolution of 3D structures may be predicted by knowledge of the rheological behavior of the colloidal gel in shear loading. Rheological behavior can be related to the structural recovery time of the colloidal gel and this may be measured with a series of equilibrium flow measurements. Successful completion of this research advances science-based ink design methods and optimization of deposition variables. Better control of shape evolution will lead to improvements in advanced applications such as photonic band gap structures, artificial bone structures, and metal-ceramic composites. The improved connections between time-dependent shear behavior and shape evolution in an extrusion process will also impact other industries (e.g., clay extrusion for catalytic converter substrates) and improve industrial productivity through better paste design. Although the current work is limited to colloidal gels, the knowledge gained here may be easily extended to other complex ink systems such as partially melted thermoplastic polymers and metals.

ADVISER'S APPROVAL: Dr. James E. Smay